UNIVERSIDAD AUTÓNOMA DE MADRID
FACULTAD DE CIENCIAS
DEPARTAMENTO DE FÍSICA DE MATERIALES

HARRISSON DAVID ASSIS SANTOS

Ag_2S nanodots for advanced biological applications through Luminescence Thermometry and Fluorescence Images

.

"Ever tried. Ever failed. No matter.
Try Again. Fail again. Fail better".

Samuel Beckett

Madrid
2019

UNIVERSIDAD AUTÓNOMA DE MADRID
FACULTAD DE CIENCIAS
DEPARTAMENTO DE FÍSICA DE MATERIALES

HARRISSON DAVID ASSIS SANTOS

Ag_2S nanodots for advanced biological applications through Luminescence Thermometry and Fluorescence Images

Thesis reported as a partial requirement to obtain a PhD title in Physics.

Phd Thesis Advisors:
Prof. Dr. Carlos Jacinto da Silva (UFAL-Brazil)
Prof. Dr. Daniel Jaque García (UAM – Spain)

Madrid
2019

UNIVERSIDADE FEDERAL DE ALAGOAS

INSTITUTO DE FÍSICA

PROGRAMA DE PÓS- GRADUAÇÃO EM FÍSICA

HARRISSON DAVID ASSIS SANTOS

Ag_2S nanodots for advanced biological applications through Luminescence Thermometry and Fluorescence Images

.

“Ever tried. Ever failed. No matter.

Try Again. Fail again. Fail better”.

Samuel Beckett

Maceió-AL

2019

UNIVERSIDAD AUTÓNOMA DE MADRID
FACULTAD DE CIENCIAS
DEPARTAMENTO DE FÍSICA DE MATERIALES

HARRISSON DAVID ASSIS SANTOS

Ag_2S nanodots for advanced biological applications through Luminescence Thermometry and Fluorescence Images

Thesis reported as a partial requirement to obtain a PhD title in Physics.

Phd Thesis Advisors:
Prof. Dr. Carlos Jacinto da Silva (UFAL-Brazil)
Prof. Dr. Daniel Jaque García (UAM – Spain)

Maceió-AL
2019

Abstract

Remarkable investigations/discoveries were performed/found out throughout the development of this thesis motivated by the needs of updated technologies that support basic human well-being and survival. Hybrid nanostructures based on the semiconductor of silver sulfide nanodots (Hereafter, Ag_2S nanodots) have been employed for carrying out different challenging tasks because of their unique and superb performance as a florescent agent of multifunctional character, acting as nanoheaters, thermal sensors, biolabelings and biomarkers. Based on these well-known outstanding features of nanostructures of Ag_2S nanodots, one major challenge in this thesis was to focus on their synthesis production, aiming to improve structural and fluorescence properties, their biocompatibilities and to achieve suitable surface decoration to specific purposes. Furthermore, their fluorescence emission lies in the so-called second biological window (II-BW), conducting to higher penetration depths of emitted photons and reducing autofluorescence due to the barely scattering and absorption of these energy photons in living tissues. Another remarkable advantage is that this material is well-excited under 800 nm of excitation photons, which is also weakly absorbed by living tissues. All these terrific features working in partnership with its multifunctional character open up the possibility of realizing so dreamed applications concerning preclinical assay. Among them, we could deal with some as can be briefly mentioned: Ex-vivo experiments were projected to provide detailed information about thermal gradients in subcutaneous studies based on the temperature dependency of the time-resolved fluorescence dynamics of our synthesized (or purchased) Ag_2S, in other words, exploiting its thermal sensing talent. Concerning its thermal sensing ability based on the luminescence properties, it also enabled us to perform an efficient detection of a tumor and even providing a well accurate prediction of its stage. During the progress of this thesis we also produced a new version of Ag_2S nanodots by far the brightest contrast agent reported in literature so far. We named them as Ag_2S superdots and some preclinical assay were carried out, enabling us to monitor, for example, its *in* vivo bio-distribution after low-dose intravenous administration and using the lowest power density dose so far reported.

Resumen

A lo largo del desarrollo de esta tesis se realizaron investigaciones notables motivadas por las necesidades de tecnologías actualizadas que respalden el bienestar y la supervivencia humanos básicos. Nanoestructuras híbridas basadas en el semiconductor de nanodots de sulfuro de plata (en adelante, nanodots Ag_2S) se han empleado para llevar a cabo diferentes tareas desafiantes debido a su rendimiento único y excelente como agente fluorescente de carácter multifuncional, actuando como nanocalentadores, sensores térmicos, bioetiquetas y biomarcadores. Sobre la base de estas características sobresalientes bien conocidas de las nanoestructuras de nanodots Ag_2S, un desafío muy importante sucedió sobre el procedimiento de síntesis, con el objetivo de mejorar las propiedades estructurales y de fluorescencia, sus biocompatibilidades y lograr una decoración de superficie adecuada para fines específicos. Además, su emisión de fluorescencia reside en la bien conocida y llamada segunda ventana biológica (II-BW), que conduce a profundidades de penetración más profundas de los fotones emitidos y reduce la autofluorescencia debido a la escasa dispersión y absorción de estos fotones de energía en los tejidos vivos. Otra ventaja notable es que este material está bien excitado bajo a excitación de 800 nm, que también es débilmente absorbido por los tejidos vivos. Todas estas características estupendas que trabajan en asociación con su carácter multifuncional permiten la posibilidad de realizar aplicaciones tan soñadas con respecto al ensayo preclínico. Entre ellos, se ha podido tratar algunos como se puede mencionar brevemente: se ha proyectado experimentos en ex-vivo que proporcionaron información detallada sobre gradientes térmicos en estudios subcutáneos basados en la dependencia con la temperatura de la dinámica de fluorescencia resuelta en el tiempo de nuestros Ag_2S sintetizado (o comprado), en otras palabras, explotamos su talento para detección térmica. En relación a su capacidad de detección térmica basada en las propiedades de luminiscencia, esta nos permitió realizar una detección eficiente de un tumor e incluso proporcionar una predicción precisa de su grado. A lo largo del desarrollo de esta tesis, también produjimos una nueva versión de nanodots Ag_2S, con mucho, el agente de contraste más brillante reportado en la literatura hasta ahora. Los nombramos como superpuntos Ag_2S y se llevaron a cabo algunos ensayos preclínicos, lo que nos permitió controlar, por

ejemplo, su biodistribución in vivo después de la administración intravenosa de dosis bajas y utilizando la dosis de densidad de potencia más baja informada hasta ahora.

Resumo

Investigações/descobertas notáveis foram realizadas/encontradas durante todo o desenvolvimento desta tese motivadas pela necessidade de tecnologias atualizadas que estimulam o bem-estar humano básico e sua sobrevivência. Nanoestruturas híbridas baseadas em "nanopontos" de semicondutor de sulfato de prata (daqui por diante chamaremos de Ag_2S nanodots) têm sido empregadas para realizar diversas tarefas desafiadoras, isso porque apresentam por conta de seus desempenhos excelentes e únicos como agentes fluorescentes de caráter multifuncional, atuando como nanoaquecedores, sensores térmicos, rotuladores biológicos em nível celular e indicadores de estado médico. Com base nestas tão bem conhecidas características excepcionais das nanoestruturas de Ag_2S nanodots, um dos grandes desafios focado nesta tese foi sobre possíveis métodos de síntese de Ag_2S, visando melhorar as propriedades estruturais e de fluorescência, suas biocompatibilidades e funcionalização de superfície visando propostas específicas. Além disso, as emissões de fluorescência encontram-se na chamada segunda janela biológica (II-BW), conduzindo a profundidades de penetrações mais profundas de fótons emitidos e reduzindo assim sinais de autofluorescência por tecidos, já que esses fótons de energia são fracamente espalhados ou absorvidos por tecidos vivos. Outra vantagem notável é que este material é bem excitado por fótons com comprimento de onda em torno de 800 nm, que é também fracamente absorvido por tecidos vivos. Todas essas características excelentes junto com seu caráter de múltiplas aplicações abrem a possibilidade de uma das mais desejadas aplicações no que diz respeito a ensaios pré-clínicos. Entre algumas, nós conseguimos conduzir com as que serão brevemente mencionadas a seguir: Experimentos em ex-vivo foram projetados para fornecer informações detalhadas sobre gradientes térmicos em estudos subcutâneos baseados na dependência com a temperatura da dinâmica de fluorescência resolvida no tempo de nossos Ag_2S produzidos (ou comprados), ou seja, explorando sua habilidade como sensor térmico. Ainda com respeito a sua habilidade de sensoriamento térmico baseados em propriedades luminescentes, nos capacitou realizar detecção de um tumor de melanoma e, além disso, predizer seu estágio com excelente precisão. Durante o desenvolvimento

desta tese nós também produzimos uma nova versão de Ag_2S nanodots, sendo de longe o agente de contraste fluorescente mais brilhante reportado até o momento na literatura. Nós o nomeamos de Ag_2S superdots e alguns ensaios pré-clínicos foram realizados, nos capacitando monitorar, por exemplo, sua bio-distribuição em *in* vivo após administrar uma dose pequena por via intravenosa e usando a mais baixa densidade de potência até o momento relatada.

Acknowledgements

I could start with a usual phrase from an acknowledgment template “I would first like…” maybe I should. But probably the sequence would not be from my own words, so, I shall do something more personal, in my style. Even though be simple words, it comes from my heart and my sincere gratitude. First, I would like to say that if there is a superhero, it is my mother. She took care of her two kids (the truth is that is still doing it.) and I should confess that I was not an easy kid in my childhood. She was/is our best mother, best father, friend, biggest teacher (especially concerning life lessons), doctor (always when we got hurt, she was there to be our doctor/nurse), and our security guard (she was capable of wearing fight gloves and challenge one who given signs of aspiring to threat her children. So instead of saying "I would like to thank you Mom" I prefer say that I LOVE YOU SO MUCH. You have provided me love, protection, emotional support and everything that I needed during this challenging time in my life (indeed, during entire life).

I do not believe in an interventionist God, in which gives gifts and a better life to one whom one calls to be "special". Instead of it, I believe that special people cross our life and all of us have the opportunity to not allow them to go. I could mention a lot of people here, but it is impossible to mention everyone giving them to the appropriated feeling descriptions. So, I selected the person that I believe is my partner in life. Although we haven't gotten married (at least not during this acknowledgements writing) and you are not my wife yet (at least in law), I can guarantee that you, Thayna, are the woman that I desired to have on my side, to make plans and dream of about future, and you know we have done a lot during these six years together (Yes, I know, it is already time to get married...) and we are still working to achieve them. I think I do not need to mention here that you are always giving me emotional support and so on… I might only say, I LOVE YOU SO MUCH.

Many thanks to my family, especially for those more close, providing me love and support, my niece-sister Carol and my Grandmother Beatriz, they were always keen to know what I was doing and why I was always locked up at home or at university. Likely they never grasped very well what I was doing, but always said me great words and screams of joy when I passed through great moments.

One of these great moments was my travel to Spain, especially to be able to enjoy one of the most beautiful cities of the world; one can easily guess I am talking about the beautiful Madrid. I spent one and half (1.5) glorious years there; I had the great opportunity to open more my mind and grew a lot in both standpoints personal and professional. It was an experience that I will never forget. There I have met amazing people, new friends, including inside or outside of work. A very special gratitude goes out to the FIG`s family, although I was not able to express very well my happiness, it was amazing to share moments with them, from the simple ones such chatting about sport (mainly football and basketball) and funny moments; sharing ideas, places; have lunch and to the more "serious" like trips, discussion about science, playing with lasers and taking care of cute mice and so on. Among the researchers that I met there I would like to say thank you so much for every one of you; Lucía, Hu jie, Emma, Blanca, Dirk, Patri, Yingli, Dasheng, Tamara, Jinke, Paloma, Antonio, Elisa, Gabriel and Michelle. A special thanks to Lucía, Patri and Emma that were always rescue me when I was in trouble in lab stuffs.

I could not forget to mention the especial times that I have with some of them out university. Hu Jie was a great friend, although sometimes we had some little "disagreements". We played uncountable football and basket matches, we watched some matches of the world cup, and he even supported Brazil on the quarterfinals (although we lost). Indeed Hu jie was not the only Chinese friend I made there, I would like to offer a special hug to Yingli, that was an incredible friend and we have done an amazing partnership there, sharing experiments, work and so on. I would like to say that Dasheng and Jinke were great friends outside of university; we have shared a lot of special moments. A great hug to the UAM football group, especially to Davi, Alejandro and Naomi that I have shared the office and we have funny moments and talks together.

A very special gratitude goes out to the members of the Medicine School of UAM; to Prof. Dr. Luis Monge, the student Ana and especially to Prof. Dr. María (Mamen) del Carmen Iglesias de la Cruz, Prof. Dr. Nuria Fernández and our kids (the mice). The moments there were amazing, Mamen and Nuria are two great women that I will never forget. We have shared more than experiments; we have shared really funny moments and amazing talks.

My deepest appreciation goes out to Prof. Dr. José García Solé (Pepe) who was always saying wonderful words of motivation “Eres un crack, ha hecho muy bien…” He was a great Professor, whom I consider a co-supervisor, always giving great ideas and advices for improvements.

A very special thanks goes out to the faculty members of the UCM; to Diego and Prof. Dr. Marco Laurenti and especially to Prof. Dr. Jorge Rubio R. (The great Jorge), who taught me a lot of things concerning chemical subjects during our scientific discussions but also propagated European culture by telling remarkable moments of Spain history. He was a great friend and a co-supervisor during my studies in Spain.

Leaving Europe and going to South America … Indeed everything began in my motherland, in my Big and Great Brazil. I have made great friends during my studies here; indeed we have a group called “Brothers of the LNFIM”. A special hug to them; Wesley (O Coite), Jefferson (Jeffrey), Michael (Jackson), Tasso (O Magrelo). I think it is not possible to mention the especial moments that we have had. All of you will be forever in my heart. I would like to say thank you to the young researchers that were newly promoted to professors and shared experiences with me; to Ueslen and Wesley. I special hug to my friend Erving, which has been a great example of student/researcher and I could got from him great tips to improve my professional skills. Not forgetting our conversations and laughs since we were undergraduate. I would like to say thank you to all GNFI group, for sharing great experiences and knowledgements. Not forgetting to mention the great women of our Group, which I have learned a lot during this last year, a huge hug to Laís, Camila and Carol.

I would like to offer my special thanks to Prof. Wagner Ferreira. On this final stage, he was always supporting me, giving remarkable advices to life and work, helping me to enhance my professional abilities. Indeed, I can say he is an offstage tutor and of course a great friend.

The research for this thesis was financially supported by Brazilian agencies CAPES and CNPq, in which I am deeply grateful. Also I would like to express my gratitude to all Brazilian people that contribute directly to scientific researches through their taxes contributions. I am also grateful to COST for providing me financial support to participate in some remarkable events during my studies in Spain.

I would like to express my UTMOST gratitude to two great men, my research supervisors, Prof. Dr. Carlos Jacinto and Prof. Dr. Daniel Jaque, for their sincere and invaluable support, useful advice during my research, patience, intelligence, diligence and erudition. I am deeply thankful to them for their time, knowledge and experience shared. If one asked me a phrase to define what they mean for me, I would borrow the famous phrase from Isaac Newton and say "*If I have seen further it is by standing on the shoulders of Giants*". Prof. Dr. Carlos Jacinto was an incredible mentor whom was always encouraging and pushing me to go further. He fought for the best academic opportunities for his students, and has believed and given the honor for me to play my part. Prof. Dr. Daniel Jaque is amazing, he heartily extended his warmest welcome to me when I arrived in Spain and showed paternal care and attention during all my study period there. As a supervisor, he is an example, a mirror, always giving generous support and the warmest encouragement. Both of them are great men and friends, which I could share unforgettable terrific moments inside and outside of university. Being by their guidance was an honorable and glorious period. A great part of my intellectual debt is to both of them, so, I am really really grateful for the enormous contribution of them, because I am capable to see further.

At last, I wish to thank many other people whose names are not mentioned here, but they have helped a lot, for this reason, I will be always grateful to all.

List of abbreviations and acronym

BW ↔ Biological Window

BW-I ↔ First Biological Window/650-950 nm

BW-II (III) ↔ Second (Third) Biological Window/1000-1350 nm (1500-1800 nm)

NIR ↔ Near Infrared

NIR-II ↔ Second Near Infrared Window/1000-1700 nm

NPs ↔ Nanoparticles

NCs ↔ Nanocrystals

Ag_2S ↔ Silver Sulfide

Ag_2S NCs ↔ Silver Sulfide Nanocrystals

Ag_2S NPs ↔ Silver Sulfide Nanoparticles

Luminescence Transient Nanothermometry ↔ *LTNh*

Transmission Electron Microscopy ↔ TEM

High resolution transmission electron microscopy ↔ HRTEM

Scanning Transmission electron microscope ↔ STEM

Dynamic Light Scattering ↔ DLS

Lifetime-Based Luminescence Nanothermometry↔ LT-LNTh

1-dodecanethiol ↔ DDT, >98%

Polymethyl ether thiol ↔ PEG

SUMMARY

1 Introduction

1.1 Luminescence Nanotechnology

Technology is being implemented for the greatest part of aspect of our day by day lives such as communication, education, banking, purchasing, agriculture, security, biomedicine and so on. The world is clearly showing to keep on developing and the science has been demonstrated to be a bridge and a crucial tool to develop and stay up-to-date new emerging technologies. Among all them, the using of luminescencent nanomaterials defining a specific sub-group of technology, called based-luminescence nanotechnology, has been so far one of the greatest promising areas of technological developments for applications in several different fields of our daily lives. One of the most beautiful and notable application of this nanotechnology is addressing to biomedice, from research to clinical practices. Diverse range of applications including smart drug-delivery vehicles, noninvasive therapies, early diagnosis of diseases and biosensing in general, has been capable of being assessed thanks to the development of luminescence nanotechnology. [1]

By point out briefly a few early remarkable momentous about the luminescence roots, the firs0t reported investigations about luminescent materials were performed by the Italian alchemist and cobbler Vincenzo Cascariolo. He fabricated a powder through a heat-up synthesis of mixture of barium sulfate and coal that exhibited, after being exposed to sunlight, a bluish glow at night. [2] Nevertheless, luminescence term first time comes up to light as ***luminescenz*** by the German physicist/science historian Eilhard Wiedemann in 19th century. He defined luminescence as all phenomena of emitted light that are not exclusively restricted by rising up the temperature, that is, not following the same rule of a thermal radiation like incandescence.[3] Up to now, luminescence is stated as a process of a spontaneous emission of radiation from an electronically excited species (or from a vibrationally excited species) not in thermal equilibrium with its environment. Luminescence subgroups are classified depending on the excitation mode, they include so far: Chemiluminescence, bioluminescence, electroluminescence, cathodoluminescence, radioluminescence, sonoluminescence,

thermoluminescence and photoluminescence. In photoluminescence the emission is thanks to a direct excitation of electrons to a higher energy level in an atom of a material after the absorption of photons.[4]

In 1852 one major event in photoluminescence history happened due to the observed results and the introduction of the term ***Fluorescence*** by George G. Stokes.[4] Since then, fluorescence spectroscopy is considered one of the most widely technique and/or technology applied in several distinctive, although commonly connected, fields. The light-matter interaction shows to prove the powerful capability of fluorescence materials to monitor molecular interactions in biological and biochemical essays, including one of major by monitoring cellular events and sensing cellular response, allowing detection of aberrant behaviors [5]. In 1941 a first pioneering published work concerning fluorescent nanotechnology applied as a direct approach in pathogenesis study was realized by Albert Coons that tracked and visualized the β-anthryl-carbamido antibodies using the fluorescence behavior of Type III pneumococci rendered by the own antibody.[6] Over last decades the fluorescent materials working in partnership with advanced detection technologies (as detectors, optical devices, excitations sources, smart analysis software and so on) play major role in modern sensing. The analysis of information behind light-matter interaction are continuously being updated making possible improvement of the technique, leading towards clinical medicine uses. High selectivity and sensitivity is one of great advantages of using fluorescence optical method for biosensing, working as a powerful tag that enables to determine location, structure and dynamics of molecular events within living cells.[7]

1.2 Biomedical Fluorescence Imaging Technique

Labeling in biological medium through Fluorescence are also recognized as *Biomedical Fluorescence Imaging Technique*, and are used routinely in clinical practice as they well-provide physiological information of organs and living tissues. It is a contactless approach allowing diagnosis and prognosis of different diseases and for these reasons they have gained increasing importance in clinical and medical research. By far the most used well-established imaging techniques considered to be stronger competitors in respect to fluorescence are also non-invasive approaches, including computed tomography (CT), or single-photon emission tomography (SPECT), magnetic

resonance imaging (MRI) and ultrasonography (Echo). However, some drawbacks like the dangerous effect of the ionizing radiation (CT, PET and SPECT) or the limited spatial resolution (MRI, Echo and PET), poor temporal resolution (CT, MRI, PET and SPECT), complex and expensive instrumentation restrict their access to third-level Hospital.[8] Some of these drawbacks are overcome by near infra-red (NIR) fluorescent imaging. This technique can be used in real time acquisitions at a cellular resolution level using low energy photons. The simplicity of the instrumentation and the high spatial and temporal resolution have facilitated for instance its use in medical research where animal models are used to study the localization and the evolution of the diseases [8] facilitating the translation from research to the clinical practice.

1.3 NIR-II Ag_2S and others remarkable fluorescent contrast agents and thermal biosensors

The development and exploration of new multifunctional nanostructures capable of emitting in the so-called biological windows (BWs) has attracted much attention in recent years, especially for being a promising emerging nanotechnology of accessing information about biological environments through *Fluorescence-Based Optical Imaging*. Indeed, they are near infrared (NIR) agents particularly outstanding for probing deep into living tissues [9]. Nowadays there are extensive efforts focused towards the development of nanostructures, especially because those emitting within of the second and third biological window (BW- II and III) fluorescence imaging present better performance over visible (450-650 nm) and traditional NIR-I imaging (650-950 nm). As a consequence of that, light in this spectral range is weakly absorbed and scattered by tissues, thus allowing for acquisition of deeper tissue penetration and lower auto-fluorescence from living tissues (taking account their biological components, such as hemoglobin, deoxyhemoglobin, melanin, fat content, water and others).

Many multifunctional nanostructures (or even simplest ones) have been proposed with signals of intention of improvements to enhance the quality of obtained fluorescence bio-images. Among them, fluorescent dyes have assumed the leadership at beginning because of their biocompatibility and the capability of monitoring biomolecular interactions. It is possible through observed changes in their colors and brightness in response to changes of their environment properties, being so-called

environment-sensitive dyes.[10] As an example, the clinically approved ICG has shown great results in vivo biodistribution essay and in vivo cancer imaging. [11] However organic dyes present some disadvantages like limited fluorescence detection due to the limited extinction coefficients or quantum yields (QY) or even limited values concerning dye/reporter molecule ratios in a labeling reaction.[12]. For this reason a new era of nanotechnology, new super nanostrusctures have started to replace traditional organic dyes due to their superior optical properties. Additionally, the capability of controlling their size and/or shape becomes one profit, promoting higher sensing assay throughput.

Inorganic/organic core-shell of rare earth (RE) doped luminescent nanoparticles (means build up of two or more nanomaterials, also defined as multiple-nanostructure) have shown up incredible advantages. One of the reasons is the flexibility of choice of different combinations of both organic and inorganic materials making possible to cover different applications proposes. A complex multifunctional superstructure based on active-core/active-shell Nd^{3+}- and Yb^{3+}-doped LaF_3 inorganic nanoparticles has showed good results of determination of physical properties of a living tissue by thermal relaxation dynamics after the tissue being subject to a heat stimulus. [13] Although the remarkable results in vivo, the complex core-shell structure and multi-level energy transfer diminishes their absorption to emission energy conversion efficiency and reduces the depths in subcutaneous tissue imaging, which requires improvements for clinical level applications. Semiconductor nanomaterials have emerged as a high contrast agent overcoming obstacles present in the previous reported structures. Some of them can be discard to be use in bioimaging due to the acute and chronic toxicity such as CdTeSe, CdHgTe, PbS.[14] This requirement limits the available alternatives to few materials, single walled carbon nanotubes (SWCNTs)[15] and Ag_2S nanoparticles[16] are the remarkable ones. These two probes could be considered promising candidates for NIR fluorescence imaging due to its negligible toxicity. However, the big size of the SWCNTs (typically between 100 to 200 nm) when compared with sub-10 nm nanoparticles reduces its cellular uptake and tissular permeability.[17]

The NIR-II silver sulfide nanodots (NIR-II Ag_2S nanodots) overcome all limitations previous described, show absence of heavy metals (Cd, Hg, or Pb), high photochemical stability, biocompatibility (demonstrating a lack of noticeable toxicity),

emission lines in the second near infrared window (NIR-II, 1000-1700 nm) and ability to be capped by surfactants or capping agents.[14, 18] This last property making this material highly promising for biological applications. For example, multiple challenging tasks have already been proposed and reported using NIR-II Ag_2S nanodots because of their multifunctional ability, being nanoheaters (ability of efficiently convert absorbed light into thermal loading), thermal sensor (commonly based on fluorescence properties like fluorescence lifetime, emission intensity and spectral shift) and biosensing (fluorescence properties changes in response to changes of biological medium). Their properties and multifunctional ability have been exploited for multiple-disciplinary applications, including subcutaneous and transcranial thermometry, tumor labelling and diagnosis and dynamic imaging of the cardiovascular system.[18-19] Some of these successfully reported goals were achieved by the investigations carried out in this thesis, as will be further described. The temperature dependency of luminescence properties, associated with the thermal sensing feature of our Ag_2S nanodots, making them an excellent candidate for application in the well-known field of *Luminescence Thermometry*. Interesting to mention is that the luminescence thermometry performance of our Ag_2S nanodots was the essential tool for the development and to deal with the multiple challenging applications concerned in vivo or ex-vivo subcutaneous thermal gradients reading. These achievements enabled us even to detect abnormalities induced in living tissues [19a, 19c]. Another so desired goal during the development of this thesis was to achieve the best NIR-II luminescence performance of Ag_2S nanodots in order to make them reliable to clinical applications stage. These improvements were achieved by means of physical-chemical nanoengineering induced during application of an ultra-fast laser. In summary, the major goal of this thesis was to tackle the use of Ag2S nanodots for different applications, by modifying their structure to make them compatible with relevant proposed tasks and unsolved application so far. The findings presented here, with no doubts are to promote future possibilities no one would have ever dreamed of not so long ago.

1.4 Relevant features of Ag_2S. A brief description

This section will be focus in some relevant properties about the semiconducting silver sulfide (Ag_2S). Ag_2S is one of the most required among the sulfides due to its interesting properties. The Ag_2S is the only semiconducting sulfide (except for HgS)

having three polymorphous modifications (α-Ag_2S, β-Ag_2S and ϒ-Ag_2S) associated with different temperatures. The semiconducting-phase α-Ag_2S (acanthite) exists temperatures below ~ 450 K, and has a monoclinic crystal structure. The cubic phase β-Ag_2S (argentite) exists in the temperature range of 452-859 K, and has a body centered cubic (bbc) sublattice of sulfur (S) atoms and has a superionic conductivity. The cubic ϒ-Ag_2S phase with a face centered cubic (fcc) sublattice of S atoms is stable from ~ 860 K up to melting temperature [20]. The most remarkable one is α-Ag_2S, and we shall focus in this one, calling it simple by Ag_2S. In normal conditions, Ag_2S structure is a direct semiconductor material which presents a narrow band gap (E_g) of 0.9-1.1 eV at room temperature (300K), although it changes as a function of temperature. This temperature change, named *temperature coefficient*, is found to be $\frac{\partial Eg}{\partial T} = -(1.2 - 1.5) \times 10^{-3} \mathrm{eVK}^{-1}$[20].

The temperature influences comes from distinct parameter, they can be listed as: Thermal expansion (contributions from size dependence and wave-function envelope) mechanical strain and electron phonon coupling[21]. Such temperature dependency is not only exclusively related to Ag_2S nanocrystals (NCs), but for a larger number of semiconductor materials[21]. Detailed studies showed the fluorescence temperature dependency of Ag_2S NCs (with average diameter of 4 nm), demonstrating a remarkable decrement in the energy band gap as the temperature goes up [22]. The major contributions is believed to be related to the thermal expansion of the crystal lattice and the electron phonon coupling[22]. The thermal expansion increases the crystal lattice constant and the energy band gap decreases proportional to this change. On the other hand, the effect of the temperature on the electron-phonon coupling depending of the phonon energy (which takes into account the environment) and the state density. Both variables increase as the temperature increases[21]. The mentioned phenomenon exhibits a peculiar property of these nanoparticles; the possibility of measuring the temperature by means of redshift of its emission peak is a reality. Indeed, it was proved several times, including using other luminescence parameters such as lifetime, peak ratio between two emissions and so on [19a, 19c, 22].

In general, the size of semiconductor nanocrystals plays roles in both energy band gap and its temperature dependency. Indeed, as the size decreases, confinement effects arise and larger is the band gap energy found. [19c]. The quantum confinement

effect also affects the temperature dependency of the band gap, but only is relevant in the quantum dot regime[21]. The electron and hole effective masses associated with bulk coarse-crystalline acanthite α-Ag_2S are $0.286m_0$ and $m_h = 1.096m_0$, respectively. Based on this information the radius of the first exciton state (main quantum number n = 1) é about $(26 \pm 1)a_B$ or ~ 1.4 ± 0.1 nm. Where a_B is the well-known Bohr radius found to be $52.9\ pm$ [20]. Ag_2S structure can be synthesized by different synthesis methods and which one produces Ag_2S NCs with different sizes (from 1.5 to 10 nm) [23]. Indeed the authors have done[23] a thorough study in literature and found that strong variations in the emission peak position are observed for Ag_2S NPs with sizes below ∼4 nm. On the other hand, those with sizes above 4 nm present emission peaks localized between 1050 and 1250 nm. The reason of this behavior is related to the previously mentioned quantum confinement effect. Indeed, for particles larger than 4 nm, no quantum confinement is observed, and photons with energy around 1200 nm (E_g of 0.9-1.1 eV) are expected. On the other hand, for those smaller than 4 nm, the quantum confinement plays effect, leading to larger band gaps and, as a consequence, photons with higher energy are emitted (blueshift of the emission as decreases the size).

Ag_2S NPs has been investigated intensively in recent years due to possible application in optoeletronics, biosenging and catalysis. It is an excellent substance for the preparation of heterostructures. Ag_2S NPs has been successfully produced by different methods such as hydrochemical deposition, template method, sol-gel method, synthesis in microemulsions, as well as by sonochemical, hydrothermal, solvothermal, electrochemical, microwave and other techniques[20]. Every methodology aims for specific targeting purposes. But is worth to mention that structural and optical properties are critically affected by the synthetic methodologies. For example, those synthesized by using decomposition of metallic salts in nonpolar media (1-dodecanethiol, for example) usually present emission centered at around 1250 nm. In contrast, the majority of those synthesized by using polar media (water, for example) yield Ag_2S NPs with blue shifted emission bands (500-1300 nm) and larger size tunability[23].

The mentioned behaviors and phenomena show that there is a high impact of the structural features on the luminescence ones. The mentioned behaviors and phenomena show that there is a high impact of the structural features on the luminescence ones. Additionally, the production methodology plays a strong effect on the structural feature

and, by means of a reaction chain, on the luminescence. So, it is important to focus on the synthesis route that provides that best material aiming a specific goal. As we have mentioned, each one shows the advantages and limitations. On this thesis we have focused, as we are going to describe in details on those based on decomposition of metallic salts in nonpolar media, providing emission in the near infrared region for biological purposes.

2 Material and experimental set up Section

2.1 Material Section

In this section the synthesis procedure or the origin of the materials used in this thesis is described. Note that some materials were not studied deeply, some of them were only investigated superficially in order to compare with the main materials investigated in our already published or current works in development at this very time moment. The main material investigated here was the semiconductor Ag_2S nanodots. The goals of our work were focused to optimize their ***Optical and Structural Properties*** via best synthesis route procedure as well as outstanding applications in ***In Vivo NIR-II fluorescence Imaging*** as well as ***Luminescence Nanothermometry***, both techniques recognized to be potential tools for the disease recognition, such as malignant tumors, tissues` abnormalities and cardiovascular diseases.

Several synthesis routes were applied to manufacture the final product of Ag_2S nanodots and different applications were reached with them. In the next sections we are going to point out the chemicals and synthesis procedures for each one and the respective applications, however deeper description regarding each one can be seen in the results ***in Chapter 3 Results and discussions***.

2.1.1 Materials

2.1.1.1 Chemicals and Synthesis of Ag_2S nanodots for Lifetime Based Luminescence Thermometry in the Near Infrared Second Biological Window

- ***Chemicals***

Silver(I) diethyldithiocarbamate (AgDDTC, 99%), 1-dodecanethiol (DDT, >98%), 1-octadecene (ODE, 90%), poly(ethylene glycol) methyl ether thiol (PEG-SH, average Mn 6000), tetrachloroethylene (TCE, >99), dichloromethane (DCE, 99.8%) and toluene (99.8%) were purchased from Sigma-Aldrich. Absolute methanol (99.8%) was purchased from Scharlau.

- ***Synthesis of PEG-SH -Ag2S and DDT- Ag_2S nanodots***

In this work, the synthesis of Ag_2S NCs is based on the thermal decomposition of silver(I) diethyldithiocarbamate in the presence of 1-dodecanethiol. The syntheses have been performed with standard Schlenk lines using a temperature controller connected to a PC unit for accurate and reproducible results. For each synthesis, 0.05 mmol of silver(I) diethyldithiocarbamate,12.5 mmol of 1-dodecanethiol, and 9 mmol of 1-octadecene were mixed in a three-neck round bottom flask and degassed under vacuum at room temperature. The flask is then backfilled with nitrogen and heated up to 200 °C at a rate of 17 °C min−1. The solution is stirred for one hour at 200 °C and then cooled down using a water bath. After the synthesis, the black colloidal dispersion is washed in several cycles of precipitation with methanol and re-dispersed in toluene.

- ***Ligand exchange procedure from DDT ligands to PEG-SH***

In order to obtain water-soluble Ag_2S NCs, the hydrophobic DDT ligands are exchanged with PEG-SH. In a typical procedure, a toluene dispersion of the NCs is precipitated with methanol and centrifuged. The supernatant is discarded and 1 mg ml^{-1} solution of PEG-SH in dichloromethane is added onto the NC deposit. The mixture is sonicated at room temperature for an hour. After that, the NCs are isolated and transferred to water. The water dispersions present good colloidal stability.

2.1.1.2 Chemicals and Synthesis of Ag_2S nanodots for Tumor Detection based on Luminescence Transient Nanothermometry (LTNh)

- ***Chemicals***

For surface biofunctionalization purposes the following chemicals were used: 1-dodecanethiol (DT, 98%, aladdin), dihydrolipoic acid (DHLA, 98%, Alfa Aesar), poly(ethylene glycol) (PEG, 90%, SunBio), ethyl(dimethylaminopropyl) carbodiimide (EDC, commercial grade, Sigma), N-hydroxysuccinimide (NHS, 98.5%, Sigma). Other chemicals including AgNO3 (AR), dimethyl sulfoxide (DMSO, AR), (C2H5)2NCS2Na·3H2O (Na(DDTC)), ethanol (AR), and cyclohexane (AR) were purchased from Sinopharm Chemical Reagent Company.

- ***Synthesis of PEG-COOH-Ag_2S nanodots***

In this work the Ag_2S nanodots were synthesized by Sinano Company (China). The synthesis procedure has been reported in some previous works [19d, 24], where the manufactured NIR-II PEG-COOH-Ag_2S nanodots has shown good biocompatibility, controllable size and negligible cytotoxicity.

2.1.1.3 Chemicals and Synthesis of Ag_2S Dot-to-Superdot transformation triggered by femtosecond laser pulses

- ***Chemicals***

Ethanol, n-hexane (95%), Silver nitrate, L-Cysteine, diethyldithiocarbamate (DDTC), chlorophorm, HS-PEG-COOH (2100 g/mol) were purchased from Sigma-Aldrich (St.Louis, MO) and used as received.

- ***Synthesis Neat Ag_2S***

The synthesis of the neat Ag_2S was carried out by thermal decomposition of the precursor silver diethyldithiocarbamate (AgDDTC). The precursor was synthesized as follows: 0.025 moles of $AgNO_3$ was dissolved in 200 mL of bidestillated water produced from milliQ water. Later 0.025 moles of DDTC (dithyldithiocarmabamate) was dissolved in 300 mL of bidistillated water and added to the above solution. The resulting yellow powder was filtered and dried at 60 in vacuum using the Rotavapor. After that, 0.025 mg of AgDDTC was dispersed in 5 mL of 1-dodecanethiol and the mixture was stirred under vacuum for 30 minutes. After that, the solution was heated up to 200 ºC for 1 hour. After this time, the solution was cooled down naturally. When the mixture temperature reached 25ºC, 10 mL of ethanol was added and the solution was centrifuges at 10.000 rpm for 10 minutes. The supernatant was discarded and the precipitated collected in 10 mL of $CHCl_3$. The final concentration of the produced nanoparticles was 1 mg/mL. The **Fig. 2.1a** shows a TEM picture of the as produced neat Ag_2S. EDS spectrum of the nanoparticles unveils the atomic ratio Ag:S of 2:1, characteristic for Ag_2S nanocrystals, **Fig. 2.1b**.

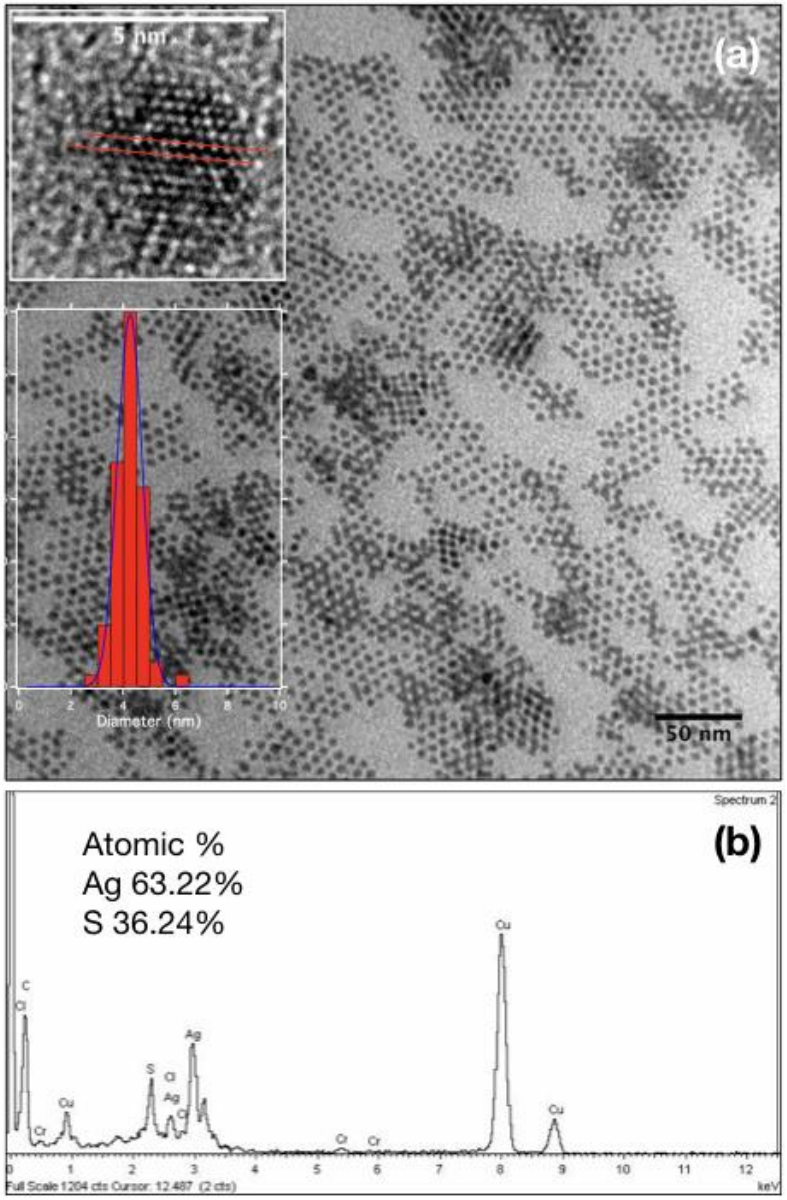

Figure 2.1 (a) TEM micrograph of the neat Ag_2S nanoparticles produced by thermal decomposition of AgDDTC. The upper inset depicts a HR-TEM of a single nanoparticle, showing the lattice fringe d_{022}=2.5Å. The inset bellow shows the size distribution of the nanoparticles centered at 4 nm of diameter. **(b)** EDS spectrum of the nanoparticles.

- ***Synthesis of Ag/Ag_2S heterodimers***

Ag/Ag_2S heterodimers are prepared as follows; 3 mmol of silver nitrate is poured into a round bottom flask containing 10 mL of octadecylamine at 160ºC under gentle stirring and N_2 atmosphere. After 10 minutes the mixture acquires a metallic blue color, at this stage 1.5 mmol of L-cysteine is added to the mixture as sulfur source. As result, the color of the mixture turns from blue to black indicating the formation of the heterodimer (30 minutes). Then the sample is cooled down and the product of the

reaction is dissolved in 40 mL of $CHCl_3$. This solution is centrifuged at 25.000 rpm for 30 minutes and the precipitate is collected and dispersed in $CHCl_3$ at a concentration of 1 mg/mL.

- ***Preparation of ultrafast transformation from Ag_2S dots into Superdots.***

The synthesis of Ag/Ag_2S heterodimers as described above gives as side product silver nanoparticles. The presence of these nanoparticles is due to the high redox potential of silver ions under the reaction temperature, resulting in the production of Ag nanoparticles.[1] With the aim of get rid off these nanoparticles, laser treatment was performed using $CHCl_3$ as reaction solvent. Preliminary studies carried out by our group have demonstrated that this process permits transforming Ag nanoparticles into AgCl particles, which are colloidally unstable and easy to remove (see **Fig. 2.2**). For that, a $CHCl_3$ dispersion of the previously synthesized Ag/Ag_2S heterodimers at a concentration of 1 $mg \cdot mL^{-1}$ is irradiated with Ti:Sapphire amplifier operating at 808 nm wavelength, giving as result Superdots. The laser provides laser pulses with a repetition rate of 1 kHz with a variable pulse widths between 50 and 550 femtoseconds. During irradiation real time NIR-II emission is continuously registered by a fiber coupled spectrometer.

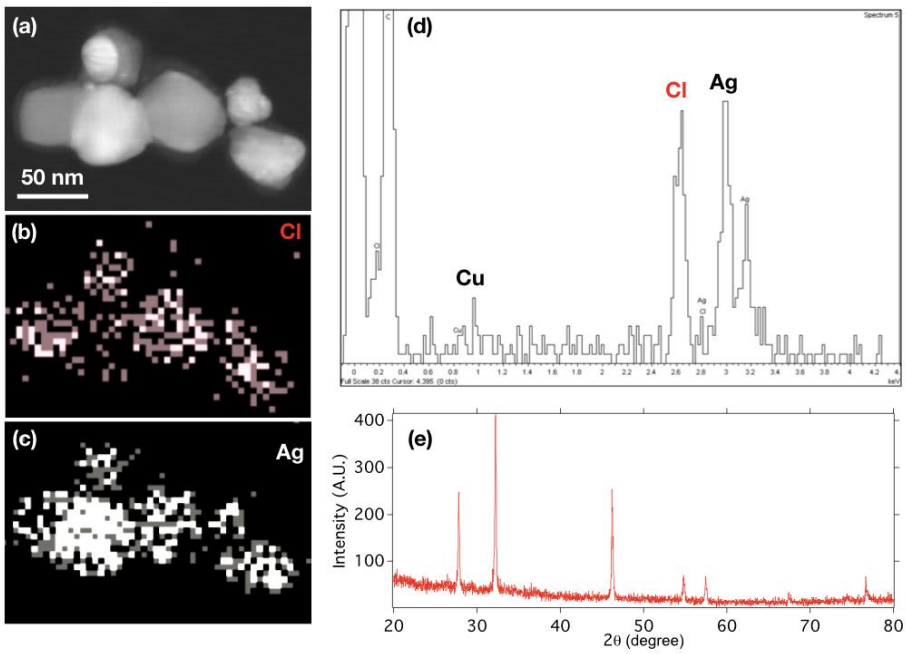

Figure 2.2. **(a)** STEM micrograph of AgCl nanoparticles obtained by ultra-fast laser irradiation of the sample. 2D EDS mapping of the spatial distribution of **(b)** Cl and **(c)** Ag reveals that these nanoparticles

are basically constituted by AgCl. This result is further confirmed by EDS analysis, Fig.S2d. XRD analysis of the sample shows the typical reflection of cubic AgCl crystals.

- ***PEGylation of superdots for in vivo imaging***

After irradiation, the sample containing superdots is centrifuged at 5.000 rpm and the precipitate (identified by EDS and X-Ray diffraction as cubic AgCl, see Fig 2.2) is discarded. The supernatant is then mixed with 0.5 mL of anhydrous ethanol and centrifuged again at 25.000 rpms. The supernatant is discarded and the precipitate re-suspended in 1 mL of $CHCl_3$ containing 1 mg of HS-PEG-COOH and sonicated in an ultrasonic bath at 20°C, 10 minutes. The product of this reaction is centrifuged at 25.000 rpm and the precipitate dispersed in phosphate buffer saline solution.

2.2 Physical and structural characterization of Ag_2S dots

In this section the *physical* and *structural characterization of Ag_2S dots* obtained by different synthesis routes and for different applications is explored and described. As before, not all materials were deeply studied, depending on the main focus of the work.

2.2.1 Transmission Electron Microscopy (TEM)

The size dimensions and geometry of our synthesized nanodots Ag_2S dots were determined. The transmission electron microcopy (TEM, TECNAI G274 with resolution of 0.2 nm are illustrated in **Fig 2.1a**) was employed to characterize the PEG-SH- and DDT-Ag_2S nanodots applied for ***Lifetime Based Luminescence Thermometry*** as well as PEG-COOH-Ag_2S ***Tumor Detection based on Luminescence Transient Nanothermometry (LTNh)*** the results can be found in the discussion of the ***Chapter 3. Results and discussions Section 3.1 and 3.2***, respectively. The equipment belongs to the medical center of Universidad Autónoma de Madrid. Some steps were followed in order to prepare the samples for TEM measurements, they are:

- For preparing the TEM samples some materials are request to follow the appropriate protocol such as parafilm sheet, the copper grids and a pair of small clean brussel stainless steel tweezershe (see **Fig 2.1b)**.
- Place the cooper grid, oriented upwardly, on the Parafilm, and deposit a drop of 15 µL of sample on it for 1 to 2 minutes (see **Fig 2.1c)**. Then, dry the sample with a piece of blotting paper (see **Fig 2.1d)**.
- Clean the cooper grid with 300 µL of milli-Q water and then dry the sample with blotting paper (see **Fig 2.1e)**. This is a particularly needed step since salts coming with the buffer are removed.
- Dry the sample under the hood for at least 30 minutes.
- The grids-sample are placed on a sample holder subsequentenly being inserted in the observation chamber of the TEM system.
- Finally the TEM images were captured in randomly selected regions of the surface of each plate. The software Image J was used in order to calculate the

average size value of the nanodots thorough statistical analyzes and a subsequently Gaussian fit.

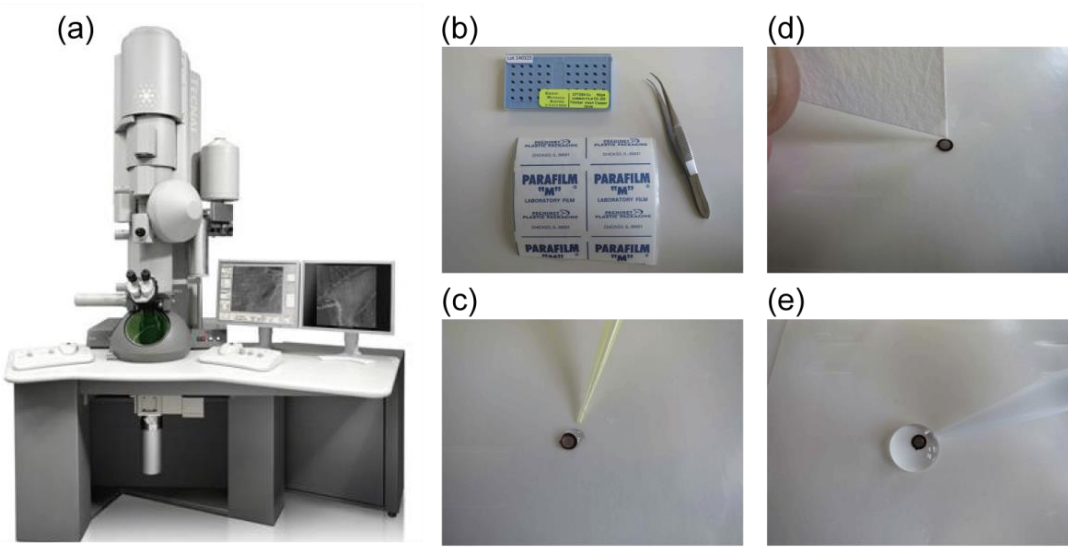

Figure 1.1. (a) FEI Tecnai G2-F20. **(b)** Materials used in sample preparation. **(c)-(d)** Protocol description of sample preparation.

2.2.2 High resolution transmission electron microscopy (HRTEM) and Scanning Transmission electron microscope (STEM)

Atomic resolution characterization was performed on a JEOL JEMARM200cF electron microscope (Cold Emission Gun) operating at 80 kV provided with a spherical aberration corrector in probe, a GIF-QuantumER spectrometer and an Oxford INCA-350 detector. Atomic resolution STEM-HAADF images were acquired using inner and outer collection semiangles of 68 and 280 mrad and a nominal camera length of 60 mm. In order to get the highest possible intensity in the XEDS detector without affecting the sample, we determined that the optimum conditions were achieved by using a condenser lens aperture of 50 micrometers and a spot size of 6. In these conditions the probe current is well above 120 pA. The camera length for the STEM images was set to 6 cm o that the collection angles range is from 90 to 370 mrad.

Figure 2.2. JEOL JEMARM200cF electron microscope.

2.2.3 Hydrodynamic diameter and Z-potential

- ***Dynamic Light Scattering (DLS)***

The hydrodynamic diameters of the Ag_2S nanodots were measured in a Zetasizer Nano ZS (Malvern) using a standard 1 cm plastic cuvette that contained a dispersion o the nanodots at a concentration of 0.1 mg/mL in water. Accumulation times for each sample were determined automatically, at selected temperatures. The correlation function was used to calculate the z-average (intensity mean) and hydrodynamic diameter (Dh) using the Einstein–Stokes equation. These results were calculated by selecting the multimodal analysis method of the DTS software (5.0) provided by Malvern

- ***Z-potential***

The Z-potential measurements were performed using a Zetasizer Nano ZS instrument (Malvern Instruments, U.K.), and the accumulation time was determined automatically for each sample. The acquired data was processed using the software provided by Malvern (Zetasizer software v7.03).

Fig. 2.3. Zetasizer Nano ZS instrument (Malvern Instruments, U.K.)

2.2.4 Fourier Transformer Infrared spectroscopy (FTIR)

In the present results, *FTIR* spectra were registered using a Nicolet Thermo scientific IR 200 FT-IR, using acquisition software setting in a static mode of 100 accumulations. The technique consists to produce discs from a mixture of potassium bromide (KBr) and Ag_2S nanodots containing 150 mg and 30 μg, respectively. Due to the high hygroscopic characteristic of KBr, it was kept in a stove at an adequate temperature in order to avoid water absorption induced by the sample being in contact with atmosphere air. All procedures were done carefully, minimizing the water absorption and impurity contaminations from surrounds.

- KBr, espectroscopic degree (P/N 202-34141).
- Weighing-machine, spreader (precision of four decimal places) and ethanol.
- Mortar and a pistil were used to crush the mixture of nanoparticles and Kbr in order to obtain a uniform distribution.
- Disc mold to shape the product in a disc shape (P/N 202-32010).
- Hydraulic pressure (P/N 200-64175). A pressure of 60 atm was applied under the sample during the time interval of 10 min.

Fig. 2.4. Nicolet Thermo scientific IR 200 FT-IR.

2.3 Optical characterization

The techniques and instruments used for providing information about the optical properties are described in details in this section. Some techniques were obtained in different set up systems, however the obtained physical-chemistry information about the materials used in this thesis is the same.

2.3.1 Fluorescence Spectroscopy

For investigating the emissions spectra of Ag_2S nanodots functionalized with different coating and dispersed in varied types of solvents, where emitted photons of light were found to belong to the NIR-II region, a homemade microscopic was used as it can be described. To do so, all the samples were excited by using a fiber-coupled 808 nm laser diode (Lumincs) coupled with a collimator (Thorlabs PAFA-X-4-B). The laser beam was, after pass throughout a dichroic mirror range from (780-850), focused in a quartz cuvette filled with the distinct (aqueous or organic) dispersion of Ag_2S nanodots by using a microscopic objective (65X IR, numerical aperture of 0.65). The fluorescence emission was collected with the same microscope objective and, after crossing the same dichroic mirror playing the role of reflecting the excitation light. Then, the luminescence signal was spectrally analyzed by an Andor Shamrock 193i spectrometer, after passing through long pass filters of > 850 nm in order to filter any light corresponding to the laser, and collected by an InGaAs CCD camera (Andor IDus iDus DU490A). The Andor SOLIS software was used for the real-time record of the emission spectral.

As described before (***in Chapter 1. Introduction***), the Ag_2S is an excellent thermal sensor by inspection of temperature dependence of the luminescence properties. To investigate the changes in the fluorescence emission spectral, a thermoelectrically cooled Peltier plate (Linkam PE120) was used making possible to vary the temperature from -25-120 °C, with a thermal resolution of 0.1°C. The heating plate was mounted in the microspic stage in order to lay the sample above it to control its temperature as well as to place the sample on the focus of the *objective lens* to guarantee maximum signal.

2.3.2 Absorption Spectroscopy

The absorption spectrum measurements from the developed Ag_2S samples investigated in this thesis was carried out between 350 to 1500 nm by means of UV-Vis-IR instrument model Perkin Elmer Lambda 1050 spectrophotometer. The spectrophotometer is integrated with a photomultiplier for spectral detection in the visible range of 200-860 nm, a cooled InGaAs detector working in the range from 860 to 1800 nm and a Cooled Pbs detector with high sensitive in the range from 1800 to 3300 nm. The spectrophotometer system holds a spectral resolution of 0.2 nm.

2.3.3 Lifetime Spectroscopy

The lifetime spectroscopy technique used for obtain the results present in this thesis were carried out in two different experimental set up systems (Supervised by the *Grupo de Nanofotônica e Imagens (GNFI)* and *Figure Imaging Group (FIG)* at *UFAL* and *UAM*, respectively). In order to point out which corresponding system was used in the results presented in ***Chapter 3. Results and discussion Section 3.1***, it is worthy to name the systems followed by the respect description. ***System (a):*** The Fluorescence decay curves measurements present in this thesis, making possible to obtain the results wich can be found in the publication [25], were recorded using the Fluorimeter NanoLog™ (HORIBA) with double grating excitation and two emission monochromators. The detector used was a liquid-N2 cooled R5509-73 photomultiplier tube, operating in the 300–1700 nm range. Luminescence decay curves were obtained by exciting the colloidal suspensions of Ag_2S NCs by using a pulsed diode laser (HORIBA, model DeltaDiode DD-450L) operating at 450 ± 10 nm and providing pulses of 80 ps duration with a maximum repetition rate of 100 MHz. The fluorescence time decay curve was finally obtained with time-domain TCSPC using the Datastation software. For the measurement of decay curves at different temperatures, the sample was placed on a controlled temperature stage that was able to tune the sample's temperature between 20 and 60 °C with 1 °C resolution. Additionally, a long pass filter of > 850 nm was located in the entrance of the monocromator in order to filter any light that did not correspond to the Ag_2S samples. The complete description of the Fluorimeter NanoLog™ (HORIBA) system is described in the illustration in **Figure 1**. This system can be found at UFAL-Brazil and is supervised by Prof. Carlos Jacinto.

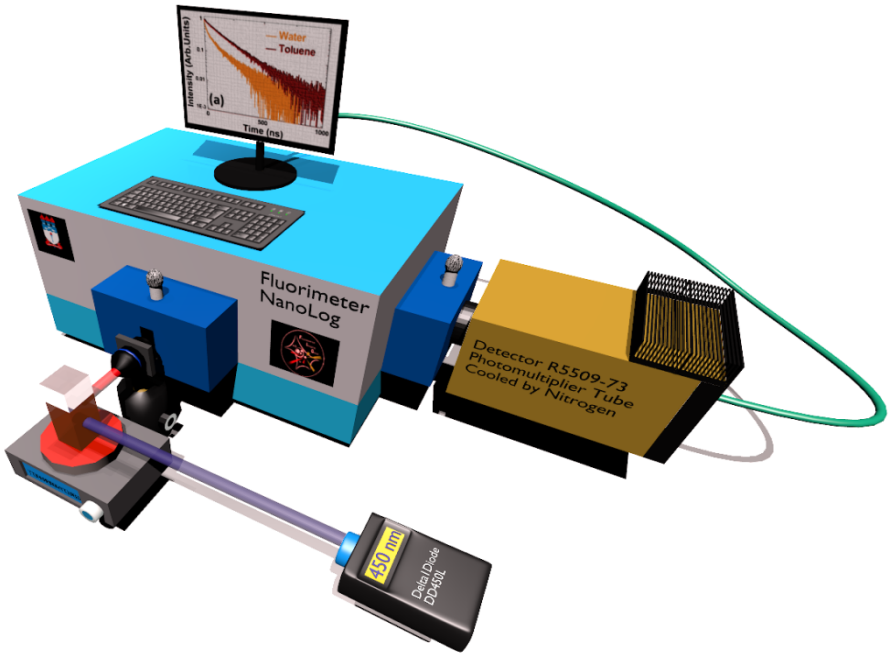

Figure 2.5 Illustrative description of the Fluorimeter NanoLog™ (HORIBA) system.

System (b): Luminescence decay curves were conducted by using an Optical Parametric Oscillator (Quanta Ray) coupled to a frequency tripled Nd:YAG laser operating at 355 nm. The Optical Parametric Oscillator, tuned to 800 nm wavelength, provides 8 ns pulses with an average energy of 0.2 J and a repetition rate of 10 Hz. The sample signal was collected and spectrally filtered by a high brightness monochromator (Shamrock 163 from Andor), after passing through long pass filters of > 850 nm in order to filter any light additional to that corresponding to the sample, and the time evolution was recorded with an infrared photomultiplier (Hamamatsu H1033C) connected to a digital oscilloscope (Le Croy Wave Runner 500), holding a frequency bandwidth of 500 MHz. This system can be found at UAM-Spain and is supervised by Daniel Jaque Garcia.

2.3.4 Quantum Yield Measurements

The absolute photoluminescence quantum yield (PLQY) has been measured by using a calibrated spectrofluorometer (Edinburgh Instruments, FLS920), equipped with an integrating sphere (Jobin-Yvon). A xenon lamp has been used as excitation source, filtered with a long-pass filter (610 nm) and a monochromator (wavelength: 800 nm, bandwidth: 20 nm) and the detector has been a liquid nitrogen cooled NIR photo-

multiplier tube (Hamamatsu, R5509-72). Details of the measurement procedure are described in reference [26], and the PLQY has been calculated as:

$$PLQY = \frac{\int Emitted\ Photons\ d\lambda}{\int Absorbed\ Photons\ d\lambda}$$

2.4 Numerical Simulations

Numerical solutions were developed in order to solve some mathematical model describing the physical phenomen observed experimentally during our studies. The numerical simuations were required since the mathematical models could not be solved through simple analytical solutions as most of them were found to be nonlinear systems. Here you are going to point out the physical problem and its respective numerical solution method applied.

2.4.1 Numerical simulations of heat equation in two-dimensions for non-homogeneous media.

The simulations of the temperature maps were obtained by solving the heat equation in two-dimensions for non-homogeneous media with internal heat generation, using a numerical scheme based on finite differences. Dirichlet boundary conditions were used at the computational edges, except at the material-air interface, where Newton´s law was applied. Thermal conductivity (κ), density (ρ) and specific heat capacity (c) for the substrate (s) and tissue (t) were taken as: κ_s = 1.05 W/(K·m)[27], ρ_s = 2200 kg/m^3 [ref], c_s = 700 J/(K·kg) [ref], κ_t = 0.412 W/(K·m)[ref], ρ_t = 1120 kg/m^3, c_t = 4340 J/(K·kg)[28]. For numerical simulation purposes, the computational window was divided with grid size of $\Delta x = \Delta y$ = 0.02 mm, where propagation time steps of Δt = 0.005 s give good convergence. In order to test the former experimental evidences on the influence of blood perfusion in the thermal relaxation of tumors, we have performed numerical simulations in a realistic computer mouse model using a transient solver that employs the finite-difference time-domain (FDTD) method, which allows a better local resolution of the calculations. A thermoregulation model based on the aforementioned Pennes bioheat equation is used,[3d] with a lumped term that includes $\boldsymbol{\omega_b}$, $\boldsymbol{\rho_b}$, $\boldsymbol{c_b}$ and $\boldsymbol{T_b}$, accounting for the *heat transfer rate*, i.e. the heat carried away by blood perfusion. More details about the mathematical model and method used, the boundary conditions and so on can be found ***Chapter 4. Supplementary data and information Section 4.2***.

2.5 In Vivo Near Infrared Second Biological Window Fluorescence Imaging System

For performing fluorescence images in vivo and ex-vivo samples, a homemade NIR-II imaging system constituted by Cooled (-45°C) InGaAs CCD camera (Xeva1.7-320) with high sensitivity in the IR spectral range (1000 – 1700 nm), two fiber-coupled 808 nm laser diode (LIMO20-F200-DL808) and heating plate (Digital Hot Plate Model PC-400D) were settling inside of a methacrylate black box as depicted in **Figure 1.2 (a)**. Such smart-arrangement enabled to avoid any undisireble signal or noise from outside. The heating plate was employed to keep the mice in a normal-body temperature that could be slightly lower or higher than 33°C. The laser fibers core used are around 400 µm and have a numerical aperture of 0.22. The lasers are capable of providing a power up to 10 W and working in pulsed and wave-continuous mode. The power density was regulated by change the distance between the light source (fiber-laser head) and the striked tissues (In vivo or ex-vivo), since the energy intensity is directly proportional to the square of the spot area, which can control by the distance or with a collimator. In the last case, the fiber-coupled 808 nm laser diode (Limo) was connected to a collimator (Thorlabs PAFA-X-4-B) in order to provide small-light spot for a well-defined localized light application depending on the goal of the experiment. Long pass filters of > 850 nm is placed between the objective lens and CCD of the InGaAs camera in order to cutoff light photons with wavelength lower than 850 nm. In **Figure 1.3 (b)** is showed the spectral response of our NIR-II imaging system taking into account the spectral response of the infrared fluorescence camera including the objective lens sensitivity, optical components and filters. The emission spectra of some well-know and used materials in this thesis are also included, such as ICG, $NaGdF_4$@Nd-Yb:NPs, SWNTs and Ag_2S. As can be clearly seen, the emission spectra of Nd-Yb:NPs, SWCNTs and Ag_2S nanodots show a significant overlap with the spectral response of our NIR-II imaging system. However, the FDA approved ICG dye for clinical applications have a spectra emission lying out of the spectral sensitivity range of our NIR-II imaging system. So, we discard the use of ICG for advanced further comparisons.

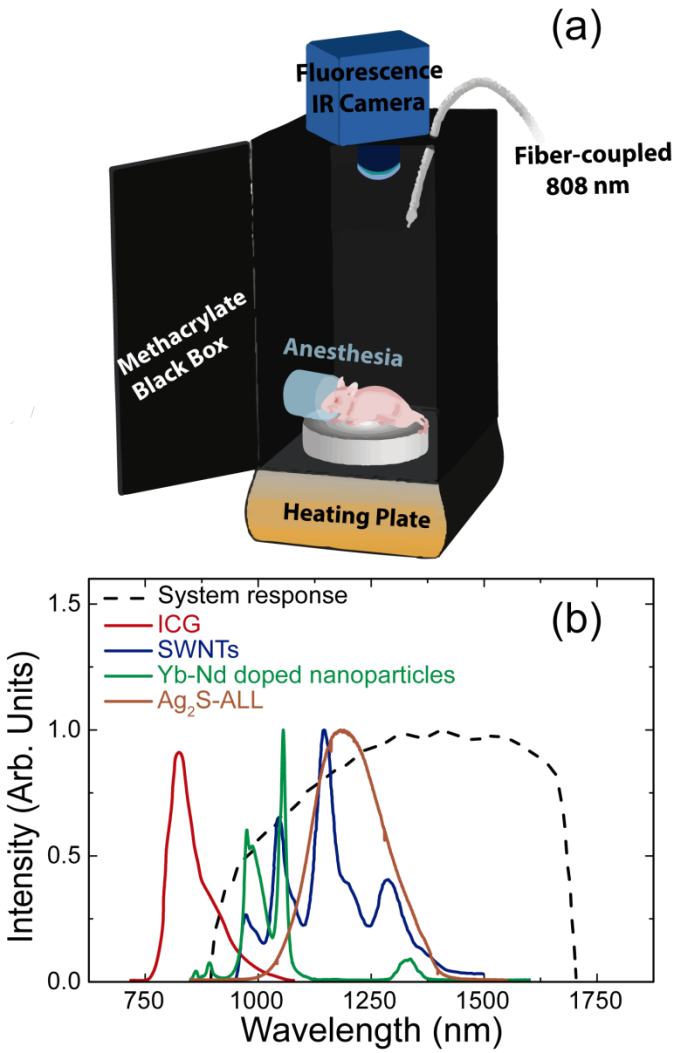

Figure 2.6 NIR-II imaging system for in vivo and ex-vivo applications. **(a)** The squematic illustration of the homemade NIR-II imaging system constituted by Cooled (-45°C) InGaAs CCD camera (Xeva1.7-320) with high sensitivity in the IR spectral range (1000 – 1700 nm), two fiber-coupled 808 nm laser diode (Limo) and heating plate (Digital Hot Plate Model PC-400D) were settling inside of a methacrylate black box. This fig. was adapted from the **thesis** [28a]. (b) Spectral response of our NIR-II imaging system taking into account the spectral response of the infrared fluorescence camera including the objective lens sensitivity, optical components and filters. The emission spectra of some well-know and used materials in this thesis are also included, such as ICG, N@Nd-Yb:NPs, SWNTs and Ag_2S.

2.6 Surface Temperature Distribution Feedback by Infrared Thermography

The reading of the surface temperature distribution, also known as thermography technique, is capable of determining the temperature distribution of an object exposed to heat, after absorving heat provided by a laser source, heating plate, transferred from nanoparticles that shows photothermal effect or whatever. Mainly in vivo and ex-vivo experiments were carried out, where living or ex-vivo tissues were subjected to a heat and the surface readout was possible by using the infrared thermographic camera. The thermal camera makes also possible the temperature readout for photothermal efficiency of nanoparticles studied in this thesis that present such effect. The acquisition thermal image system used was FLIR E40 bx. This camera was remotely controlled through FLIR Tools software and had an accuracy of 2 ° C in the -20-120 ° C range.

2.7 Blood Perfusion Imaging using Laser Speckle Fundamental

The moorFLPI-2 blood flow imager uses the laser speckle contrast technique to deliver real-time, high-resolution blood flow images, providing outstanding performance in a wide range of applications. User-friendly features promote smooth workflow and enable the high through-put required to scan cohorts quickly and accurately. The technique uses a Near-Infrared diode laser of 785 nm to produce light-matter interaction in order to get speckle images. Also uses an aiming beams red laser diode of 650 nm just for focus. The images acquired can have dimension from 5.6mm x 7.5mm up to 15cm x 30cm (continuously variable with zoom lens). The camera resolution is from 576 x 748 / 116 x 150 (spatial mode) up to 580 x 752 (temporal mode), with acquisition modes of single point (16 channel), single image and video mode. Being able to monitor optical zoom and auto focus through motorised system, holding a single camera/RGB illumination to match colour photo and blood flow images.

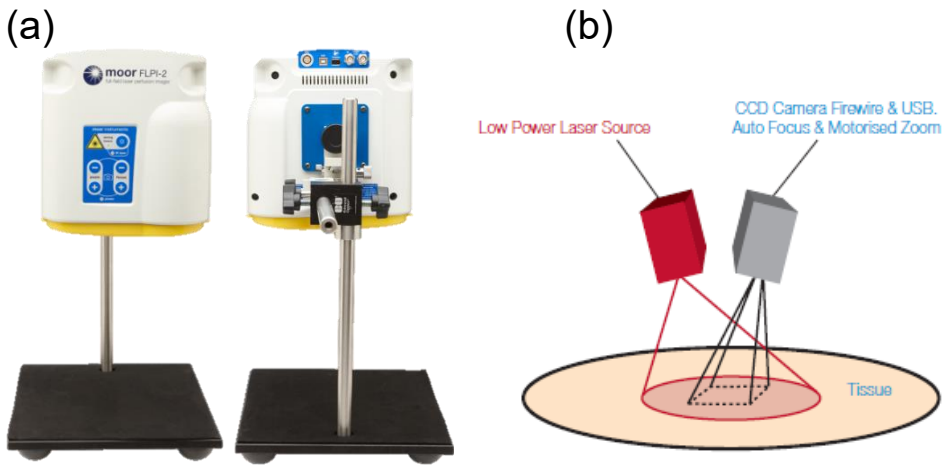

Figure 2.7 (a) The moorFLPI-2 blood flow imager**. (b)** Schematic description as the speckle images are obtained using an incident laser of 785 nm to interact with a living tissue.

2.8 In Vivo Essay: Disease Detection and Nanoparticles Tracking via NIR-II Bioimaging

Animal's models were used for several types of experiments concerning nanoparticles applications. In vivo essay was carried out in order to determine the efficiency of the nanoparticles for ***In Vivo Biomaging*** making possible diseases detection as well as to quantify the reliability regarding cytotoxity.

- ***Luminescence Transient Nanothermometry (LTNh)*** *technique was one of the most important technique explored in this thesis. The nanothermometry ability of Ag_2S nanodots opens up the incredible possibility of detecting tumor as well as to discriminate its stages.*

- ***Subcutaneous NIR-II Fluorescence imaging and Intravenously Injected Nanoparticles Biodistribution*** *capability of the different nanoparticles studied in this thesis was also explored. It is important to remember that we have synthesized Ag_2S by using different routes in order to improve the luminescence properties as well as to promote functionalization on the surface for specific targeting purposes.*

2.8.1 Animal studies

In vivo experiments were approved by the regional authority for animal experimentation of Comunidad de Madrid and were conducted in agreement with the Universidad Autónoma de Madrid Ethic Committee, in compliance with the European Union directives 63/2010UE and Spanish regulation RD 53/2013.

The In Vivo Essay Procedures in which the mice were exposed during the experimental investigations were conducted and supervised by the responsible investigators (Dr. Nuria Fernández Monsalve, Dr. Luiz Monge and Dr. Maria de Carmen Iglesias de la Cruz, who are certified to manage animals for scientific experimentation, Certificate category C) as well as by the veterinary staff of the facilities.The mice were inhaling isoflurane during during the *In vivo experiments* for avoiding any pain in case of undiserible side effects maybe present in the animals. Also, the sedation was necessary to keep the animals asleep since the experiment procedure required the animails to remain "motionless" (still breathing) for as long as

possible. The isoflurane doses rate was 5% in a methacrylate chamber to make the mice fall asleep and then kept at 2% as far the experiment ended. Some criterias were applied with stringency in order to reduce or avoid undiserible side effect conditions during the experiments such as weight loss, edema, pain and so on. The animails were sacrificed by the end of each investigation experiments through either painless methodologies cervical dislocation or by inhalation of CO_2.

2.8.1.1 Cell culture concerning In Vivo Early Tumor Detection by LTNh

In ***Chapter 3. Results and discussion Section 3.2*** results concerning ***Luminescence Transient nanothermometry (LTNh) technique*** shows the powerful tool of this technique for detection of tissues' abnormalities like a melanoma tumor. The procedures from the cells culture to the tumor induction are described as follows. The murine melanoma B16 is a spontaneously arising melanoma of C57Bl/6 mice, from which the B16 cell line was established. We have used this commercially available cell line (ATCC® CRL-6322™, Manassas, VA, USA) for the in vivo experiments. Cells were plated onto sterile T75 flasks (Thermo Fisher Scientific, Waltham, MA USA) and cultured with DMEM medium (Thermo Fished Scientific), supplemented with 10% fetal bovine serum and antibiotics (100 U/ml penicillin, 100 µg/ml streptomycin, all from Thermo Fisher Scientific), in a humidified incubator with 5%CO_2. After reaching 75-80% confluence, cells were trypsinized and centrifuged at 1000 g for 5 minutes

2.8.1.2 Animal studies concerning In Vivo Early Tumor Detection by LTNh

We used 6 to 12 week old female C57BL/6 mice to induce melanoma, a well-established and widely used tumor model. [1] Briefly, mice were anesthetized with isoflurane in 100% oxygen, placed in the prone position on the operating table and hair was removed with an electric shaver and hair removal cream to leave the back of the animal exposed for injection. With a 1-ml syringe with attached 27½-G needle, we inserted the needle superficially, so that it was visible through the skin. A subcutaneous injection of 100 µL containing a dose of 1×10^5 B16 cells (which is 1.5 to 2 times the minimal tumorigenic dose in normal C57BL/6 mice) resulted in a clear "bleb". A palpable tumor appeared in 10 to 11 days and was observed until it grew to an approximate size of 1 × 1 × 1–cm in 14 days. At this point, the tumors became necrotic in the top and began to ulcerate or bleed; and we euthanized the mice.

2.8.1.3 Animais studies concerning Subcutaneous NIR-II Fluorescence Imaging and Intranevously Injected Nanoparticles Biodistribution

For this study a total of 15 CD1 female mice (8-14 weeks old, weighing 25-39 g) bred at the animal facility of Universidad Autónoma de Madrid were used. In oder to track the biodistribution of the particles though the NIR-II fluorescence emission of Ag_2S Superdots synthesized in this thesis (see in ***Chapter 3. Results and discussion Section 3.3***) anesthesia was induced in the group of mice in an induction chamber with a continuous flow of 4% isoflurane (Forane, AbbVie Spain, S.L.U) in 100% oxygen until loss of righting reflex was confirmed and breathing rhythm was significantly slowed. Then, anesthesia was maintained by means of facemask inhalation of 1.5% isoflurane and core body temperature was kept at 36 ± 1 °C with a rectal probe and a controlled heating pad. Two different experimental procedures were used in anesthetized mice at the time of placing them into the small animal imaging chamber:

- In 4 mice, hair of the back was shaved with an electric shaver prior to subcutaneous injection of 100 µL of a PBS solution containing 1.5 mg/mL of Ag_2S superdots, Ag_2S dots, NPs:Nd-Yb or SWCNTs. One additional mouse was anesthetized in order to check the potential thermal load induced by laser with and without fur. To that, an infrared thermographic camera (FLIR E-40) was used to measure surface temperature with 14 different irradiation power density: 0.3, 5, 20, 40, 50, 70, 90, 112, 130, 150, 173, 200, 227 and 240 mW/cm^2 and the illuminating time was settled as 1 min in the intact mouse and 30 s after shaving the fur. As shown in the figure, accumulative surface temperature reached 2°C when the power density was 150 mW/cm^2.

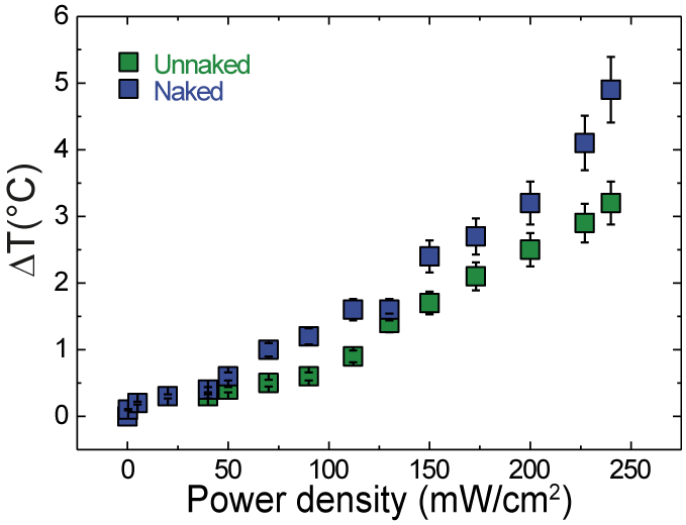

Figure 2.8 Temperature increment after illuminate whole-body of an individual mouse with an 810 nm fiber-coupled laser at different power densities. The experiment was made in a mouse before and after shaving its fur.

- In 2 mice, a small incision in the neck skin was done to expose the right jugular vein, and a polyethylene tubing catheter was inserted 2 mm in the caudal direction to infuse 100 μL of solution containing 1.5 mg/mL PEG-coated Ag_2S superdots dispersed in PBS. Three hours after infusion, mice were sacrificed by isoflurane overdose and major organs (liver, spleen, heart and lungs) were collected to obtain *ex-vivo* NIR-II images.

2.8.1.4 In vivo toxicity study concerning Intranevously Injected Nanoparticles Biodistribution

For the *in vivo* toxicity study, 4 mice were intraperitoneally injected with 300 μL of a 500 μg/mL solution of Ag2S superdots in PBS. A control group of 4 additional mice were intraperitoneally injected with 300 μL of PBS. The animals were housed in two separated cages in a room (23 ± 2°C) maintained on a 12/12 h light/dark cycle (light on at 6:30 am) with food and water continuously available. Weight increase, food ingestion and surface temperature measured by an infrared thermographic camera (FLIR E-40), were analyzed in the awake mice on a daily basis during 2 weeks.

3 Results and discussion section

3.1 Ag_2S nanodots for Lifetime-Based Luminescence Thermometry in the Near Infrared Second Biological Window (NIR-II BW)

To sum up briefly, the main purpose of our study in this section is to provide a methodological description of the potential of Ag_2S nanodots for ***Lifetime-Based Luminescence Nanothermometry (LT-LNTh*)**. The results demonstrated that Ag_2S nanodots present a unique design, showing to be a special material for lifetime nanothermometry operating in the NIR-II biological window (1000-1400 nm). Indeed, in this present section, the time-resolved fluorescence of our presented Ag_2S was investigated by looking at its main emission, which is found to be around 1225 nm, and has showed to be strongly temperature dependent. This is certainly a pivotal requirement for a material that would exhibit potential applicability regarding lifetime based luminescence nanothermometry. Although many examples of materials for LNTh have been reported to present a high lifetime thermal sensitivity, the majority is found to show up limitations by working in the visible range (450-750) [29]. Indeed, the Ag_2S nanodot is the best one for *In Vivo* LT-LNThs purposes, since it is the only one operating in the second biological window and, thus, the only one LT-LNThs potentially capable of subtissue lifetime based thermal sensing. Additionally, the roles of surface coating (PEG-SH -Ag_2S or DDT- Ag_2S) of the nanodots as well as the surrounding medium in which they were dispersed (water and toluene, respectively) were deeply investigated in this specific part of the thesis (an illustrative description are displayed in **Fig. 3.1**). Beyond, we have designed and conducted a methodological experiment showing a direct application with the final objective of determining the magnitude of the differences between inner and surface temperatures of a tissue undergoing localized heating. This opens up questions of great relevance especially when dealing with photothermal therapies of subcutaneous tumors. In these cases detailed knowledge of the relation between skin and inner tumor's temperature is essential in order to understand heat dissipation in treated tumors as well as to achieve

easy control over therapy by simple surface (skin) thermal measurements. The studies being reported here were recognized due to the remarkable achievements required in nanomedicine issues and the investigations were published in Nanoscale Journal, which is known by its high credibility and impact factor [25].

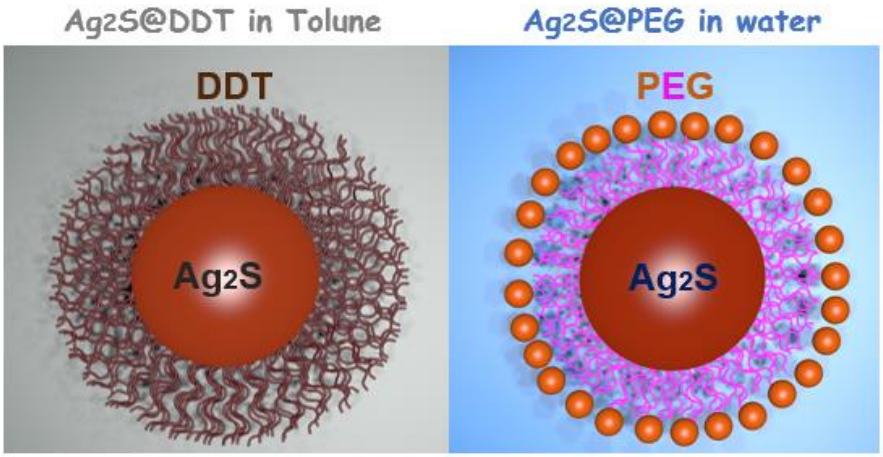

Figure 3.1 Illustrative description of Ag_2S nanodots coated with hydrophobic DDT ligands and PEG-SH dispersible in toluene and water solvents, respectively.

3.1.1 Analysis of room temperature decay curves: Decay rates and quantum confinement of Ag_2S nanodots.

Fig. 3.2a and **b** shows the TEM images corresponding to Ag_2S nanodots coated with PEG-SH and DDT ligands that make then dispersible in nonpolar and polar solvents, respectively. The size histograms obtained in each case are shown in **Fig. 3.2c** and **Fig. 3.2d**, respectively. Average sizes were found to be 4.7±0.7 and 4.3±0.7 nm for the Ag_2S nanodots coated with PEG-SH and DDT ligands, respectively. The size difference observed can be due to the presence of some unreacted precursor or to the encapsulation on the nanodots` surface by the big PEG-SH molecules that could interact with the DDT existing ligands instead of being completely removed, thus slightly increasing their size. The observed size change due to ligand exchange (0.4 nm) is, nevertheless, within the uncertainty in size determination so that it can be considered as negligible. In both cases TEM images reveal spherical Ag_2S nanodots that showed excellent colloidal properties without signs of precipitation during months (**Fig. 3.2e**). Under 808 nm excitation, colloidal solutions showed a bright infrared luminescence centered at 1225 nm (see **Fig. 3.2f**).

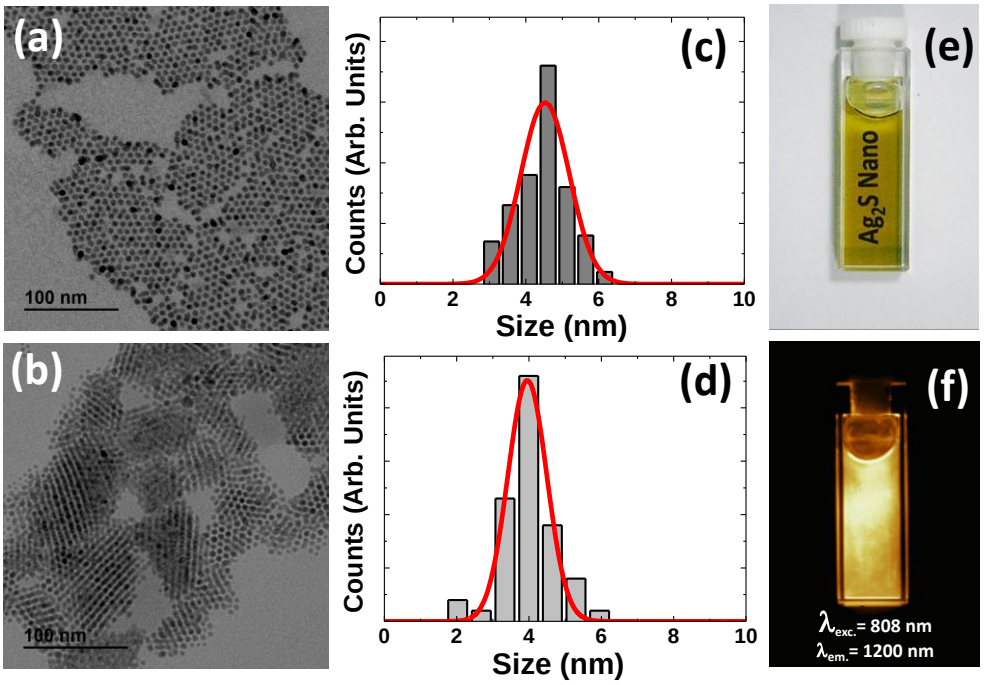

Figure 3.2 TEM images of Ag_2S nanodots coated with PEG-SH (**(a)**) and DDT (**(b)**) ligands that make them colloidal in water and toluene, respectively. The size histograms obtained in each case are shown in **(c)** and **(d)** for PEG-SH and DDT coatings, respectively. (bars are experimental data and solid line is the best fit to a Gaussian distribution). **(e)** Optical photograph of a colloidal solution of Ag_2S nanodots in water. **(f)** Fluorescence image of the solution included in **(e).** Excitation and emission wavelengths were set to 808 and 1200 nm, respectively.

Despite similar emission spectrum profile can be found for both colloidal solutions of Ag_2S nanodots (water and toluene), their room their room temperature fluorescence decay curves are remarkably different (**Fig. 3.3a**). Indeed, DDT coated Ag_2S nanodots dispersed in toluene showed a single exponential decay (it can be seen with more detailed in the adjustment present in **Fig. 3.4**). This, according to previous works, may suggest that in this case, surface related nonradiative de-excitations (via surface defects or environment assisted multiphonon relaxations) are not taking place.[30] Thus, the observed single exponential decay obtained for DDT coated Ag_2S nanodots dispersed in toluene would reveal the single contribution in respect to "bulk" process. Under this assumption we can state that the room temperature "intrinsic" bulk fluorescence lifetime of DDT coated Ag_2S nanodots is close to 180 ns, i.e. $\tau_B^{DDT}(RT) \approx$ 180 ns. The total (radiative plus nonradiative) bulk room temperature decay probability of DDT coated Ag_2S Nanodots is, therefore, calculated to be $W_B^{DDT}(RT) = \left(\tau_B^{DDT}(RT)\right)^{-1} \approx 5.5 \times 10^6$ s^{-1}.

At variance, PEG-SH coated Ag_2S nanodots dispersed in water showed an evident nonexponential decay. In this case, the fluorescence decay curve can be nicely fitted to a double exponential decay curve, an approach widely assumed by authors in previous studies dealing with fluorescence dynamics of semiconductor nanostructures.[31] The experimentally obtained decay curves of our Ag_2S nanocrystals suspended in water have been fitted to:

$$I_{em}^{PEG}(t) = A_B exp(-t/\tau_B^{PEG}) + A_S exp(-t/\tau_S^{PEG}) \quad (3.1.1)$$

where A_B and A_S are the amplitude components of slow and fast decay components, respectively. In expression (1) τ_B^{PEG} and τ_S^{PEG} are the fluorescence lifetimes of the slow and fast decay components, respectively. Fitting the decay curve, at room temperature, we experimentally obtain both fast and slow decay times τ_S^{PEG}= 17 ns and $\tau_B^{PEG} = 140$ ns, respectively (see fits included in **Fig. 3.4**). The fast and slow lifetime values are found to be significantly larger than those reported by W.J. Mir et al. (1 and 11 ns) but comparable to the values found by P. Jiang and co-workers (10 and 75 ns).[32] According to previous works, the fast decay component can be attributed to surface nonradiative de-excitations due to the presence of defect states, surface inhomogeneities (both created during the ligand exchange process), and/or to a strong coupling with the environment phonons (vibrations of water or PEG-SH surface molecules).[33] At the same time, the long fluorescence lifetime component can be correlated to bulk excitonic recombinations. Thus, we can define, for PEG-SH coated Ag_2S nanodots dispersed in water, two characteristic decay times at room temperature namely the bulk and surface decay times ($\tau_B^{PEG}(RT) \cong 140$ ns and $\tau_S^{PEG}(RT) \cong 17$ ns, respectively). The total bulk radiative probability of PEG-SH coated Ag_2S nanodots can be estimated to be $W_B^{PEG}(RT) = \left(\tau_B^{PEG}(RT)\right)^{-1} = 7 \times 10^6 s^{-1}$. The fact that $W_B^{PEG}(RT) \cong W_B^{DDT}(RT)$ evidences that the ligand exchange process did not affect the bulk recombination dynamics. Therefore, the differences between fluorescence dynamics of Ag_2S nanodots in toluene and water can be attributed to surface-related processes. At this point, it is important to note that the assignment of the long lifetime (≈ 140 ns) component to the inverse of the bulk total de-excitation probability in both PEG and DDT coated Ag_2S nanodots is in agreement with previous works. Y. Zhang and co-workers investigated the fluorescence time decay characteristics of colloidal Ag_2S nanodots in chloroform with variable sizes ranging from 2.2 up to 7 nm and concluded

that, as size was increased, the fluorescence decay curve was dominated by a long component with a characteristic decay time of 180 ns that was also attributed to pure bulk electron-hole recombinations [17b].

Fig. 3.3b shows the wavelength dependence of the room temperature fluorescence lifetime of our Ag_2S nanodots in toluene and water (circles and squares, respectively). For comparison, the room temperature emission spectrum is also included (red line). In the case of Ag_2S nanodots in water the averaged lifetime is defined as $\bar{\tau} = \frac{\int I(t)\cdot t\cdot dt}{\int I(t)\cdot dt}$, where $I(t)$ is the emitted intensity at time t after excitation. As can be observed, the fluorescence lifetime remains, within the experimental uncertainty, wavelength independent. When dealing with semiconductor nanostructures, the combination of inhomogeneous broadening (size dispersion) and quantum confinement (size) leads to wavelength dependent fluorescence decay times.[34] Therefore, the experimental evidence of a wavelength independent fluorescence lifetime in our Ag_2S nanodots suggests the absence of quantum confinement. This was, somehow, expected since the size of our Ag_2S nanodots (4-5 nm) is significantly larger that their Bohr radius. This has been experimentally estimated by Y. Zhang and co-workers to be 2 nm and theoretically calculated by S.Lin *et al.* to be as low as 1 nm.[17b, 35] The absence of quantum confinement in Ag_2S Nanodots is also in agreement with the work published by V. M. Huxter *at al*. who demonstrated that 8 nm Ag_2S nanocrystals exhibit optical absorption spectra similar to the corresponding bulk materials [36].

At this point it should be noted that is also possible to find in literature different works reporting on strongly wavelength dependent fluorescence lifetimes for Ag_2S nanodots. For instance, W.J. Mir *et al.* reported on a relevant increment of fluorescence lifetime with the emission wavelength being this associated to a relevant contribution of emitting defects at short wavelengths.[32a] Nevertheless, this behavior was claimed by authors as unusual and, in our opinion, reflects the relevant role that surface properties, strongly dependent on particular synthesis procedure, plays in the fluorescence dynamics of Ag_2S nanodots. The determinant role of surface on luminescence properties of Ag_2S nanodots has been also recently evidenced by R. Gui et al. who demonstrated that slight variations on the surface decoration could lead to large variations in the fluorescence Quantum Yields.[37] The strong relation between luminescence properties of Ag_2S nanodots and capping agents at their surface was also stated by M.C. Brelle and

co-workers. They claimed the existence of "deep traps" in Ag_2S nanodots whose relaxation dynamics after laser excitation were strongly dependent on capping materials.[38].

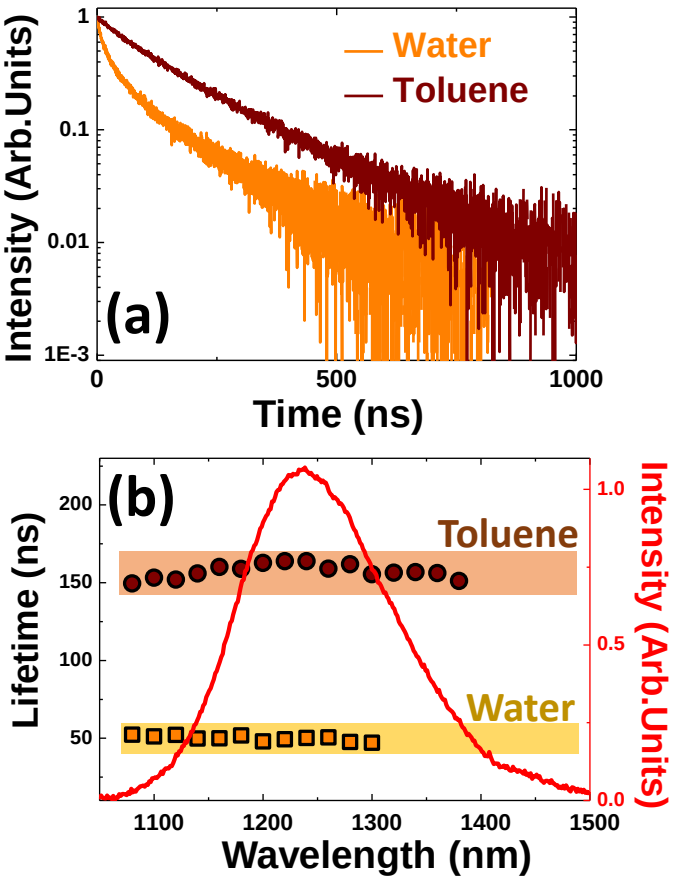

Figure 3.3 (a) Room temperature luminescence decay curves of Ag_2S nanodots in toluene and water. **(b)** Wavelength dependence of the luminescence lifetime of Ag_2S nanodots in toluene and water. Symbols are experimental data and color rectangles are just guide for the eyes to evidence the wavelength independent value of lifetime. The room temperature emission spectrum of Ag_2S nanodots is also included (solid red line).

3.1.2 *Temperature dependence of decay curves.*

Additionally to the exponential and non-exponential behavior found in the fluorescence decay curves of DDT and PEG-SH coated Ag_2S nanodots, respectively, **Fig. 3.4** provides information about their fluorescence decay curves as obtained at two different temperatures (22 and 48 °C). Their fluorescence decay curves were found to be, in both cases, strongly temperature dependent. Indeed, a relative small temperature increment of 30 ºC has led to a relevant (70%) shortening of the decay times. In the case of Ag_2S nanodots dispersed in toluene, the temperature induced reduction takes place

while keeping the single exponential character. Thus, following the same arguments described in the previous section, this temperature induced lifetime reduction can be correlated to non-radiative recombinations assisted by multiphonons. **Fig. 3.4** also reveals that for DDT coated colloidal Ag_2S nanodots dispersed in toluene, temperature increments in the biological range (20-50 °C) does not lead to the activation of electronic de-excitations via neither surface effects nor phononic coupling with molecules in contact with surface of nanodots. The temperature dependence of the bulk fluorescence decay time of DDT coated Ag_2S nanodots in toluene ($\tau_B^{DDT}(T)$) is included in **Fig. 3.5a** from which a remarkable temperature induced reduction is observed: from 180 down to 60 ns when the temperature is increased from 20 up to 50 °C. At variance with other semiconductor nanosystems (such as CdTe QDs) the temperature induced reduction in the fluorescence lifetime does not follow a linear trend [29c]. This, as it will be demonstrated in the next section, leads to temperature independent thermal sensitivities in the surroundings of room temperature.

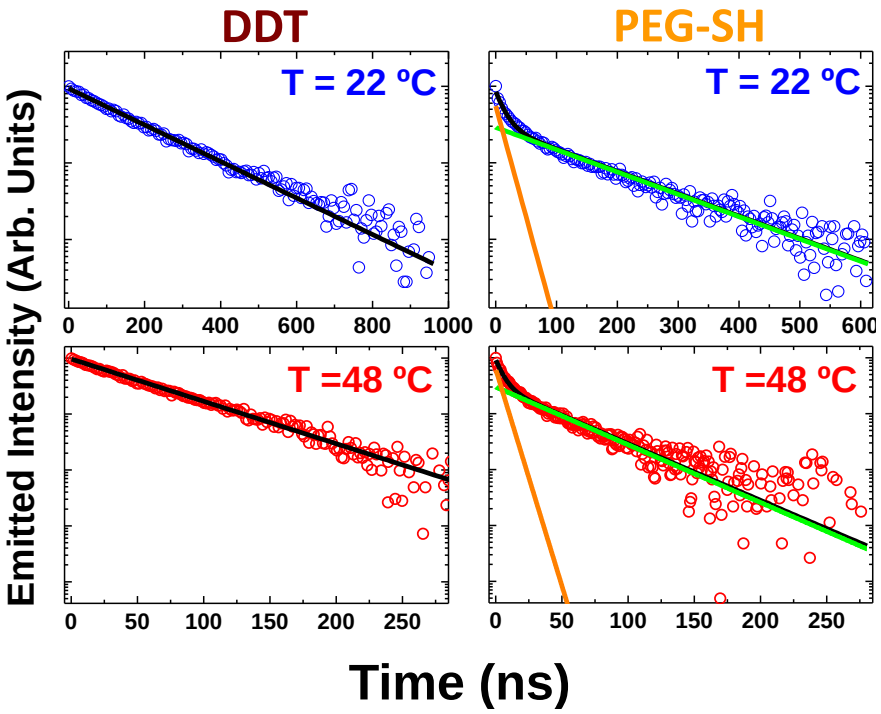

Figure 3.4.- Luminescence decay curves at 22 and 48°C as obtained for colloidal solutions of DDT and PEG-SH coated Ag_2S nanocrystals dispersed in toluene and water, respectively.

Fluorescence decay curves from PEG-SH coated Ag_2S nanodots were found to present, not only at room temperature as previous described, but at any temperature a double exponential decay behavior (see **Fig. 3.4**). By fitting to a double exponential on the decay profiles obtained at different temperatures, it is possible to access the

temperature dependence of both bulk and surface fluorescence decay times ($\tau_B^{PEG}(T)$ and $\tau_S^{PEG}(T)$, respectively). Results are included in **Fig. 3.5a**. Different conclusions can be extracted from these data. First, the bulk related fluorescence decay time strongly reduces with temperature, following almost the same trend as that obtained for DDT coated Ag_2S nanodots in toluene. This fact reinforces the assumption that in colloidal Ag_2S nanodots the long lifetime component can be associated with bulk electronic relaxations that, in turns, are strongly favored by multiphonon transitions activated by temperature. At the same time, experimental data included in **Fig. 3.5c** reveal a remarkable temperature induced reduction in the fluorescence lifetime due to non-radiative recombinations associated with surface defects (from 17 down to 6 ns when temperature is increased from 20 up to 50 °C). This can be associated with the thermal activation of multiphonon assisted recombination processes taking place at surface. We have also determined the temperature evolution of the probabilities constants related to bulk and surface transitions in respect to the net fluorescence of PEG coated Ag_2S nanodots (A_B and A_S amplitudes in expression (1), respectively). Results are included in **Fig. 3.5b** from which it is evident that the relative contributions of both processes can be considered, in a first order approximation, temperature independent, being the surface transitions dominant in the whole temperature range analyzed in this work. When the ratio A_B/A_S is calculated in detail, it is observed that temperature favors surface electronic recombinations as it is evidenced in **Fig. 3.5c**. Experimental data reveal a decrease in the relative contribution of bulk in respect to surface recombinations close to a 30% when temperature is increased from 20 up to 50 °C. This can be explained in terms of a temperature assisted energy migration from bulk to surface states, a mechanism already employed to explain the size dependence of quantum efficiency in visible emitting QDs [39].

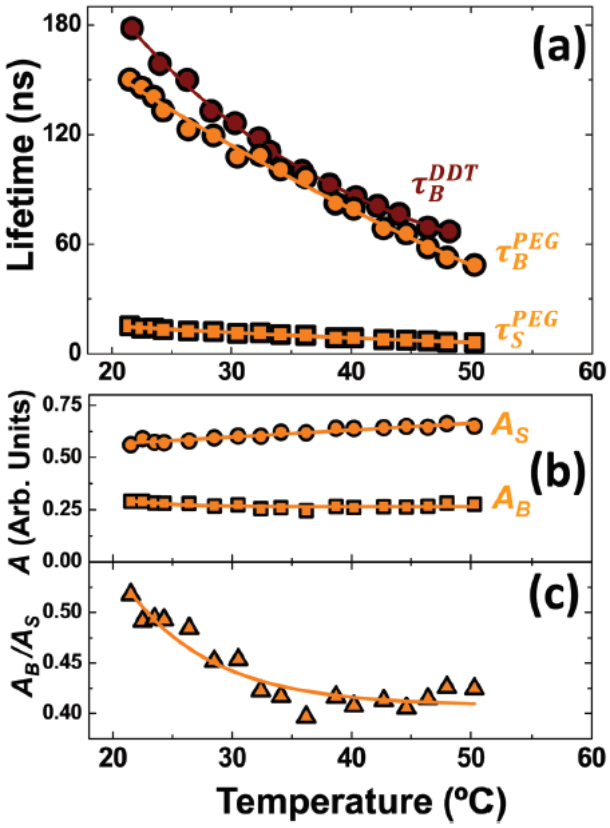

Figure 3.5 (a) Temperature dependence of the "bulk" fluorescence lifetime of Ag_2S nanocrystals in toluene (τ_B^{DDT}). The temperature dependences of both "bulk" and "surface" fluorescence lifetimes of Ag_2S nanocrystals in water are also indicated (τ_B^{PEG} and τ_S^{PEG}, respectively). Symbols are experimental data and solid lines are guide for the eyes. **(b)** Temperature dependence of the relative contribution of "bulk" and "surface" transitions to the net fluorescence decay curves of Ag_2S nanocrystals in water (A_B and A_S, respectively). Symbols are experimental data and solid lines are guide for the eyes. **(c)** Temperature dependence of the A_B/A_S ratio as calculated from data included in **(b)**. Symbols are experimental data and solid line is a guide for the eyes.

3.1.3 Temperature dependence of time-resolved fluorescence of Ag_2S nanodots

As mentioned in the beginning of this chapter one of the most interesting applications of fluorescence nanostructures with strongly temperature dependent fluorescence lifetime is their potential application for remote thermal sensing by lifetime based luminescence nanothermometry [40]. The ability of any given nanostructure for lifetime based luminescence nanothermometry depends on its particular relative thermal sensitivity, S_R, that is defined as [40b]:

$$S_R(T) = \frac{1}{\tau(T)}\frac{d\tau(T)}{dT} \quad (3.1.2)$$

where $\tau(T)$ is the fluorescence lifetime of the fluorescence nanostructure at temperature T and $\frac{d\tau(T)}{dT}$ is the temperature derivative of $\tau(T)$. In our case, $S_R(T)$ can be calculated from the experimental data included in **Fig 3.5a**. The thermal sensitivities obtained for both DDT and PEG-SH coated Ag_2S nanodots are included in **Fig. 3.6a**. It has been found that both DDT and PEG-SH coated Ag_2S nanodots provides very similar values of $S_R(T)$ in the whole temperature range here investigated. This is an outstanding point as it clearly evidences the robustness and reliability of thermal measurements performed on the basis of the analysis of Ag_2S nanodots the fluorescence lifetime, since their sensitivity does not critically depend on their surface properties. This would be a great advantage over other luminescence nanothermometers whose thermal sensitivity has been found strongly dependent on the environment and surface properties [40b, 41]. In addition, data included in **Fig. 3.6a** reveals that Ag_2S nanodots provide a lifetime based thermal sensitivity that depends only slightly on temperature in the 20-42 ºC range. In this temperature range Ag_2S nanodots provide a lifetime thermal sensitivity as large as 3-4 %·ºC^{-1} that is above most of the lifetime thermal sensitivities previously reported in the literature (see the comparative graph included as **Fig. 3.6b**). Only polymeric nanostructures have provided a larger lifetime thermal sensitivities but with the drawbacks of a much reduced temperature operation range (30-36 ºC) [29a, 29b] while we report are reporting here 20-50 ºC with our Ag_2S nanodots.

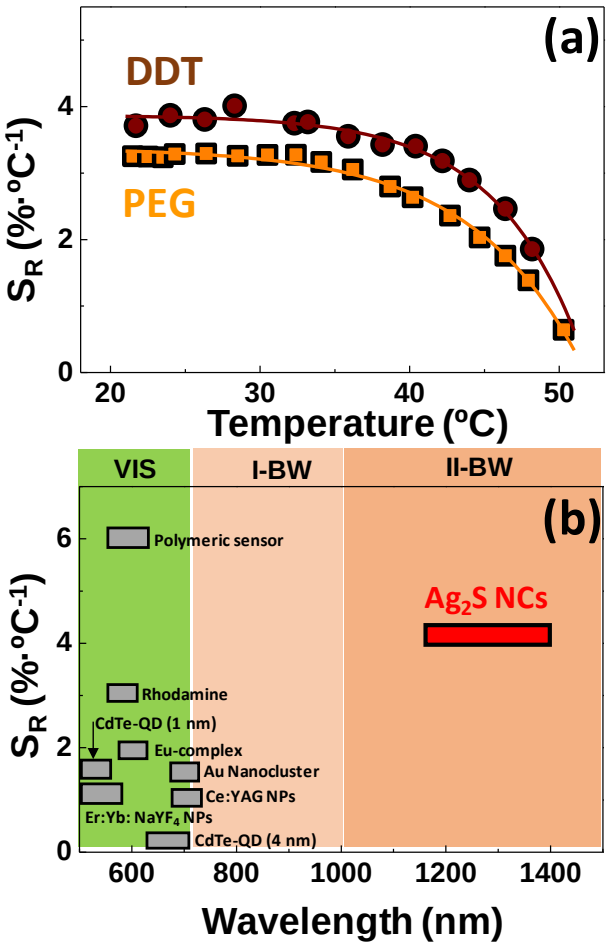

Figure 3.6 (a) Temperature dependence of the relative lifetime based thermal sensitivity of both DDT and PEG coated Ag_2S nanocrystals. Symbols are the experimental data obtained from the analysis of data included in Figure 4(c) and solid lines are guide for the eyes. **(b)** Lifetime based thermal sensitivity of different luminescent nanothermometers and their spectral operating ranges.[29]

The clear advantage of Ag_2S Nanodots over the already developed LT-LNThs is their spectral operating range. From **Fig. 3.6b** it is clear that Ag_2S nanodots are the only LT-LNThs that operates in the second biological window and, thus, they are the only one LT-LNThs potentially capable of subtissue lifetime based thermal sensing. In order to provide a proof of concept of the potential application of our ag_2S Nanodots for subtissue lifetime based thermal sensing, a simple experiment was designed (see schematic representation of **Fig 3.7a**). These experiments were designed and conducted with the final objective of determining the magnitude of the differences between inner and surface temperatures of a tissue undergoing localized heating. This is an open question of great relevance especially when dealing with photothermal therapies of subcutaneous tumors. In these cases detailed knowledge of the relation between skin and inner tumor's temperature is essential in order to understand heat dissipation in

treated tumors as well as to achieve easy control over therapy by simple surface (skin) thermal measurements [42]. As it is schematically indicated in **Fig. 3.7a**, in our case the point heating source is constituted by a high resistive Kanthal wire (0.2 mm radius) that is placed under a chicken breast tissue. This wire was connected to a voltage supply in order to control the magnitude of heating. The surface temperature of the tissue was measured by using an infrared thermal camera (FLIR E40 bx as described in ***Surface temperature distribution feedback by Infrared thermography Section***). In order to simultaneously detect the subtissue temperature (T_{st}, that is the temperature of the resistive wire) a thin film of Ag_2S nanodots was placed between the heating wire and the tissue. This thin film provides the same thermal sensitivity of Ag_2S nanodots dispersed in either water or toluene. Optical excitation of the sensing film was provided by an 80 ps 405 nm pulse diode laser.

The time decay curve of the Ag_2S nanodots in the film was obtained by using the same experimental set-up ***system (a)*** described in ***Lifetime Spectroscopy Section***. **Fig. 3.7b** and **c** shows the optical images of the system constituted by the heating wire and sensing film with and without a 3 mm thick tissue. **Fig 3.7d** includes the infrared thermal images obtained when tissues holding different thickness equal to 1, 3 and 5 mm was placed on top of the heating wire (images were obtained when an electrical current of 0.6 A was established). From these thermal images we have extracted the maximum surface temperature (T_{sf}) for the different tissue thickness. It is worthy to give the mathematical description of the thermal impedance in this particular case, because the although the intrinsic tissues properties are keep the same (since them all are chicken tissue), the thermal impedance, that is, the temperature gradient per unit of heat flux, passing through the interface is dependent upon the dimensions of the tissue, in this case the thickness. The thermal impedance is constructed by combining the definitions of thermal resistance and capacity, and it is mathematically described by:

$$\beta_{th} = R_{th} \cdot A = \frac{A}{C_{th}} = \frac{\Delta T \cdot A}{q} = \frac{A}{mc} \tag{3.1.3}$$

Where R_{th} and C_{th} is the thermal resistance and capacity, respectively. $\Delta T = T_{st} - T_{sf}$ is the temperature difference between the surfaces at bottom and top of a chicken tissue, in which the bottom is defined to be the one at the interface-contact area to the heat sink (our Kanthal wire), settle to be in a steady temperature T_{st}. The top is the opposite interface in a distance to the bottom equal to the tissue's thickness in which its

temperature is to be T_{sf}. A is the area limited by the transversal dimensions of the tissue, m is the mass and c is the specific heat. Note that q is the total charge provided by the heat dissipation of the Kanthal wire after applying a fixed electrical current of 0.6 A, therefore, this value is the same used for all tissues` thickness. The only parameter that change is the mass due to the increment of thickness, therefore, ΔT is expected to increase when the thermal impedance increases (when the mass increases). As can be observed in **Fig. 3.7e** T_{sf} decreases monotonously with the tissue thickness as it was, indeed expected due to the increment in the thermal impedance. For each particular tissue thickness the subtissue temperature (wire's temperature) was obtained by analyzing the fluorescence decay curves of the Ag_2S nanodots thin film. The variation of this subtissue temperature (T_{st}) with the tissue thickness are also included in **Fig. 3.7e**. At variance with the surface temperature, T_{st} has been found to be almost independent on the tissue thickness. **Fig. 3.7g** shows the relative difference between subtissue and surface temperature as expected ($\Delta T_R = \left(T_{st} - T_{sf}\right)/\Delta T_{st}$, were ΔT_{st} is the absolute increment in the subtissue temperature) as a function of tissue thickness as calculated from data included in **Fig. 3.7e**. Note that ΔT_R becomes larger as the tissue thickness is increased. Indeed, for a tissue thickness of 5 mm, we have found $\Delta T_R \approx 80$ %, so that for such thickness the "apparent" surface temperature increment is only 20% of the actual subtissue temperature increment. This evidences the critical importance of achieving subtissue thermal reading in bio-applications where surface measurements (achieved by using infrared thermal cameras) could lead to a totally wrong and drastic underestimation of actual inner temperature. The existence of large differences between subtissue and surface temperatures has been previously evidenced in *in vivo* experiments. For instance, during photothermal therapies of cancer tumors these temperature differences have been reported to be as large as 57%, 40%, and 20% for thermal therapies based on carbon coated nanoparticles, quantum dots and rare earth doped nanoparticles, respectively. [1c, 42-43] Thus, *in vivo* experimental data reveals, on average, a discrepancy between surface and intratumoral temperatures close to 40% for a subtissue depth close to 2 mm (being this the average tumor radius used in animal models). This is, indeed, in good accordance with the experimental data included in **Fig. 3.7e** that predicts, for this thickness, a relative temperature difference of 50%. In order to provide additional information and a further support to our experimental measurements we have conducted numerical simulations of the temperature patterns

created in the tissue by the heating wire. **Fig. 3.7f** includes two characteristic thermal patterns calculated by assuming a tissue thickness of 0.5 and 5 mm, respectively. From these simulations the existence of relevant temperature differences between surface and heating source (wire, in our case) are evidenced, these being increased with the tissue thickness. By performing simulations with different tissue thickness we were able to compute the dependence of ΔT_R with the tissue thickness. Results obtained from numerical simulations are included as solid line in **Fig. 3.7g** from which an excellent agreement between experimental data and simulations that demonstrates the suitability of Ag_2S nanodots for subtissue lifetime thermal sensing. Furthermore, temperature induced lifetime reduction is accompanied by a remarkable intensity reduction as well by a substantial change is spectra shape, this makes Ag_2S nanodots very promising candidates for fast and high precision multiparameter temperature sensing via neuron network reconstruction, a possibility that has been already demonstrated based on other semiconductor nanodots [44].

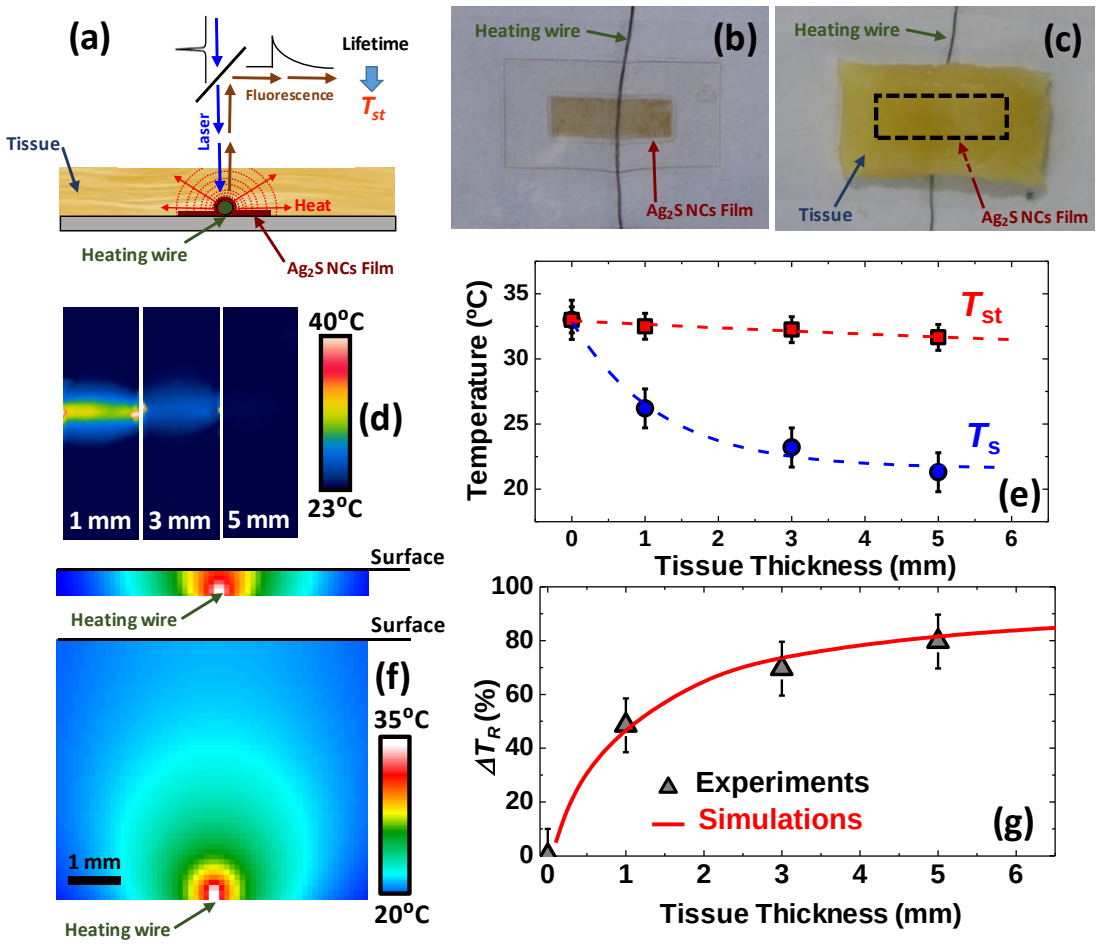

Figure 3.7 (a) Schematic representation of the *ex vivo* experiments designed and conducted to demonstrate the ability of Ag_2S NCs for lifetime based subtissue thermal sensing. **(b)** Optical image of the

thin film of Ag_2S NCs used for subtissue lifetime thermal sensing. The heating wire is also shown. **(c)** Optical picture of the thin film and wire under a 3 mm thick tissue. **(d)** Infrared thermal images (surface thermal images) as obtained for three tissue thicknesses. Wire's current was set to 0.6 A. **(e)** Dependence of both surface and subtissue temperatures on tissue thickness. Symbols are experimental data and dashed lines are guides for the eyes. **(f)** Numerical simulations of the cross sectional temperature patterns as obtained by assuming tissue thickness of 0.5 and 5 mm. **(g)** Relative temperature difference between surface and subtissue temperature increments as a function of the tissue thickness. Symbols are data obtained from experimental measurements included in **(e)** whereas solid line is obtained from numerical simulations.

Finally, we should note that the use of a pulsed laser sources with longer wavelengths instead of a 450 nm laser here used would result in an improved penetration depth. For instance, subtissue penetration length of 808 nm excited Ag_2S have been found to be more than two times larger than those here reported under 450 nm laser excitation. Nevertheless, the use of the 450 nm laser (lying out of the biological windows) does not subtract validity to the main conclusion of this work that is the great potential of Ag_2S Nanodots for lifetime based thermometry.

3.2 Ag_2S nanodots for Tumor Detection Based-Luminescence Transient Nanothermometry (LTNh)

Nanotechnologies have demonstrated tendencies towards the implement and development of new techniques for diagnostic and therapeutic applications well-defined as theranostics. In the previous section we have shown the potential application of our Ag_2S for nanothermometry, more specifically that one based on lifetime parameter, so called *Lifetime-Based Luminescence Nanothermometry (LT-LNTh***)**. In this section we are going to report a long-desired dream of accessing, with an extremely high accurate level, the state of tissues abnormalities, providing early diagnosis for more effective treatments with a higher cure rate. To do so, the nanothermometry-based approach using the Ag_2S nanodots was again implemented. Instead of using *(LT-LNTh***)** the temperature induced changes in the overall number of emitted photons by Ag_2S nanodots were monitored. This latter technique (hereafter ***Intensity Luminescence Nanothermometry (ILNth)***) together with *(LT-LNTh***)** belongs to a general group called ***Luminescence Thermometry*** [40a]. Once more, the Ag_2S nanodots show off their orienteering skills, working in a new challenging task of leading an effective and efficient accurate intratumoral thermal reading opens up access to assessment for identifying malfunction through tissue properties and its surrounds promoted by the presence of a tumor. Herein, we report a novel and outstanding pathway for premature tumor detection. The high thermal sensitivity of luminescence intensity from Ag_2S nanocrystals was capable of monitoring the temperature dynamics (time evolution of temperature) of tissue during and after being subjected to a thermal stimulus. The changes on the tissue properties enabled the efficient detection of growth of a tumor and beyond, predicting its stage and degree, which in turns can be denoted in two regimes - angiogenesis and necrosis-, where the latter is prognosticated to be in high level as the tumor presents an advanced stage.

3.2.1 Fundamentals of Living Tissue Diagnosis by Thermal Transient Thermometry

From a thermodynamic standpoint, a living tissue is a complex system whose temperature ($\boldsymbol{T_{ts}}$) is determined by the interplay between different physical parameters.

Both the tissue temperature and its thermal dynamics depend both on intrinsic tissue properties (such as its mass, specific heat and thermal conductivity) and on physiological parameters of the organism. The latter include blood temperature and perfusion rate, together with the overall metabolic activity. All these variables influence the response of living tissues to thermal stimuli, which can be expressed through the well-known Pennes' bioheat equation. Transient thermometry (hereafter TTh) aims to obtain information about the state of living tissues by monitoring their thermal relaxation dynamics after application of a moderate heating stimulus that drives the tissue temperature slightly above ($\Delta T < 7^{\circ}C$) its basal value. The tissue thermal relaxation that happens once the heating stimulus is removed, according to Pennes´ formalism, can be written as follows: [45]

$$\rho_t c_t \frac{dT_s(\vec{r},t)}{dt} = -k\nabla^2 T_s(\vec{r},t) - \omega_b \rho_b c_b \left(T_s(\vec{r},t) - T_b(\vec{r})\right) + Q_{met} \qquad (3.2.1)$$

where $\boldsymbol{\rho_t}$, $\boldsymbol{k}$ and $\boldsymbol{c_t}$ are mass density, thermal conductivity and specific heat of the living tissue and $\boldsymbol{\omega_b}$, $\boldsymbol{\rho_b}$, $\boldsymbol{c_b}$ and $\boldsymbol{T_b}$ are the perfusion rate, mass density, specific heat and temperature of the blood. In expression (1), $\boldsymbol{Q_{met}}$ refers to the heat production caused by the tissue metabolic activity. In a first order approximation, as described in detail in the Supporting Information, equation (1) can be solved leading to:

$$\Delta T_s(t) = \Delta T_s(t=0) e^{-t/\tau_c} \qquad (3.2.2)$$

where $\Delta\boldsymbol{T_s}$ refers to the difference between the tissue temperature at time *t* after removing the heating stimulus and its basal temperature. Accordingly, $\Delta\boldsymbol{T_s}(\boldsymbol{t=0})$ is the temperature increment caused by the heating procedure. In expression (2), $\boldsymbol{\tau_c}$ is the tissue characteristic cooling time, which can be written in a first order approximation as:

$$\tau_c = \frac{\rho_t c_t}{\omega_b \rho_b c_b + Ck - \alpha} \qquad (3.2.3)$$

where $\boldsymbol{C}$ is a time-independent constant that depends on the dimensions of both the tissue and the heating source and $\boldsymbol{\alpha}$ is associated with the metabolic activity (see equation S19 for more details). From expression (3), it is clear that the cooling dynamics of a tissue strongly depends on its intrinsic characteristics (density, thermal conductivity and specific heat), while also being influenced by the thermoregulation mechanisms provided by the cardiovascular system through the blood flow rate. Therefore, the analysis of the cooling dynamics of living tissues can constitute a

powerful tool for the diagnosis of any disease that affects either the intrinsic tissue properties or its blood perfusion rate.[46] Tumor evolution can affect all the variables included in expression (3). Indeed, it has already been reported that tumor growth promotes alterations in the tissue specific heat, thermal conductivity and density.[47] Additionally, the interplay between angiogenesis and necrosis during tumor evolution leads to changes in the blood perfusion rate at the core of the tumor and its periphery.[48] According to expression (3), those changes in the blood flow could also lead to remarkable changes in the tissue thermal relaxation dynamics. Therefore, relevant information about tumor development could be obtained through in vivo measurement of the thermal relaxation dynamics and its subsequent analysis based on expression (3), which is the basis of TTh.

3.2.2 Early Tumor Detection by Nanoparticle-Assisted Transient Thermometry

As stated in the previous sections, TTh requires an accurate measurement of the tissue thermal relaxation after subjecting it to a moderate heating. In this work, we studied the evolution of the thermal dynamics in a murine model of melanoma throughout its growth since induction in C75Bl/6 mice until its final stages, when necrosis was evident. Details about the procedure followed for tumor induction can be found in the Supporting Information. For monitoring the tissue temperature, we relied on NIR nanothermometry provided by intratumorally injected Ag_2S nanocrystals. These nanocrystals presented an average diameter of 4.2 nm, as measured from TEM images as shown in **Fig. 3.8a**, and remarkable temperature sensitivity in NIR-II. This is evidenced in **Fig. 3.8b**, where the emission spectrum of a colloidal suspension of Ag_2S nanocrystals in phosphate buffer saline (PBS) is given for different temperatures. From the data in Figure 1(b), we determined that the Ag_2S nanocrystals showed an intensity-based thermal sensitivity of $3\%\cdot{}^{\circ}C^{-1}$, in good agreement with recently published results.[49] The thermal calibration curves obtained for Ag_2S nanocrystals in aqueous dispersion and in a tumor tissue sample (see Figure S1) showed no effects of the environment in their thermal sensitivity, highlighting the reliability of these NPs as temperature sensors in biological media. To achieve intratumoral thermometry, Ag_2S nanocrystals were injected either together with the cancer cells used to induce tumor growth or at later stages of the tumor development. The moment at which the

nanothermometers were injected did not have an impact on the tumor thermal dynamics, as no effect related to the injection time was observed in the thermal relaxation curves.

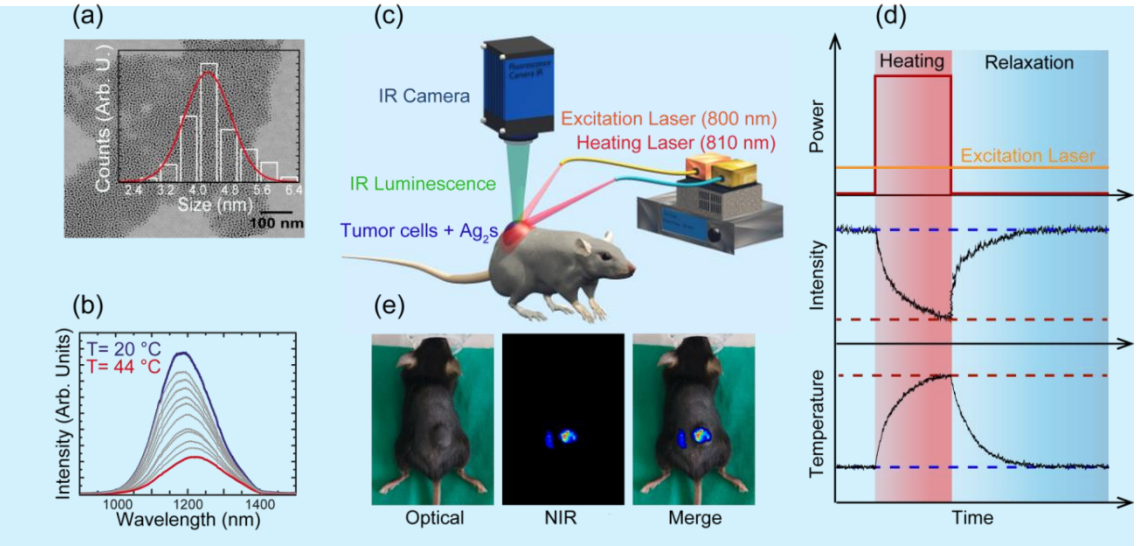

Figure 3.8 (a) Size histogram and representative TEM image of the Ag_2S nanothermometers used in this work. **(b)** Temperature dependence of the emission spectrum of Ag_2S nanothermometers upon optical excitation at 800 nm. **(c)** Schematic diagram of the experimental setup developed in this work for in vivo measurement of thermal transients in both tumoral and healthy tissues. The use of two infrared lasers (heating and pump radiations) is indicated, as well as the presence of Ag_2S nanothermometers. An InGaAs camera operating in the 1400-1700 nm range was used to collect the luminescence of Ag_2S nanocrystals. **(d)** Schematic representation of the experimental approach. A laser operating at moderate intensity (heating laser) was used to elicit a moderate local heating in a 4-minute-long time window. Thermal reading throughout the experiment was achieved by exciting Ag_2S nanocrystals with a laser operating at a much lower intensity (pump laser) so as not to generate any additional heating. The time evolution of the intensity emitted by the Ag_2S nanocrystals recorded by the InGaAs camera allows obtaining the temperature decay curve. **(e)** Optical and NIR fluorescence images of a representative mouse studied in this work. The NIR emission evidences the presence of Ag_2S nanocrystals both at the tumor site and in a healthy tissue area.

The experimental setup used to measure in vivo the thermal dynamics in tumor-bearing mice relied on a double-beam approach, as is schematically shown in **Fig 3.8 c**. An 810 nm fiber-coupled laser operating at a moderate intensity (0.25 $W \cdot cm^{-2}$), labeled as heating laser in **Fig 3.8c**, was used to elicit a moderate temperature increase (< 7˚C) at the tumor site. The major contributor to this laser-induced heating was the photothermal effect of the Ag_2S nanocrystals, as this wavelength does not cause significant tissue heating by itself. This laser was switched off after 4 minutes.

Meanwhile, the second laser (800 nm), operating at a much lower intensity (< 0.03 $W \cdot cm^{-2}$) achieved optical excitation of the Ag_2S nanocrystals without any measurable heating and was kept on throughout the experiment to monitor the intratumoral temperature. This is represented schematically in **Fig. 3.8d**, which shows how the low-power laser excitation does not affect the Ag_2S emission, whereas the heating laser causes a dramatic decrease in its intensity, which correlates with an increase in temperature. After the heating laser was switched off, the NIR-II emission generated by the intratumorally injected Ag_2S nanothermometers gradually recovered, indicating the thermal relaxation of the tissue until it reached its basal temperature. As a control, we measured the thermal relaxation profiles healthy tissue areas in the same mice, which were subjected to the same heating procedure as the tumor after subcutaneous injection with Ag_2S nanocrystals. The presence of Ag_2S in both tumoral and healthy tissues is shown, for one of the mice studied in this work, in the NIR-II fluorescence image in **Fig. 3.8e**. For both tumoral and healthy tissues, we obtained the thermal relaxation curves ($\Delta T_{tumor}(t)$ and $\Delta T_{health}(t)$, respectively) by combining the thermal calibration of the Ag_2S nanothermometers (see Figure S1) with the experimentally recorded intensity vs time curves. This allows us to compare the characteristing cooling times of both tissues, which, in a first approximation, are given by:

$$\tau_{tumor} = \frac{\int \Delta T_{tumor}(t)dt}{\Delta T_{tumor}(t=0)} \tag{3.2.4}$$

and

$$\tau_{health} = \frac{\int \Delta T_{health}(t)dt}{\Delta T_{health}(t=0)} \tag{3.2.5}$$

As shown in **Fig. 3.9a**, 24 hours after cancer cell inoculation (Day 1) the relaxation curves of healthy and tumoral tissues were almost identical, with tumoral tissue showing a slightly faster relaxation. If we define the relative change in the relaxation time as

$$\Delta\tau = \frac{\tau_{tumor} - \tau_{health}}{\tau_{health}} \tag{3.2.6}$$

we can state that 24 hours after innoculation $\boldsymbol{\Delta\tau}$ is slightly negative (close to -5%).

At the 5-day mark, the presence of tumors could not be observed by the naked eye (see optical images in **Fig. 3.9b**) nor by infrared thermography (**Fig. 3.9c**), which

typically reveals the presence of a tumor through a well-localized temperature singularity in the tumoral region. Although the tumor remained "invisible" for these two inspection techniques 5 days after tumor induction, that was not the case for the thermal relaxation profiles, which indicated remarkable differences between the thermal dynamics of tumoral and healthy tissues. At that point, the comparison between the thermal relaxation curves obtained for both tissues already led to values for $\Delta\tau$ above 15%. This difference in thermal relaxation profiles became even more pronounced as the tumor developed, as evidenced by the comparison between the thermal relaxation profiles obtained for both tumoral and healthy tissue 11 days after tumor inoculation (see last column in **Fig. 3.9a**). At this time, $\Delta\tau$ reached 45%. Such a large difference in thermal relaxation profiles occurs for a well-developed tumor, easily detectable by optical inspection and by infrared thermography (see last columns in **Fig. 3.9b** and **c**). Experimental data included in **Fig. 3.9** suggest $\boldsymbol{\Delta\tau}$ is a highly sensitive parameter for monitoring tumor progression, evidencing tumor development well before it becomes detectable by other techniques. This supports the use of TTh based on Ag_2S nanothermometersfor in vivo early tumor detection.

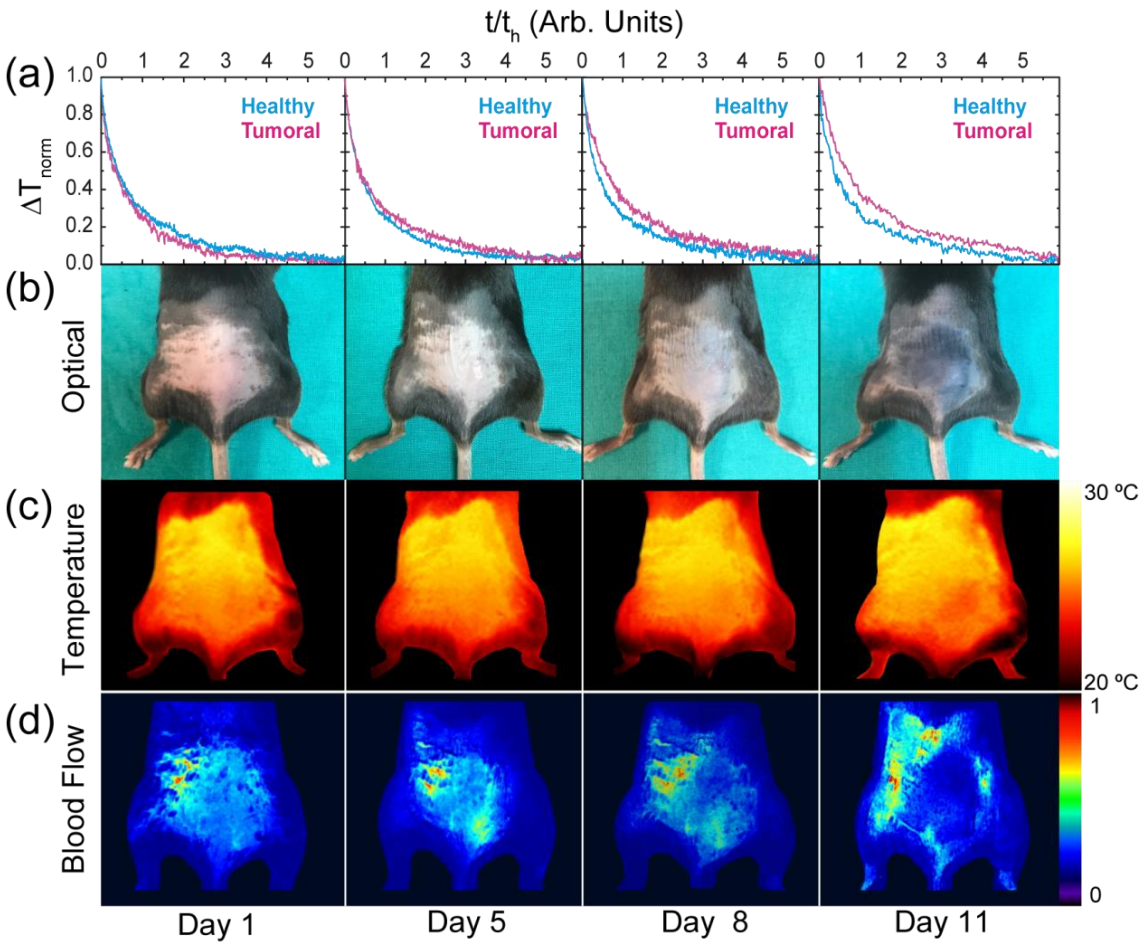

Figure 3.9 (a) Thermal transient curves corresponding to tumoral and healthy tissues as obtained at different times after inoculating a mouse with B16 cancer cells. **(b)** Optical images of a representative mouse at different time points after cancer cell inoculation. **(c)** Thermographic images and **(d)** blood perfusion images obtained with a laser speckle camera corresponding to the mouse shown in (b) at various time points after tumor induction.

The potential use of TTh as a tumor early diagnosis tool is further evidenced by the data included in **Fig. 3.10a**, which shows the time evolution (measured from the inoculation day) of $\Delta\tau$. For the sake of comparison, the time evolution of tumor size (**Fig. 3.10b**) and of the temperature difference between tumoral and healthy tissue, as measured by infrared thermography (**Fig. 3.10c**), are also included. All the data shown Figure 3 correspond to the average values from the experimental data obtained for the n = 6 mice studied in this work. From the variance on the experimental data obtained for different mice on the same day of tumor development, we estimated an statistical variation in $\Delta\boldsymbol{\tau}$ close to $\sigma(\Delta\boldsymbol{\tau})$ = ± 6%, assumed to be constant during tumor development. Then, we can establish the criterion that TTh would evidence the presence of a developing tumor when $\Delta\boldsymbol{\tau} > \sigma(\Delta\boldsymbol{\tau})$ (i.e. when the difference between the relaxation profiles of tumoral and healthy tissues is statistically significant). According

to this criterion, the experimental results shown in Figure 3(a) evidence that TTh can detect the existence of a tumor only 5 days after the inoculation of cancer cells. This constitutes a great advance when compared with the traditional detection based on optical inspection, which cannot achieve tumor detection until seven days later, i.e. eleven days after inoculation with tumoral cells (see **Fig. 3.10b**). TTh also has a comparative advantage with respect to inspection by infrared thermography, which, assuming a thermal uncertainty of ± 0.2 ˚C, requires ten days after tumor induction to be able to detect its presence, according to the data on **Fig. 3.10c. Fig. 3.10** clearly evidences the potential of TTh in combination with Ag_2S nanothermometers for early tumor detection when compared to conventional approaches. Taking into account that the characteristic tumor cycle time in our animal model is of 14 days, the application of TTh shortens the time required for tumor diagnosis by a remarkable 60%.

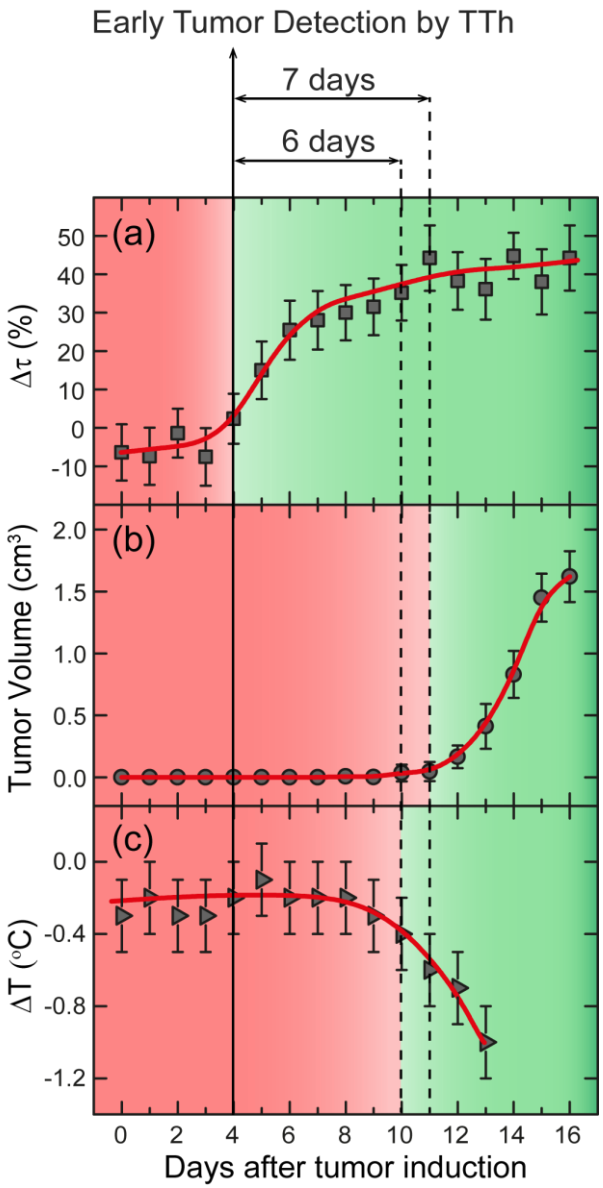

Figure 3.10 (a) Time evolution after tumor induction of $\Delta\tau$ (normalized difference between the thermal relaxation time of tumoral tissue with respect to that of the healthy tissue). **(b)** Time evolution of tumoral volume volume. **(c)** Time evolution after tumor induction of the surface temperature difference between tumor and healthy tissue as obtained with a thermographic camera. In all cases, the dots correspond to the experimental data obtained as an average of the n = 6 mice analyzed in this work and solid lines are included as guides for the eyes. The background colors and vertical lines indicate the time when the tumor becomes detectable by the different methods.

3.2.3 Physiological Basis of Early Tumor Detection by Transient Thermometry

The demonstrated capacity of TTh for early tumor detection is necessarily related to the different physiological changes that take place during the first stages of tumor

development, while it is still undetectable by direct observation. According to expressions (3.2.2) and (3.2.3), a developing tumor would be detectable by TTh if either (or both) its intrinsic physical properties, such as density or specific heat, or its blood perfusion are substantially modified as a consequence of tumor growth. The density of tumoral tissue was systematically analyzed in all the animals studied in this work by measuring tumor mass and volume after euthanasia. The experimentally measured average tumor density (1.06 ± 0.02 g·cm^{-3}) was very similar to that of the healthy tissue (close to 1 g·cm^{-3}) and consistent with the values found in the literature.[50] Further review of the available literature indicates that other intrinsic tissue properties that influence its thermal dynamics, including specific heat and thermal conductivity do not differ greatly between tumoral and healthy tissues.[50a, 51]

Therefore, we postulate at this point that changes in intrinsic tissue properties are not the cause of the large (close to 45%) variation experimentally observed in the thermal relaxation time of the tumor with respect to that of a healthy tissue. Thus, according to expression (3.3.3), such variance must be correlated with changes in the thermoregulation mechanisms through the blood perfusion, as well as with changes in the metabolic heat energy generation during tumor development. In order to verify this hypothesis, the blood perfusion images of the tumor were systematically acquired by laser speckle imaging (see ***Blood perfusion imaging in Section 2.7***).[52] Some representative perfusion images obtained at different stages of tumor development are shown in **Fig. 3.9d**. These images reveal how the progression of the tumor is accompanied by drastic changes in blood perfusion, as has been already reported.[53] A comparison of the blood perfusion images obtained at the onset of tumor development (right after cancer cell inoculation) and 14 days later evidences tumor progression brought about a significant reduction of the blood perfusion rate at the center of the tumor. As a way to quantify this reduction in blood flow, we have analyzed the perfusion images to calculate the relative blood perfusion rate change at the tumor *n* days after inoculation ($\Delta\boldsymbol{\omega_C(n)}$). We can define this parameter as:

$$\Delta\omega_C(n) = \frac{\omega_C(n)-\omega_H(n)}{\omega_H(n)} \qquad (3.2.7)$$

where $\boldsymbol{\omega_H(n)}$ is the blood perfusion rate in a healthy tissue as measured at day *n* after inoculation. The time evolution of $\Delta\boldsymbol{\omega_C(n)}$ is shown in **Fig. 3.11a** and it denotes a moderate increment during the first days (1-4) of tumor development and a drastic

reduction from the 5th day onwards. These two distinct regimes can be correlated with the initial development of a vascular network in the tumor environment (angiogenesis), required to ensure sufficient nutrition and oxygenation to an incipient tumor with a high metabolic activity. This initial stage is followed by a second one characterized by the onset of necrosis in the inner volume of the tumor. This is evidenced by a drastic reduction in the blood flow, caused by the high intratumoral extravascular pressure acting over the blood vessels. As a consequence of the decreased blood flow, inefficient uptake of oxygen and nutrients also play a strong role in promoting necrosis in the inner volume of the tumor.[54]

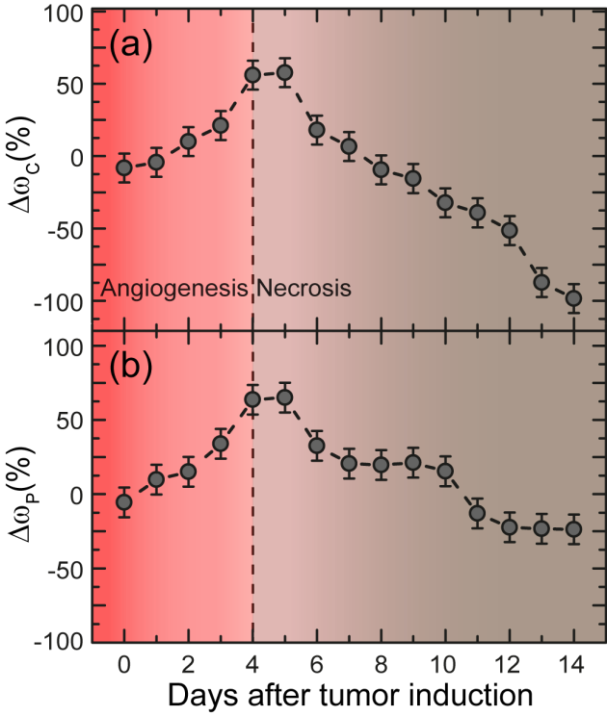

Figure 3.11 Time evolution after tumor induction of the change in blood perfusion as measured **(a)** at the center of the tumor ($\Delta\omega_C$) and **(b)** at the tumor periphery ($\Delta\omega_P$). Dots are experimental data and dashed lines are guides for the eyes. The background colors indicate the tumor evolution stages dominated by angiogenesis and necrosis, respectively.

The existence of these two well-differentiated stages is also evidenced in the analysis of the peripheral blood perfusion. **Fig. 3.11b** shows the time evolution of the relative change in the peripheral blood perfusion, defined as:

$$\Delta\omega_P(n) = \frac{\omega_P(n)-\omega_H(n)}{\omega_H(n)} \quad (3.2.8)$$

where $\boldsymbol{\omega_p(n)}$ is the peripheral blood perfusion measured at day *n* after tumor induction. In this case, we also observe a relevant increment in the peripheral blood perfusion in the first (1-4) days. This supports the dominant role of angiogenesis during the early stages of tumor development. This increase in peripheral blood flow starts a smooth reduction on day 5 after tumor induction and recovers its initial value at the terminal tumor stage. This downward trend can also be explained in terms of the appearance of necrosis in the center of the tumor. Note that at day 14 (final stages of tumor development) the peripheral blood perfusion rate has returned to the value it presented before tumor induction (i.e. at day $n = 0$), whereas the blood perfusion at the central tumor volume is virtually nonexistent. These observations suggest that after 14 days of growth, the tumor is constituted by a well-advanced necrotic central core (with a minimum presence of blood vessels) surrounded by an external highly metabolic tumor tissue with a dense vasculature. In order to verify this assumption, we performed a histological analysis of an excised tumor, evaluating the size of the necroting area using hematoxyline-eosine staining and visualizing the angiogenesis by SMA and CD31 immunoreaction, as detailed in the Supporting Information. The histological results are summarized in **Fig. 3.12**, where the low density of blood vessels in the central area of tumor, when compared to that at the tumor periphery, is evidenced. The central area of the tumor was found to be necrotic, as observed in SMA and CD31 immnunohistochemistry images shown in **Fig. 3.12**. These results further support the conclusions extracted from blood flow images obtained by laser speckle (Figure 2(d) and Figure 4). It is worth noting that, although the results from blood perfusion rate provide supplementary information about the tumor development and can help to discriminate between the two different regimes (angiogenesis and necrosis), this technique still presents great limitations for early tumor diagnosis. In particular, as blood flow values do not follow a monotonous trend, it is possible to observe similar blood perfusion rates at different tumor development stages due to the interplay between the changes happening at the core of the tumor and its periphery. This makes it

impossible to unequivocally determine the stage of development of a tumor through laser speckle imaging alone.

Based on the results shown in Figure 4, we can now establish the biophysical origin of the capacity of TTh for early tumor detection. Note that on day 5 after tumor induction, the onset of intratumoral necrosis causes a significant reduction in the blood perfusion inside the tumor, where our Ag_2S nanothermometers are located. According to expression (3), the intratumoral thermal relaxation time, $\boldsymbol{\tau_c}$, is inversely proportional to the intratumoral blood perfusion rate. Thus, once the necrosis process starts, the significant reduction in blood perfusion leads to a significant increase in the thermal relaxation time of the tumoral volume. The very large differences (up to 45%) observed between the thermal relaxation times of intratumoral and healthy tissues was indeed expected, considering that intratumoral blood perfusion undergoes a drastic reduction (close to 100%) as the tumor develops. We can therefore state that TTh can detect the presence of a developing tumor once intratumoral necrosis starts to occur. At this stage, TTh is a highly sensitive technique because of the changes that take place in the intratumoral blood perfusion rate.

The relevant increase in blood flow observed by laser speckle imaging at the very early stages of tumor development (as shown in figure 4) is, as discussed above, directly related to the appearance of angiogenesis. However, this did not have a direct impact on the thermal relaxation time of tumoral tissue, which was somehow unexpected, as according to expresion (3), an increment in blood perfusion should lead to a decreased thermal relaxation time. We postulate at this point that this is related to other changes happening in the early stages of tumor development, when the characteristic increase in blood perfusion rate is accompanied by an increase in metabolic activity (included in expression (3.3.3) through the term $\boldsymbol{\alpha}$). According to our experimental results, we propose that the increment in blood perfusion rate is somehow balanced by the increment in the metabolic activity in such a way that the thermal relaxation time remains unchanged at the early stages of tumor development. Therefore, nanoparticle assisted TTh is not only capable of early tumor detection, but is also capable of providing a first order diagnosis discriminating between two tumor stages. Early tumor development stages, characterized by a large metabolic activity, significant angiogenesis and high blood perfusion rate at the tumor volume and periphery can be

identified through TTh by similar thermal relaxation times for both tumoral and healthy tissues. More advanced stages of tumor development, characterized by a significant reduction of intratumoral blood perfusion as a consequence of necrosis, can be accurately detected by TTh through thermal relaxation time that are significantly higher than those of healthy tissues.

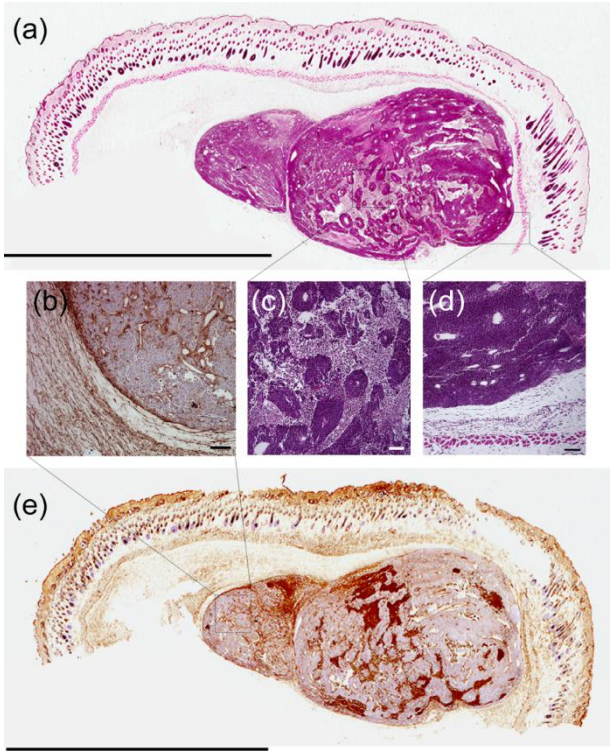

Figure 3.12 Microphotographs of histological transversal sections of the melanoma. **(a)** Panoramic view of the melanoma stained by hematoxylin-eosin. **(b)** High magnification of the squared area in (e) showing the angiogenic satellite nodule of the melanoma. **(c)** High magnification of the squared area in (a) showing the predominant necrotic tissue in the central area of the melanoma. **(d)** High magnification of the squared area in (a) showing vessels and non-necrotic tissue. Notice the increment in angiogenesis and less abundant necrotic tissue on the periphery of the melanoma, more evident in the satellite nodule. **(e)** Panoramic view of CD31 immunoreaction of the melanoma. Calibration toolbars: (a), (e): 100 µm and (b)-(d): 10 µm.

3.2.4 Numerical Simulations

In order to compare the experimental results to theoretical predictions and get additional insights on the thermal relaxation dynamics of well-developed tumors, we have performed numerical simulations in a realistic computer mouse model using a transient solver that employs the finite-difference time-domain (FDTD) method.[55] Details about the numerical calculations here discussed can be found in the Supporting

Information. **Fig. 3.13a** shows the mouse virtual model used. Note that simulation software allows simulating the thermal dynamics of a mouse similar to those used in experiments, including its posture in the imaging chamber. In our calculations, we included a tumor phantom with a total volume close to 1.5 cm^3 that, according to Figure 3(b), corresponds to a well-developed tumor. Based on the histopathological findings summarized in Figure 4, the microcirculation of the tumor was simulated to have a predominant peripheral vascularization, with most of the vessels running parallel to the tumor surface (see detailed image of tumor phantom included in Figure 6(a)). Then the thermal relaxation dynamics of the simulated tumor after moderate and well-localized heating was numerically calculated. **Fig. 3.13b** shows the temperature maps of the tumor corresponding to different times after the end of the heating process. The time evolution of the intratumoral temperature, shown in **Fig. 3.13c**, was then extracted from the analysis of these thermal maps. For the sake of comparison, the normalized thermal transient provided by numerical simulations for a healthy tissue is also shown in Figure 6(c). Note that numerical calculations well reproduce the experimental evidence: tumor development leads to a slowdown in thermal relaxation. Indeed, the numerical calculations yield thermal relaxation times of 55 and 43 s for the tumoral and healthy tissues, respectively. Thus, numerical calculations predict a relative change in relaxation time close to $\Delta\boldsymbol{\tau_{calc}} \cong 30\%$, which is in reasonable agreement with the experimental results ($\Delta\boldsymbol{\tau_{exp}} \cong 40\%$, as obtained from Figure 3(a)). Thus, numerical simulations reproduce reasonably well the results obtained experimentally by the TTh technique. This result does not only provide further support to the previous interpretation of the experimental data, but also expands the potential applications of TTh beyond tumor detection, showing that it could be a valuable diagnosis tool for a wider array of diseases.

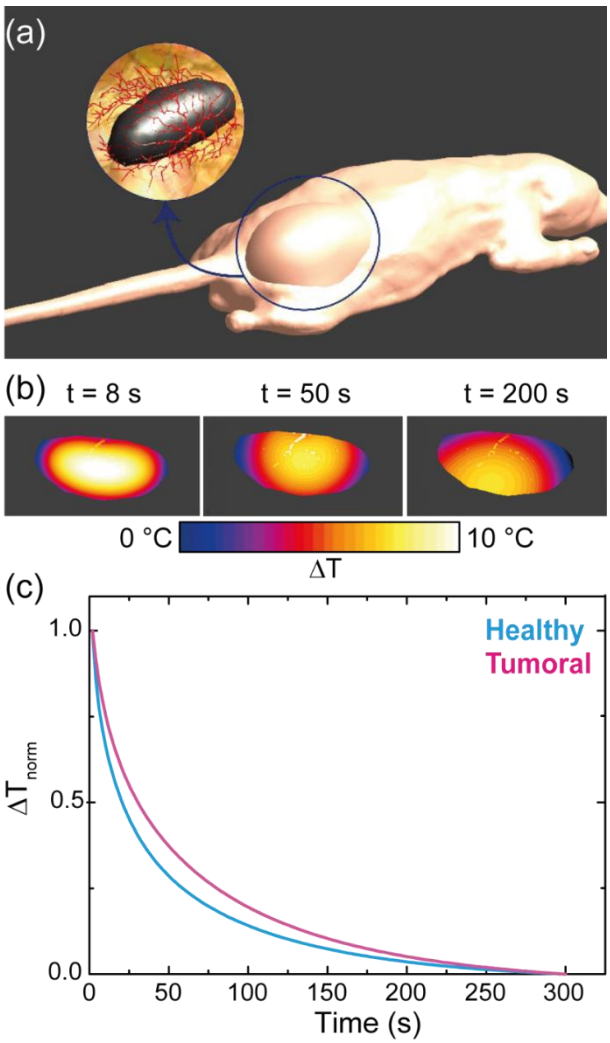

Figure 3.13 (a) Mouse virtual model used in the numerical simulations model. **(b)** Temperature maps of the tumor corresponding to different times after starting the cooling process. **(c)** Time evolution of temperature extracted from the analysis of the thermal maps in (b) for an advanced-stage tumor and a healthy tissue.

3.3 Ag_2S dot-to-Superdot transformation triggered by femtosecond laser pulses.

In the present section of this thesis, we develop a novel methodology that permits a substantial increment in the quantum yield of Ag_2S dots. The process is based on the dispersion of the as-synthesized Ag/Ag_2S heterodimers in chloroform and its subsequent irradiation with ultra-fast laser pulses, which induces the explosion of metallic silver nanoparticles and the subsequent formation of an AgCl shell around Ag/Ag_2S heterodimers. This process reduces the surface traps while minimizing dot-to-medium transfer nonradiative events that results in a 50 fold QY enhancement. The potential use of Ag_2S superdots for low dose whole-body in vivo imaging is also evaluated and their performance compared with classical NIR-II luminescent in vivo probes.

3.3.1 Physical characterization of Ag_2S dots before and after ultrafast laser irradiation.

The average size and shape of as synthesized nanoparticles were obtained through high-angle annular dark-field imaging scanning transmission electron microscopy (HAADF-STEM). As can be observed in **Fig. 3.14a,** the HAADF-STEM micrograph of the as synthesized nanoparticles exhibiting an elliptical shape and average size of 9.5±1 nm (See **Supporting Fig. 4.7**). Two well-distinctive regions concerning electrodense could be identified; a high electrodense core (lighter area) located eccentrically which corresponds to parts of the sample that absorbs fewer electrons from the electron beam and a less electrodense (darker) area that constitutes the major part of the nanoparticle. The high resolution STEM of a typical particle reveals a remarkable crystalline structure, **Fig. 3.14b** with lattice fringe d_{111} = 2.30 Å in the higher electrodense part, in accordance with those of cubic Ag phase (JCPDS 04-0783), while the less electrodense area exhibits a lattice fringe of d_{-104} = 2.37 Å that matches with the monoclinic Ag_2S (JCPDS No. 14-0072). The less electrodense area in **Fig. 3.14b** is supposed to be Ag_2S, as the density of Ag_2S (7.2 $g \cdot cm^{-3}$) is smaller than that of Ag (10.505 $g \cdot cm^{-3}$). This assumption is corroborated by the energy dispersive X-ray spectroscopy analysis (EDS) showed in **Fig. 3.14c**, **d** and **e**. Here, we can observe that while the core of the

nanoparticles is rich in Ag element, the S is mainly located in the outer part of the nanoparticles. The anisotropic distribution of elements is depicted in the Net X-ray Intensity profiles shown in **Fig. 3.14g**. In this figure, we can observe that the maximum of the X-Ray intensity assigned to the Ag atoms arises from the electrodense region, while the X-ray intensity signal attributed to the S atoms becomes maximum in the less electrodense area. The elemental analysis of an heterodimer shows a Ag:S ratio of 74:26. All these results support the presence of a metallic Ag region within an Ag_2S matrix.

After ultrafast illumination with 50 fs pulses during 90 min (9 W/cm^2), the average diameter of the nanoparticles increases from 9.51 nm to 12.31 nm, while the size of the metallic Ag core remains constant at around 5.1 nm, see **Fig. 3.14h** (more HAADF-STEM images of the nanoparticles after ultrafast laser irradiation as well as the size distribution histogram are showed in **Supporting Fig. 4.7**). High resolution STEM of a representative Ag/Ag_2S heterodimer after ultrafast laser irradiation reveals, again, two well differentiated crystalline regions, an electrodense one with lattice fringe of d_{111} = 2.30 Å, that agree with metallic Ag and a less electrodense area with a lattice fringe of d_{110} = 2.50 Å, as seen in **Fig. 3.14i.** In this figure is also observed the presence of 1 nm thickness shell as a grey region around the nanoparticles. Energy dispersive X-ray spectroscopy analysis reveals that the resulting nanoparticles are composed by Ag and S, which are distributed like in the as-synthetized nanoparticles. Interestingly, EDS analysis detects the presence of Cl atoms distributed around laser irradiated heterodimers, which is a result of the formation of an AgCl shell, see **Fig. 3.14j, k, l, m**. The elemental analysis of a laser treated heterodimer shows a Ag:S:Cl ratio of 68:23:7. Again the excess of Ag would indicate the conservation of rich silver core within the heterodimers.

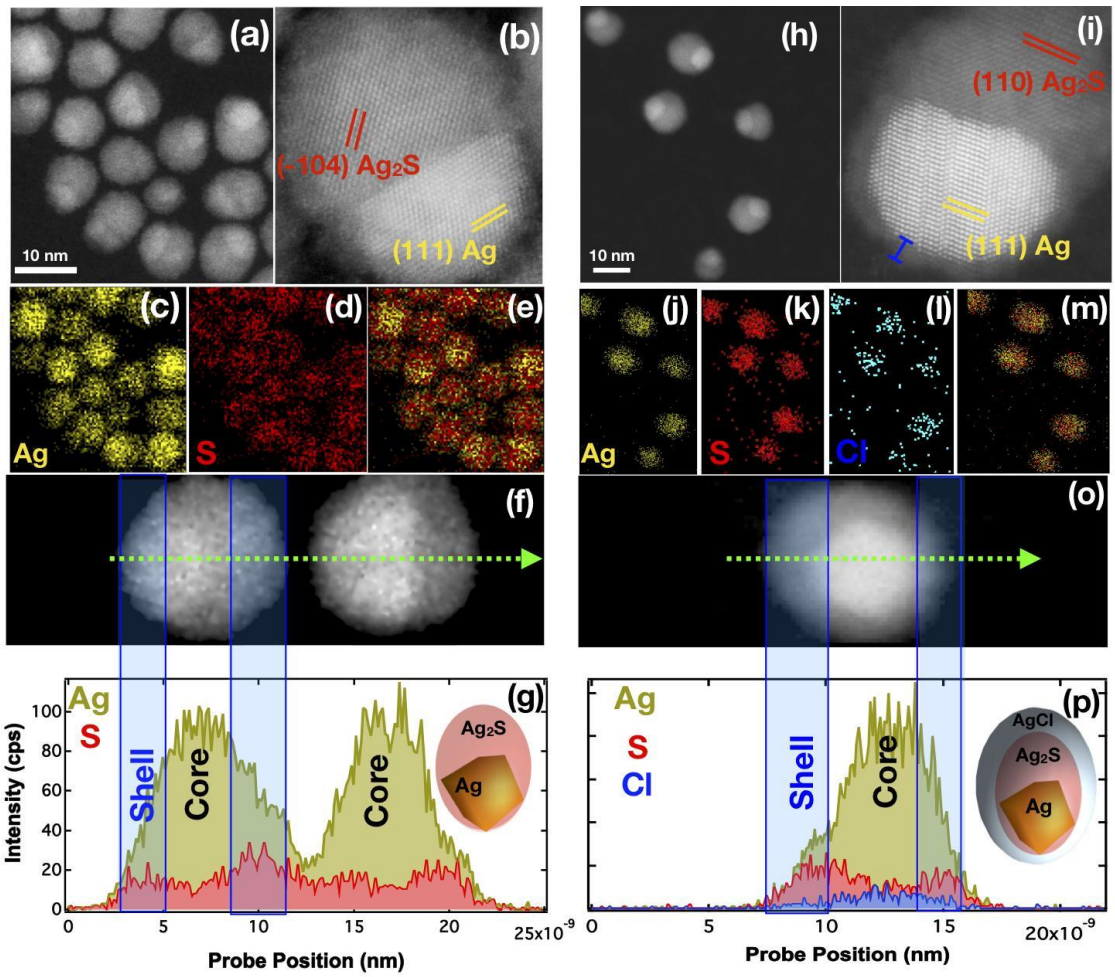

Figure 3.14 Tuning structural and chemical properties through ultra-short laser irradiation. (a) HAADF-STEM micrograph the as-synthetized dots. **(b)** High resolution transmission electron microscopy of as-synthetized dots showing lattice fringes d_{111} and d_{-104} of cubic Ag and monoclinic Ag_2S respectively. 2D EDS mapping of the spatial distribution of **(c)** Ag, **(d)** S and **(e)** Ag+S of the dots. **(f)** magnified STEM micrograph of dots. **(g)** Net X-ray intensity profiles extracted from the green arrow marked in image **(f)**, note how the Ag/S ratio increases at the edges of the dots, which coincides with the electrodense area. The inset shows a model nanoparticle. **(h**) HAADF-STEM micrograph of Ag/Ag_2S heterodimers after ultrafast laser irradiation with 50 fs laser pulses during 90 min at a fluence of 9 W/cm^2. **(i)** High resolution transmission electron microscopy of an ultrafast laser irradiated Ag/Ag_2S heterodimer showing lattice fringes d_{111} and d_{110} of cubic Ag and monoclinic Ag_2S, respectively. Note in this figure the presence of a shell marked with a blue bracket around the nanoparticle. 2D EDS mapping of the spatial distribution of **(j)** Ag, **(k)** S, **(l)** Cl and **(m)** Ag+S+Cl of an ultrafast laser irradiated Ag/Ag_2S heterodimer. **(o)** Magnified STEM micrograph of an ultrafast laser irradiated Ag/Ag_2S heterodimer. **(p)** Net X-ray intensity profiles extracted from the green arrow marked in image **(o)**, where we can observe the presence of Ag, S and Cl. The inset on the left shows a schematic representation of an Ag/Ag_2S heterodimer after ultrafast laser irradiation.

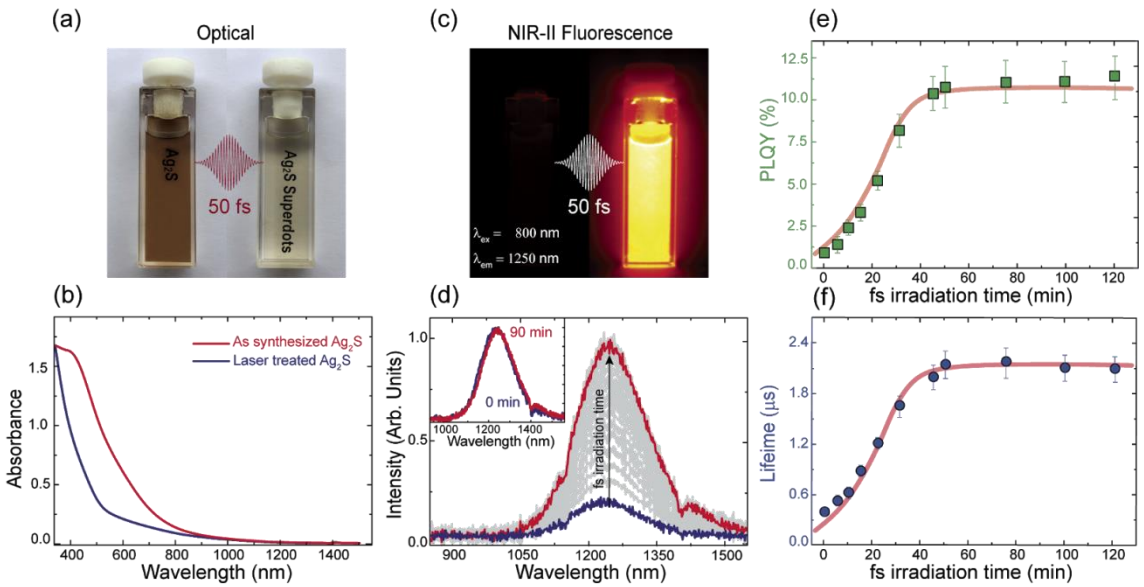

Figure 3.15 Optical transformation of Ag_2S dots into superdots. (a) Optical image of a colloidal solution of Ag_2S dots in $CHCl_3$ before and after ultrafast laser irradiation (50 fs laser pulses during 90 min at a fluence of 9 W/cm^2). **(b)** VIS-NIR extinction spectra of colloidal solutions of dots in $CHCl_3$ before and after ultrafast laser irradiation. **(c)** NIR-II fluorescence image of a colloidal dispersion of dots before and after ultrafast laser irradiation (90 min). **(d)** NIR-II emission spectra generated by a colloidal suspension of dots in $CHCl_3$ during ultrafast laser irradiation (90 min). Solutions where optically excited with an 808 nm laser diode. **(e)** Fluorescence Quantum Yield of Ag_2S dots in $CHCl_3$ after being subjected to ultrafast laser irradiations processes of different durations. **(f)** Fluorescence lifetime of Ag_2S dots in $CHCl_3$ after being subjected to ultrafast laser irradiations processes of different durations. In **(e)** and **(f)** dots are experimental data and the red line is a guide for the eyes.

3.3.2 Optical transformation of Ag_2S dots into superdots.

Promoted structural changes under ultrafast laser pulses were summarized in **Fig. 3.14** and they are accompanied by a remarkable modification of their optical properties, which can be easily observed by direct optical inspection. **Fig. 3.15a** shows the optical image of a colloidal dispersion of as synthetized Ag/Ag_2S heterodimers (hereafter referred as to Ag_2S dots) in $CHCl_3$ before and after 90 min irradiation with 50 fs laser pulses that, according to previous section, leads to the creation of Ag/Ag_2S@AgCl heterodimers (hereafter referred as Ag_2S superdots). Ultrafast laser irradiation induces a clear color change, becoming the solution more transparent. This color change occurs progressively during illumination with ultrafast laser pulses as it is evidenced in **Supporting Fig. 4.14a**. The absorption spectra of both solutions, before and after 90 min irradiation, are included in **Fig. 3.15b**. This figure evidences that 50 fs pulses lead

to a remarkable decrease of the absorption coefficient in the 400-800 nm range. Data included in **Supporting Fig. 4.8** reveals that this change takes place progressively during ultrafast laser irradiation. In the as-synthesized solution, the absorption spectrum reveals the presence of a shoulder around 400 nm, which is attributed to the plasmonic band of sub-100 nm Ag nanoparticles and that is conspicuously reduced upon the laser treatment (See **Supporting Fig. 4.8a** and **b**).[56] Interestingly, not only the absorption properties are affected by ultrafast laser irradiation; also the fluorescence brightness of the dots is significantly increased. **Fig. 3.15c** displays a NIR-II fluorescence image of the colloidal dispersion of the dots before and after ultrafast laser irradiation (50 fs, 90 min, 9 W/cm^2). Before ultrafast laser irradiation the dots produce a luminescence hardly detected by our NIR-II imaging system. By contrast, ultrafast laser irradiation increases tremendously the fluorescence brightness of the solution. Such an increment is not accompanied by any relevant change in the spectral shape of emission. This is evidenced in **Fig. 3.15d** that shows the time evolution of the NIR-II emission generated by Ag_2S dots during fs laser irradiation. **Fig. 3.15e** shows the fluorescence QY of different colloidal solutions of Ag_2S dots in $CHCl_3$ after being irradiated during different times with ultrafast laser pulses (50 fs, 9 W/cm^2). QY increases monotonously with irradiation times for treatment durations shorter than 40 min. Longer irradiations do not lead to any further improvement of QY. As-synthetized dots show a QY of 0.25% that increases up to 10 % after 50 min irradiation with 50 fs pulses. This constitutes a 50 fold enhancement, explaining why we denote the Ag/Ag_2S@AgCl heterodimers as superdots. QY enhancement is also accompanied by a substantial enlargement of fluorescence lifetime from 200 ns up to 2 µs as it evidenced in **Fig. 3.15f** (decay lifetime curves are displayed in **Supporting Fig. 4.8d**). Indeed the increment in fluorescence time with the irradiation time follows the same trend as that observed for QY in **Fig. 3.15e** and is confirmed to be related to the reduction of non-radiative pathways, shown no signs of possible influence of fluorescence self-absorption during our lifetime measurements (see **Supporting Fig 4.9)**

3.3.3 Required conditions for dot-to-superdot transformation.

The ultrafast laser dor-to-superdot depends critically on the irradiation density. **Fig. 3.16a** shows the time evolution of NIR-II fluorescence intensity generated by a colloidal solution of dots in $CHCl_3$ as obtained for different power densities while

keeping constant pulse duration (50 fs), repetition rate (1 kHz), and average power (0.6 W). For power densities below 3 W/cm^2, that seems to be a threshold value, non-appreciable improvement in luminescent properties is observed. For power densities between 3 W/cm^2 and 9 W/cm^2 NIR-II fluorescence intensity increases with the irradiation time until it saturates. In this range of power densities, the slope of the intensity vs time curve ($\eta = dI/dt$) depends strongly on the irradiation pulse energy (E_p). In fact, we find that $\eta \propto E_p^2$, which would suggest that the dot-to-superdot transformation is triggered by a two-photon absorption process (see **Supporting Fig. 4.10**). Irradiation energies above 10 W/cm^2 lead to a decrease in the emitted intensity for long irradiation times that could be attributed to the sample degradation, such an effect is highlighted when the irradiation energies are close to 100 W/cm^2. Under these conditions, the increment of the intensity is followed by an abrupt diminish of the signal, rendering to a non-luminescent and completely transparent solution that indicate the completely sample degradation.

Fig. 3.16b demonstrates that ultrafast laser induced dot-to-superdot only occur when the as-synthesized Ag_2S dots are dispersed in $CHCl_3$. Indeed, when they are suspended in water, toluene or hexane, irradiation with 50 fs pulses leads to a decrease in their NIR-II fluorescence that can be attributed, as discussed in **Supporting data and information section 4.2**, to laser-induced thermal loading during irradiation. The relevance of the presence of silver also rules out to be critical. In fact, neat Ag_2S dots without any Ag nanoparticles were synthetized by a procedure detailed in **Material Section 2.1 (c)** Ultrafast laser irradiation of these pure Ag_2S dots does not produce any fluorescence improvement as it is evidenced in **Fig. 3.16c**. Thus, we conclude that ultrafast laser driven dot-to-superdot transformation requires not only the presence of $CHCl_3$ but also of Ag nanoparticles in the dispersion. Not only that, the dynamics of the dot-to-superdot transformation critically depends on the laser pulse duration. **Fig. 3.16d** shows the time evolution of the NIR-II fluorescence intensity generated by a dispersion of Ag_2S dots in $CHCl_3$ during irradiation with 808 nm laser pulses of 50, 100, 200 and 550 fs. All the curves included in this figure were obtained with the same power and laser density and wavelength (0.6 W and 9 W/cm^2, respectively). The efficiency of dot-to-superdot transformation, estimated from the magnitude of NIR-II luminescence enhancement, decreases as the pulse duration increases. In addition, CW laser

irradiation does not lead to any NIR-II fluorescence improvement, indicating the absence of any dot-to-superdot transformation.

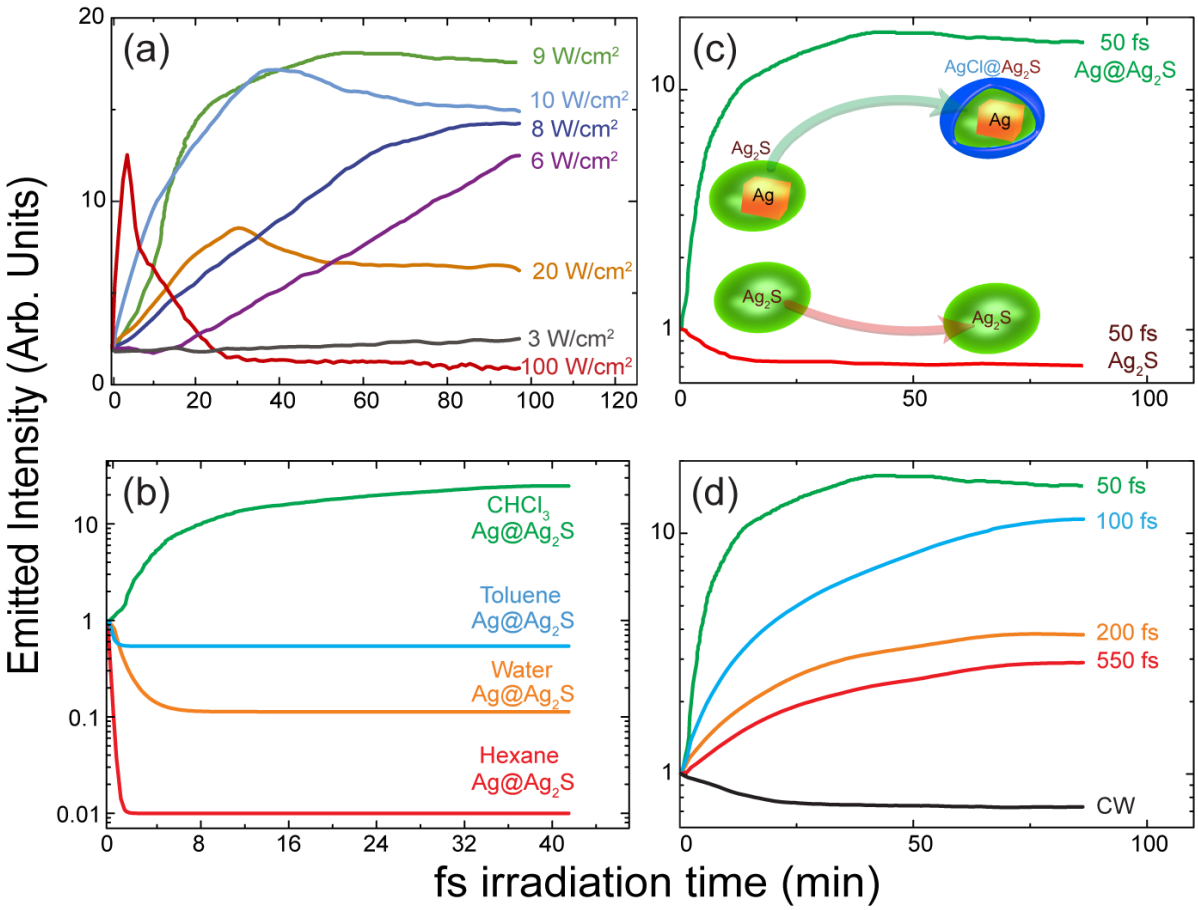

Figure 3.16 Required conditions for laser induced transformation of $Ag@Ag_2S$ dots into superdots. **(a)** Time evolution of the NIR-II fluorescence generated by colloidal solutions of dots in $CHCl_3$ while being irradiated with different power densities. In all the cases pulse width was set to 50 fs.**(b)** Time evolution of the NIR-II fluorescence generated by $Ag@Ag_2S$ dots suspended in different solvents during laser irradiation with 50 fs, 808 nm wavelength laser pulses. Average laser power density was in all the cases set to 9 W/cm^2. **(c)** Time evolution of the NIR-II fluorescence generated by $Ag@Ag_2S$ and Ag_2S dots during laser irradiation with 50 fs, 808 nm wavelength laser pulses. Average laser power density was in all the cases set to 9 W/cm^2. **(d)** Time evolution of the NIR-II fluorescence intensity generated by $Ag@Ag_2S$ dots in $CHCl_3$ as obtained for different pulse durations. In all the cases the same power density is used (9 W/cm^2).

3.3.4 Dot-to-superdot transformation mechanisms.

Based on the previous experimental evidences included in **Figs 3.14-16** and a plausible explanation can be enounced for the dot-to-superdot transformation. This is schematically shown in **Figs 3.17**. We assert also based on arguments corroborated by

the synthesis procedure described in **Material Section 2.1 (c)**, that the as-prepared dispersions of Ag_2S dots also contain Ag nanoparticles whose plasmonic resonance is, indeed, responsible of the extinction peak at around 400 nm (as previously shown in **Fig. 3.15b**). When excited by 808 nm ultrafast pulses, two photon absorption by Ag NPs leads to the local induction of a high free electron density that results in their coulomb explosion.[57] The key role of multiphoton excitation is supported by the requirement of ultrafast laser pulses that ensure high photon densities and, hence, allows for sequential absorption through virtual states of Ag NPs.[58] Coulomb explosion of Ag NPs leads to an increment of highly reactive Ag atoms in the solution that react with $CHCl_3$ yielding silver chloride (AgCl): $Ag+Cl \rightarrow AgCl$. The interaction of the laser induced AgCl molecules with the highly reactive surface of Ag_2S dots results in the formation of a protective shell of AgCl. Therefore, we state that after ultrafast laser irradiation, the Ag_2S low-bandgap semiconductor (0.9 eV) is covered with an inorganic shell of a higher-bandgap AgCl (5.13 eV) of a thickness of some monolayers as seen in **Fig. 3.14a**.[59] This protective shell strongly reduces the non-radiative transitions that involve the vibronic activation of solvent molecules $CHCl_3$, and the formation of shallow, or deep, midgap states as surface traps that provide pathways for non-radiative exciton recombinations. Therefore, this laser-induced passive shell leads to an increment in the NIR-II fluorescence intensity and to an enlargement of the fluorescence lifetime as well as the QY. We also state that both dots and superdots could be damage if they are subjected to an excessive irradiation dose. This explains why, for high irradiation laser power energies, the initial NIR-II luminescence enhancement is followed by a nonreversible quenching (see **Fig. 3.16a**).

The above proposed mechanism states that the dot-to-superdot transformation starts with the light absorption by Ag NPs that, indeed, behave as primary inductors of the transformation. This would mean that in absence of Ag NPs in the dispersion ultrafast laser irradiation would not lead to any improvement in the optical properties of Ag_2S dots. This is exactly what has been experimentally observed in **Fig. 3.16c** where it is clear that in absence of Ag NPs ultrafast laser irradiation of single Ag/Ag_2S dots does not produce any improvement in their optical properties.

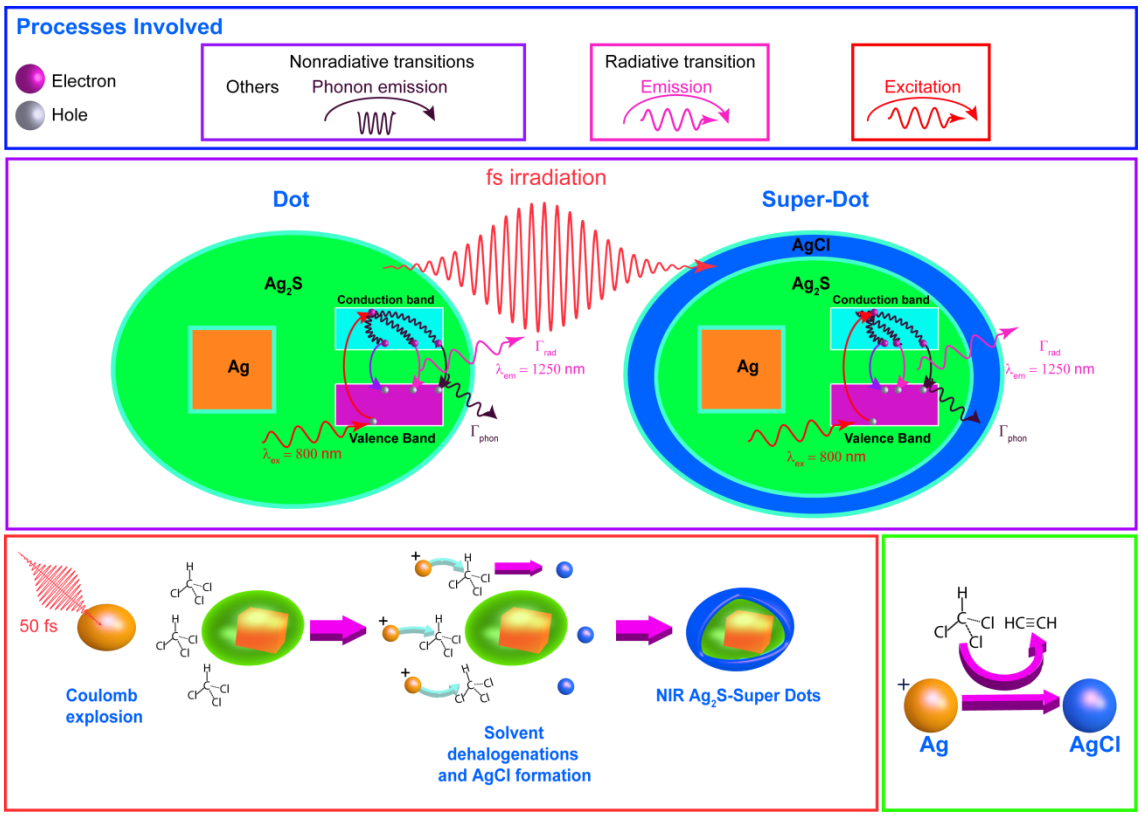

Figure 3.17 Dot-to-Superdot transformation mechanisms. (a) Schematic representation of the physico-chemical mechanisms underlying the ultrafast laser induced dot-to-superdor transformation. Upon illumination with ultrafast infrared laser pulses, multi-photon excitation of Ag nanoparticles would lead to their coulomb explosion. The Ag atoms generated by coulomb explosion react with $CHCl_3$ molecules forming AgCl that reacts with the surface of the Ag/Ag_2S dots forming a protective layer. **(b)** Typical dehalogenation reaction catalyzed by the presence of Ag, which produces AgCl. **(c)** Schematic representation of the different de-excitation pathways taking place in both Ag/Ag_2S dots and superdots.

3.3.5 In Vivo NIR-II imaging with Ag_2S Superdots

The potential application of Ag_2S Superdots for NIR-II in vivo imaging is here tested by transferring them from its original solvent, chloroform, to water by means of a ligand exchange procedure described in detail in **Supporting data and information section 4.2**. The adhesion of hydrophilic and bifunctional HS-PEG-COOH ligands on the surface of Ag_2S Superdots makes them stable in Phosphate Buffer Saline (PBS) without any sign of precipitation during months. The average, hydrodynamic diameter and Z-potential after the ligand exchanges are 22 nm, and -25 mV. PEG coating and dispersion into PBS causes a reduction in the fluorescence decay time from 2 down to 0.7 micros (see **Supporting Fig. 4.15a**). This is very likely caused by a combination of the presence of surface defects promoted during the ligand exchange process and multiphonon relaxation favored by the vibration modes of water molecules. Despite the

activation of these nonradiative processes, the QY of the PEG coated superdots in PBS is as large as 5.7% (see Section X in the SI). This QY value is still, by far, a hanker-dreamy improvement when compared with the QY of commercial PEG coated Ag_2S dots (**Supporting Table 4.3**). Fluorescence lifetime of PEG coated Ag_2S superdots in PBS is 700 ns, that is more than ten times larger than that reported for commercial Ag_2S dots in PBS (**Supporting Fig. 4.15**). Such a high QY suggest the potential application of our PEGylated superdots for high contrast, low dose NIR-II in vivo imaging. This possibility is here evaluated by performing a comparative study in respect to well-established NIR-II fluorescent probes such as commercial Ag_2S dots, Neodymium-Doped Lanthanum Fluoride (LaF_3:Nd^{+3}) and single walled carbon nanotubes (SWCNTs).[1a, 60] The FDA approved ICG dye is not included in this comparative study as preliminary experiments revealed the poor spectral overlap between its emission tail and the spectral response of our NIR-II imaging system (**Supporting Fig. 4.16**).[61] We subcutaneously inject into four different mice 100 µL of a PBS solution containing, in each case, Ag_2S superdots, Ag_2S dots, NPs:Nd-Yb and SWCNTs. In all the cases the same mass concentration is used: 1.5 mg/mL. **Fig. 3.18a** shows the in vivo NIR-II fluorescence images in living mice obtained in each case for 808 nm irradiation power densities ranging from 227 down to 0.3 mW/cm^2. The superior performance of our Ag_2S superdots is evident. They make possible the acquisition of a reliable fluorescence image with a irradiation power density as low as 0.3 mW/cm^2. This does not only allows the acquisition of in vivo images with cost effective excitation sources but also ensures a minimum thermal loading during in vivo imaging acquisition (**Supporting Fig. 4.17** in **Supporting data and information section 4.2**) [62]. At such ultra-low illumination power densities no fluorescence image was obtained when using any of the other three tested nanoprobes. The improvement achieved by using Ag_2S superdots is quantified in **Fig. 3.18b** that includes the power dependence of the signal to noise ratio (SNR) calculated from the fluorescence images obtained at different 808 nm laser power densities. From **Fig. 3.18b** we conclude that the brightness improvement achieved during ultrafast laser irradiation reduces by almost two order of magnitude the minimum illumination density that can be used for in vivo bioimaging. Such enhancement is also evidenced when comparing the illumination conditions here used to those employed in previous works dealing with "conventional " Ag_2S dots, SWCNTs

and rare earth doped nanocrystals (see **Supporting Table 4.4** in **Supporting data and information section 4.2**).

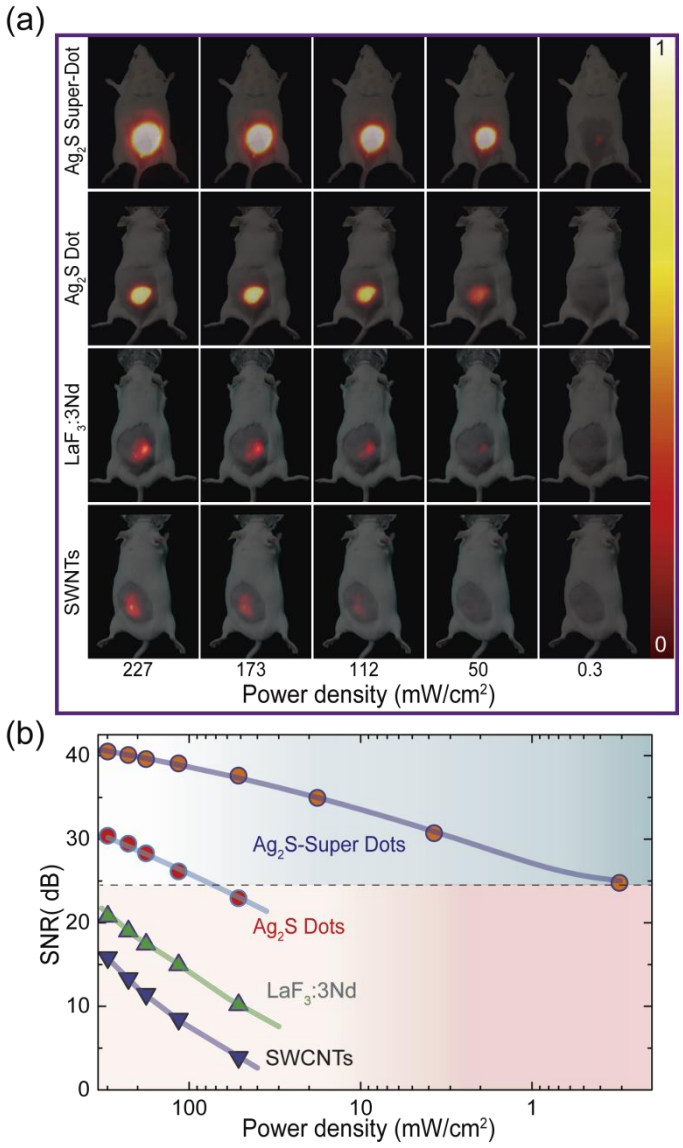

Figure 3.18 In vivo brightness of Ag_2S Superdots: a comparison with their competitors. (a) NIR-II fluorescence images of a group of mice which were subcutaneously injected into their limb muscles with colloidal aqueous solutions containing Ag_2S Superdots, comercial Ag_2S dots, SWCNTs and Nd-Yb doped NPs. In all the cases the same mass of nanoparticles were injected. The different images for same optical probe correspond to different 808 nm power density illumination**. (b)** The signal to noise ratio as a function of power density quantified from the analysis of the in vivo NIR-II images as obtained for the the four NIR-II nanoprobes here studied. Note that the use of Ag_2S Superdots allows the use, in exactly same experimental conditions, excitation power densities almost two order of magnitude lower than for the other NIR-II probes.

The superior brightness of Ag_2S superdots allows in vivo video rate NIR-II imaging while maintaining the illumination density and the administered dose at minimum values. This, in turns, reduces the potential risk of toxicity and keep at minimum the undesired thermal loading caused by the tissue absorption of 808 nm radiation. **Fig. 3.19a** shows the NIR-II images obtained at different times after intravenous administrations of 100 μL of PEG-coated Ag_2S superdots dispersed in PBS (at a concentration of 0.15 mg/mL). This leads to a total dose of 15 μg that corresponds to a dose per mouse mass of 0.37 mg/Kg. This is more than one order of magnitude lower than, for instance, the administered dose previously used for NIR-II video recording using "conventional" Ag_2S dots (200 μg) [19b]. The NIR-II video is recorded by using an 808 nm laser excitation density of 50 mW/cm^2 that is three times lower than the excitation density employed for NIR-II video recording using SWCNTs (140 mW/cm^2).[60b] The excitation density here used is also six times lower than the safe threshold (329 mw/cm^2) at this wavelength as have been established by the International Commission on Non-ionizing Radiation Protection (ANSI Z136.1-2000). **Supporting Table 4.4** compares the illumination densities and administration doses here used with those reported in the literature for NIR-II in vivo imaging based on fluorescent nanoparticles. NIR-II video allows to elucidate the biodistribution tracking of our Ag_2S superdots. The time evolution of the fluorescence emission intensity generated by the Ag_2S superdots at liver, spleen, heart and femoral artery after intravenous injection are displayed in **Fig. 3.19b**. At the first 3 min postinjection the PEG-coated superdots were mainly circulating and gathering in the liver, spleen and heart. For times longer than 30 min Ag_2S superdots are transferred and accumulated into the liver and spleen. The high accumulation rates in the liver and spleen has been commonly reported and such behavior are related to filtration mechanism promoted by the reticuoendothelial system (RES).[63] The fluorescence signal generated at the femoral artery is assigned to the presence of Ag_2S superdots in the bloodstream. By fitting a first-order exponential on this curve we have estimated an average circulating time for our Ag_2S superdots close to 20 min. Time resolved NIR-II images suggest that 3 hours after injection most of the Ag_2S superdots have been accumulated at liver and spleen. This fact has been corroborated by ex-vivo NIR-II imaging of the different organs. NIR-II fluorescence and optical images of liver, spleen, heart and lung are displayed in **Fig. 3.19c.**

Finally, the in vivo toxicity of our Ag_2S superdots is evaluated. We analysed the time evolution of weight, daily food income and temperature of a group of 4 CD1 mice after intraperitoneal administration of 300 µL of a solution of Ag_2S superdots in PBS at a concentration of 500 µg/mL. This constitutes a total administration dose of 150 µg of Ag_2S superdots that is one order of magnitude larger than that used for NIR-II in vivo video recording. Results are compared with those obtained from a "control" group of 4 mice after administration of 300 µL of PBS. Experimental data included in **Fig. 3.19d** reveal that, even for such "high" administration doses, no differences are found when comparing the behavior of both groups. This suggest a negligible in vivo toxicity of our Ag_2S superdots. This was, indeed, expected based on the already demonstrated low toxicity of Ag_2S superdots. Data included in **Fig. 3.19d** also reveal that the addition of a protective AgCl shell does not lead to any additional toxicity.

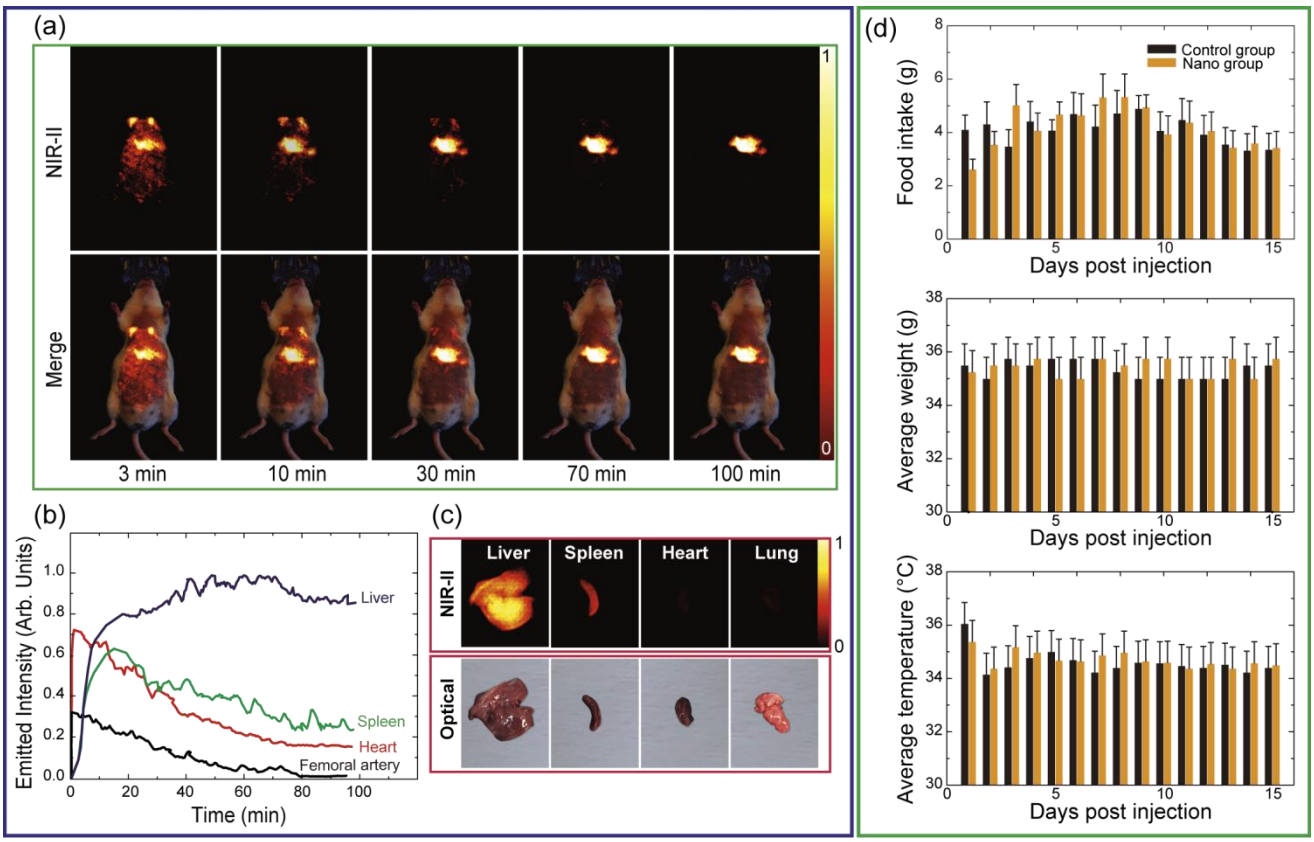

Figure 3.19 In vivo time resolved imaging with Ag_2S Superdots. (a) NIR-II fluorescence images as obtained at different times after intravenous injection of 100 µl of a solution of Ag_2S superdots in PBS at a concentration of 0.15 mg/mL. **(b)** Time evolution of fluorescence emission intensity corresponding to liver, spleen, heart and femoral artery during the *in vivo* bio-distribution of Ag_2S superdots. **(c)** NIR-II ex vivo fluorescence and optical images of Liver, Spleen, Heart and Lung. Animal was sacrificed 100 min after intravenous injection of Ag_2S superdots. **(d)** Time evolution of daily food income, weight and

temperature of CD1 mice after administration of 300 µL of a solution of Ag_2S superdots in PBS (0.5 mg/mL, that leads to a total administration of 150 µg of Ag_2S superdots). Results obtained from a control group (subjected to an administration of 300 µL of PBS) are also included for comparison.

This study represents the first example of the potential of ultrafast laser pulses to improve the luminescent properties of nanostructures operating in the second biological window. In particular, the ability of ultrafast laser pulses to tune the structural and optical properties of infrared luminescent Ag_2S nanoparticles would expand their range of applications, especially in the field of nanomedicine. When one considers the advantage offered by these nanoparticles, including photo-chemical stability and optimum spectral operation range, the more than one order of magnitude improvement in their Quantum Yield demonstrate in this study should constitute the first step towards their translation into the clinics. Our discovery, the ability of ultrafast laser pulses to improve luminescent nanoparticles, may also stimulate new concepts on synthesis procedures that could benefit from the synergy between traditional chemical procedures and light-matter interaction processes.

4 Supplementary data and information section

4.1 Supplementary data and information of Ag_2S nanodots for Tumor Detection Based-Luminescence Transient Nanothermometry (LTNh)

They Ag_2S synthetized by Sinano Company (China) were surface-coated with PEG. In addition, FTIR spectrum of the Ag_2S nanodots solution evidencing the presence of PEG at dots' surface by identifying the band at around 960 cm^{-1}.

4.1.1 Ag2S nanodots characterization.

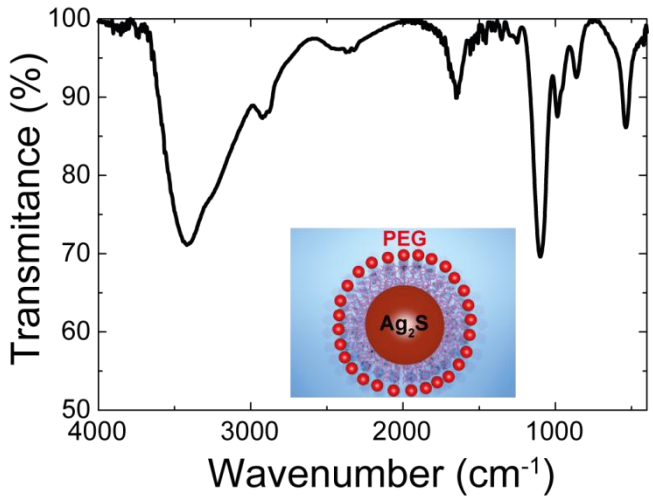

Supporting Figure 4.1. FTIR spectrum of the Ag_2S nanodots used in this work revealing the presence of PEG at its surface. The inset is an illustrative description of the Ag_2S coated with PEG.

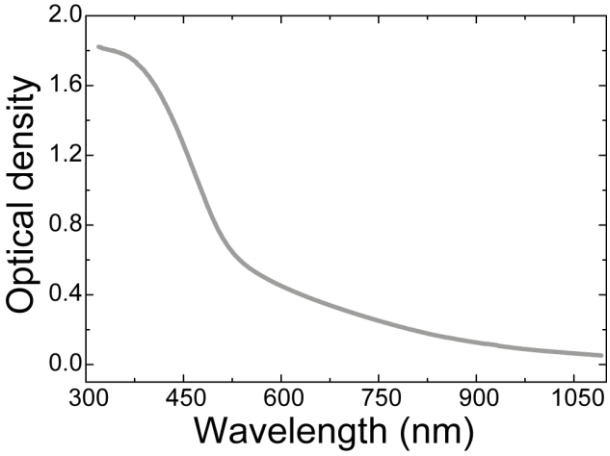

Supporting Figure 4.2. Absorption spectra of Ag_2S nanots.

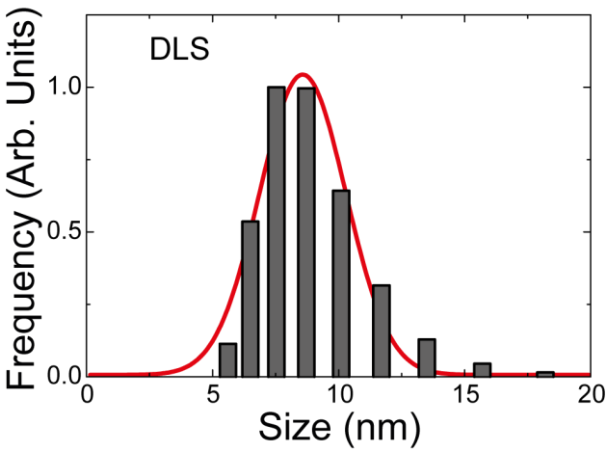

Supporting Figure 4.3. Hydrodynamic size distribution from DLS measurements of Ag_2S coated with PEG dispersed in PBS.

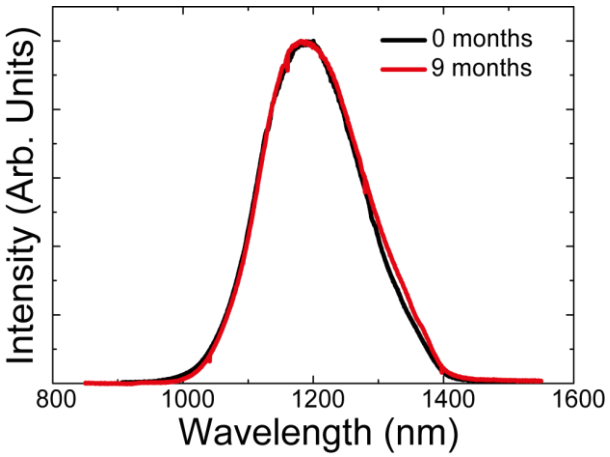

Supporting Figure 4.4. Emission spectra of a solution of Ag_2S nanodots suspended in PBS as obtained just after synthesis and 9 months later. The emission spectra are almost identical evidencing the absence of degradation.

4.1.2 Temperature dependence of Ag2S used for transient nanothermometry (TTNTh)

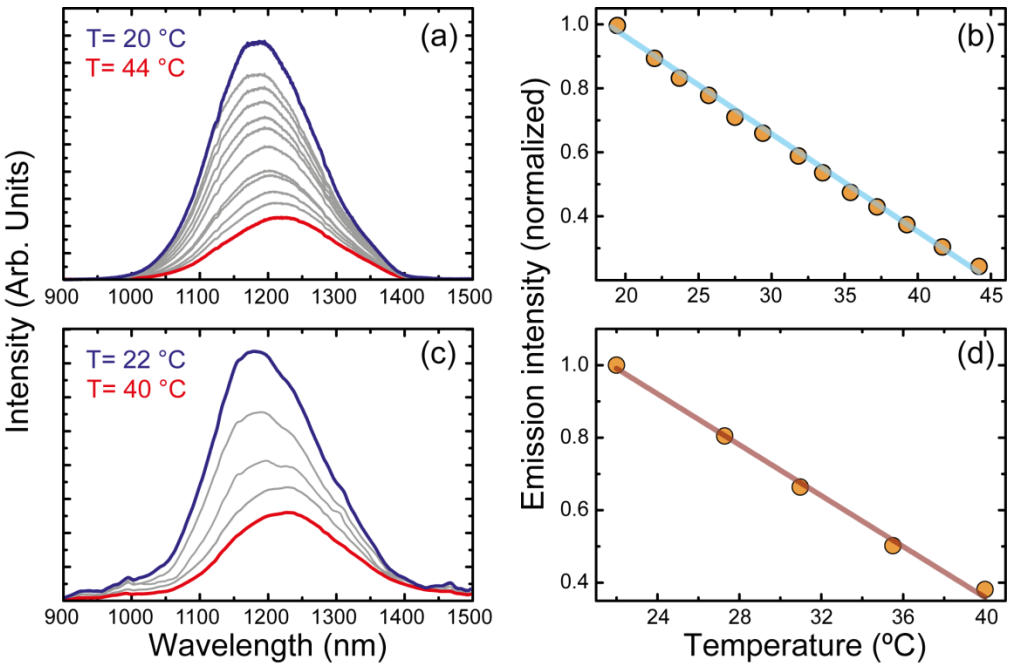

Supporting Figure 4.5. Temperature dependence of the emission spectrum generated by the Ag_2S nanothermometers **(a)** dispersed in phosphate buffer saline (PBS) and **(c)** injected into a sample of advanced-stage tumoral tissue. The tumor tissue containing the Ag_2S NCs was removed from a euthanized C57Bl/6 mouse 14 days (defined to be the characteristic tumor cycle time in our studied model) after tumor induction. The temperature dependence of integrated area under the emission curves shown in (a) and (c) is displayed in **(b)** and **(d)**, respectively.

4.1.3 Monitoring tumor progression during a 14-day cycle through transient thermometry, visual inspection, thermography and blood flow imagin

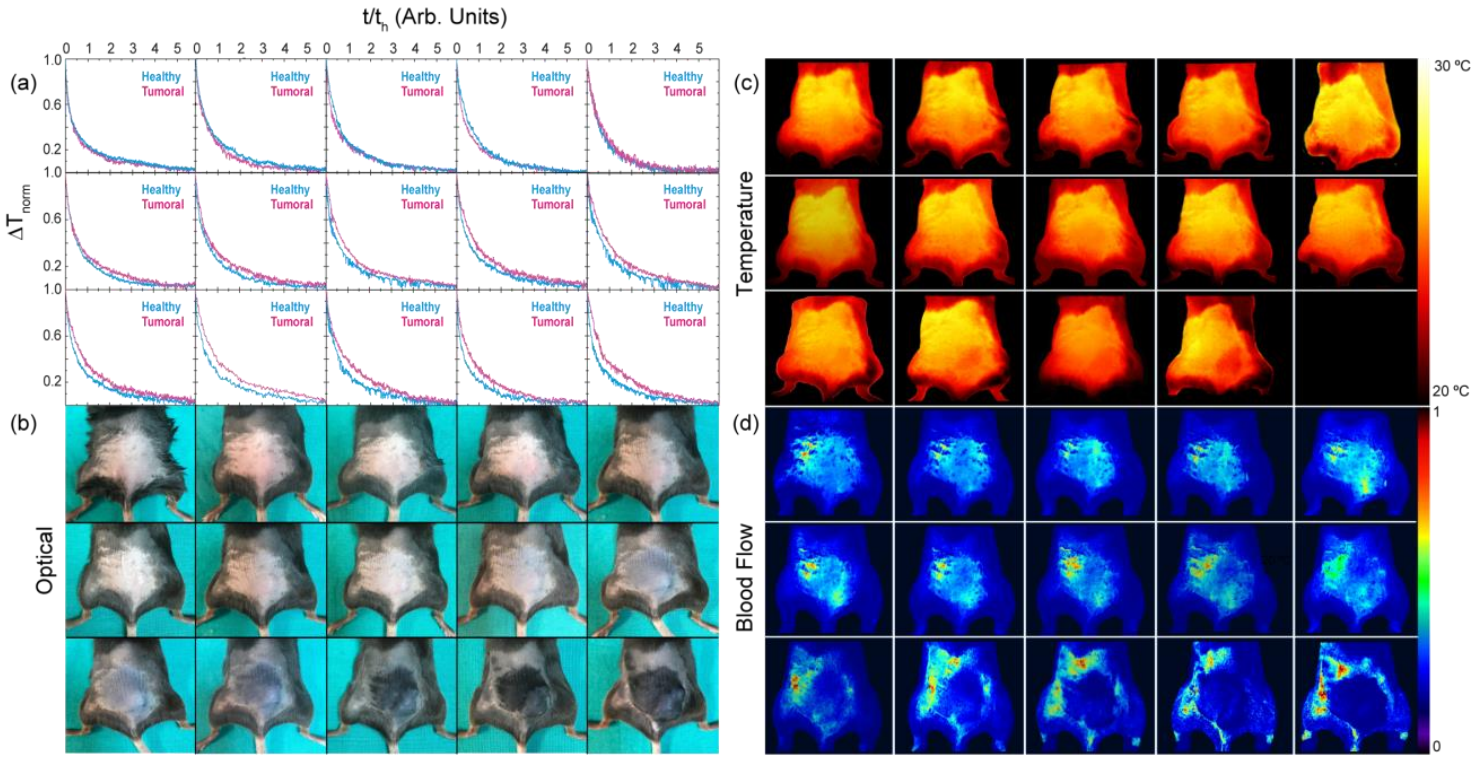

Supporting Figure 4.6. (a) Thermal transients corresponding to tumoral and healthy tissues as obtained at different times after inoculating a C57Bl/6 mouse with B16 cancer cells. **(b)** Optical images, **(c)** thermographic images and **(d)** blood perfusion images of a representative mouse as measured daily throughout tumor development. In all the inspection procedures shown in (a)-(d), the ascending order of days after cancer cells induction is from the left to right and top to bottom.

4.1.4 Analytical developing of Transient Thermometry formalism based on Pennes´ Bio-Heat equation (Laser beam as heating source)

Heat transfer in a tissue during laser irradiation is strongly affected by a variety of factors, such as the thermophysical properties of the tissue (heat capacity, density etc.), the geometry of irradiated organism, laser light absorption, metabolic heat generation, blood perfusion and other thermoregulatory mechanisms.[2] By applying the principle of energy conservation, one can balance the thermal energy in a particular control volume inside the laser-excited tissue:

$$Q_{result\ gain} = Q_{laser} + Q_{met} - Q_{loss} \quad \text{(S1)}$$

where Q_{laser} ($W \cdot m^{-3}$) is the energy gain due to light absorption by the control volume inside the tissue, Q_{met} ($W \cdot m^{-3}$) is the gain stemming from metabolic activities and Q_{loss}

($W \cdot m^{-3}$) is the energy lost through heat being conducted (or convected) away from the control volume to its surroundings (volume boundaries). For our purposes, we can neglect the boundary effects at the tissue surface as the thermal relaxation of the tissue is analyzed only through the emission of Ag_2S NCs which were injected in a specific control volume inside the tissue, thus allowing monitoring local temperature. In other words, we consider the heat conduction inside the tissue has a much more important role in the observed thermal relaxation process than the surface effects.

Based on the experimental conditions of our work, the control volume of tissue reaches a maximum temperature ($\Delta T < 7\ ^\circ C$) during the continuous incidence of the heating laser, where the temperature readout inside the control volume can be extracted through the temperature-sensitive emission of Ag_2S nanocrystals. Under those circumstances, the rate of heat gain is exactly equal to the rate of heat loss. As a consequence of this empirically observed phenomenon, the heat loss must be a function of temperature. The two main heat flow mechanisms related to energy loss inside the control volume are *Conduction* and *Convection*. Both mechanisms can be described as functions of temperature [3]. The *Conducted heat* is governed by Fourier's Law, which states that the quantity of thermal energy conducted through a medium is proportional to the cross-sectional area, the temperature difference between two points (still within the tissue) and the time elapsed and inversely proportional to the distance between the two points. Mathematically, it can be written as:

$$Q_{conduction} = -kA(\Delta T)\Delta t/\Delta L \tag{S2}$$

where *k* is the thermal conductivity ($W \cdot m^{-1} \cdot K^{-1}$).

The heat conduction flux density is defined as [3]:

$$f = \frac{Q_{conduction}}{A\Delta t} = -\frac{k\Delta T}{\Delta L} = -k\frac{\partial T}{\partial L} \tag{S3}$$

For the case of $\Delta L \approx dL$, that is an infinitesimal quantity. In 3-dimensions, the heat flux density can be written as:

$$\vec{f} = -k\vec{\nabla}T(\vec{r}, t) \tag{S4}$$

Thus, the losses due to the heat conduction can be defined as:

$$Q_{cond} = \vec{\nabla} \cdot \vec{f} = -k\nabla^2 T(\vec{r}, t) \tag{S5}$$

In *Convection* by blood flow, thermal energy is transported in and out of the control volume being studied. The net inflow can be written as:

$$Q_{convection} = \omega_b \rho_b c_b (T - T_b) \tag{S6}$$

where ω_b is the blood perfusion rate (volume of blood per unit mass of tissue per unit time), ρ_b and c_b are the density ($kg \cdot m^{-3}$) and specific heat ($J \cdot kg^{-1} \cdot K^{-1}$) of blood, and T_b is the temperature of the arterial blood. The liquid gain, $Q_{result\ gain}$, while the laser is applied, is proportional to the density, the specific heat capacity of the system (tissue + Ag_2S Qds), and the time derivative of temperature:

$$\sum_i \rho_i c_i \frac{dT}{dt} \approx \rho_t c_t \frac{dT}{dt} \tag{S7}$$

where ρ_t ($kg \cdot m^{-3}$) and c_t ($kg \cdot m^{-3}$) stand for the density and specific heat of the tissue. In this approximation, we have neglected the component $\rho_s c_s$ associated with the Ag_2S nanocrystals as their density in the control volume, ρ_s, is much smaller than ρ_t, i.e. $\rho_s \ll \rho_t$. Combining these results yields a final expression that is a special case of the well-known Pennes' bioheat equation (for the special case in which the heating source is a laser beam):[3d]

$$\rho_t c_t \frac{dT(\vec{r}, t)}{dt} = k\nabla^2 T(\vec{r}, t) - \omega_b \rho_b c_b \big(T(\vec{r}, t) - T_b(\vec{r})\big) + Q_{met}(\vec{r}, t) + Q_{laser}(\vec{r}, t) \tag{S8}$$

As previously stated, after subjecting the tissue control volume to a continuous incidence of a heating laser, the tissue reaches a maximum temperature, i.e., the net energy gain is equal to zero, mathematically described as:

$$\frac{dT(\vec{r}, t)}{dt} \approx 0 \tag{S9}$$

At this very moment, herein defined as $t = 0$, the heating laser is switched off ($Q_{laser}(\vec{r}, t = 0) = 0$). From expression (S8), this results in:

$$0 \approx k|\nabla^2 T(\vec{r}, t=0)|_{T=Tmax} - \omega_b \rho_b c_b \left(T_{max}(\vec{r}, t=0) - T_b(\vec{r})\right) + Q_{met}(\vec{r}, t=0)$$

$$\therefore Q_{met}(\vec{r}, t=0) \approx -k|\nabla^2 T(\vec{r}, t)|_{T=Tmax} + \omega_b \rho_b c_b \left(T_{max}(\vec{r}, t=0) - T_b(\vec{r})\right) \quad \text{(S10)}$$

Equation (S10) indicates a temperature dependence of metabolic activity. In fact, an exponential trend has been reported within the relevant biological range (0-40 °C).[4] However, for a small temperature increment ($|\Delta T| < 7$ °C), we can consider the metabolic activity, in a first order approximation, as a linear function of the temperature increment, i.e.:

$$Q_{met}(\vec{r}, t) = \alpha\left(T(\vec{r}, t) - T_{basal}(\vec{r})\right) + Q_{basal}(\vec{r}) \quad \text{(S11)}$$

where $T_{basal}(\vec{r})$ is the basal temperature of the tissue control volume before being subjected to a heating stimulus. The constant α depends on the average activation energy, E, which reflects the kinetics of enzyme-catalyzed biochemical metabolic reactions [4b, 5]. These enzyme-catalyzed reactions, in turn, provide energy to the organisms which will then use it not only for growing and reproducing but also for maintaining their structures and for responding to modifications induced on their surroundings, such as temperature changes.[6] $Q_{basal}(\vec{r})$ is the metabolic heat production before the heating stimuli.

Henceforth, we must clearly define the three different time regimes in our experiment:

- The period before the laser was switched on:

$$t \to -\infty \quad \text{(S12.1)}$$

- The period during which the laser continuously heated the tissue:

$$-\infty < t < 0 \quad \text{(S12.2)}$$

- The period after the laser was switched off (cooling stage):

$$t > 0 \tag{S12.3}$$

Equation (S8) states that (for $t > 0$):

$$\rho_t c_t \frac{dT(\vec{r},t)}{dt} = k\,\nabla^2 T(\vec{r},t) - \omega_b \rho_b c_b (T(\vec{r},t) - T_b) + Q_{met}(\vec{r},t) \tag{S13.1}$$

Defining the temperature increment as $\Delta T(\vec{r},t) = \left(T(\vec{r},t) - T_{bassal}(\vec{r})\right)$ and since we know that $Q_{met}(\vec{r},t) = \alpha \Delta T(\vec{r},t) + Q_{basal}(\vec{r})$, then Equation (S13.1) becomes:

$$\begin{aligned}
\rho_t c_t \frac{d[\Delta T(\vec{r},t) + T_{basal}(\vec{r})]}{dt} = \rho_t c_t \frac{d[\Delta T(\vec{r},t)]}{dt} = \\
k\,\nabla^2[\Delta T(\vec{r},t) + T_{basal}(\vec{r})] - \omega_b \rho_b c_b (\Delta T(\vec{r},t) + T_{basal}(\vec{r}) - T_b) \\
+ \alpha \Delta T(\vec{r},t) + Q_{basal}(\vec{r}) = \\
k\,\nabla^2[\Delta T(\vec{r},t)] + (\alpha - \omega_b \rho_b c_b)\Delta T(\vec{r},t) + \\
+\{ k\,\nabla^2[T_{basal}(\vec{r})] - \omega_b \rho_b c_b (T_{basal}(\vec{r}) - T_b) + Q_{basal}(\vec{r})\}
\end{aligned} \tag{S13.2}$$

Now, we state that the term inside the curly brackets vanishes. To demonstrate this, we indicate that, for our purposes, $\lim_{t\to-\infty} T(\vec{r},t) = T_{basal}(\vec{r})$ which, in turns, implies the following:

$$\begin{aligned}
\lim_{t\to-\infty} \Delta T(\vec{r},t) = \lim_{t\to-\infty} [T(\vec{r},t) - T_{basal}] = 0 \\
\lim_{t\to-\infty} Q_{met}(\vec{r},t) = \lim_{t\to-\infty} [\alpha\, \Delta T(\vec{r},t) + Q_{basal}(\vec{r})] = Q_{basal}(\vec{r})
\end{aligned} \tag{S13.3}$$

With those relations in mind, we can calculate the same limit for Equation (13.2):

$$\begin{aligned}
\lim_{t\to-\infty} \left[\rho_t c_t \frac{dT(\vec{r},t)}{dt}\right] = \lim_{t\to-\infty} [k\,\nabla^2 T(\vec{r},t) - \omega_b \rho_b c_b (T(\vec{r},t) - T_b) + Q_{met}] = \\
= k\nabla^2 \left\{\lim_{t\to-\infty} [T(\vec{r},t)]\right\} - \omega_b \rho_b c_b \left\{\lim_{t\to-\infty} [T(\vec{r},t)] - T_b\right\} + \lim_{t\to-\infty} [Q_{met}(\vec{r},t)] \\
= \\
k\,\nabla^2 T_{basal}(\vec{r}) - \omega_b \rho_b c_b (T_{basal}(\vec{r}) - T_b) + Q_{basal}(\vec{r},t) \\
\therefore \rho_t c_t \lim_{t\to-\infty} \left[\frac{dT(\vec{r},t)}{dt}\right] \\
= k\,\nabla^2 T_{basal}(\vec{r}) - \omega_b \rho_b c_b (T_{basal}(\vec{r}) - T_b) + Q_{basal}(\vec{r},t)
\end{aligned} \tag{S13.4}$$

Now, if we make the reasonable assumption that before the laser was switched on, the temporal fluctuations of temperature were close to zero, i.e., $\lim_{t\to-\infty}\left[\frac{dT(\vec{r},t)}{dt}\right]=0$, then equation S13.4 results in:

$$k\,\nabla^2 T_{basal}(\vec{r}) - \omega_b\rho_b c_b(T_{basal}(\vec{r}) - T_b) + Q_{basal}(\vec{r},t) = 0 \qquad \text{(S13.5)}$$

Thus, the expression S13.2 is summarized as (for $t > 0$):

$$\rho_t c_t \frac{d[\Delta T(\vec{r},t)]}{dt} = k\,\nabla^2[\Delta T(\vec{r},t)] + (\alpha - \omega_b\rho_b c_b)\Delta T(\vec{r},t) \qquad \text{(S14)}$$

The time interval characterized by $t > 0$ is defined as the cooling stage, during which the thermal relaxation was monitored in our experiments. The simple form of equation S14 suggests that the method of separation of variables can be applied and helps us derive an analytic solution for the bioheat equation. Thus, if we assume a solution in a product form:

$$\Delta T(\vec{r},t) = G(\vec{r}) * F(t) \qquad \text{(S15)}$$

For quantifying the temporal evolution of the bioheat equation after switching off the laser, we can spatially integrate equation S14 inside the control volume of interest. The result of this operation is:

$$B_1\rho_t c_t \frac{dF(t)}{dt} = kB_2F(t) - \omega_b\rho_b c_b B_1 F(t) + B_1\alpha F(t) \qquad \text{(S16)}$$

Where B_1 and B_2 are constants that depend on the dimensions of both the investigated tissue and the spot of the heating laser, defined as:

$$B_1 = \int G(\vec{r})dV \;\; and \;\; B_2 = \int \nabla^2 G(\vec{r})dV = \oint \vec{\nabla}G(\vec{r})\cdot d\vec{S} \qquad \text{(S17)}$$

If we now integrate equation S16 with respect to time (t) from 0 to t', it results in:

$$F(t') \approx e^{-\frac{(\omega_b\rho_b c_b - (B_2/B_1)k - \alpha)t'}{\rho_t c_t}} = e^{-t'/\tau} \qquad \text{(S18)}$$

where τ is defined as a first order approximation of the thermal characteristic relaxation time of the tissue control volume. In our experiments, this can be well monitored through temperature-induced emission intensity changes of the Ag_2S nanothermometers injected within the tissue. Blood and tissue properties, metabolic activity, heat conductivity and the geometry of the irradiated tissue all play an important role in the thermal response of the tissue:

$$\tau = \frac{\rho_t c_t}{\omega_b \rho_b c_b + Ck - \alpha} \tag{S19}$$

where $C = -B_2/B_1 = \oint \vec{\nabla} G(\vec{r}) \cdot d\vec{S} \,/ \int G(\vec{r}) dV$. At this point, it is worth noting that *C* is a positive constante.

To demonstrate this, let us remind *that* $\Delta T(\vec{r}, t) = G(\vec{r}) * F(t) \geq 0$ for all $(\vec{r}, t)$. As $F(t') > 0$ at any time t (see expression (S16)), then $G(\vec{r}) > 0$ everywhere. *Also, let's assume* $\vec{r} = r\hat{r}$ points away from the center of the studied volume.

The previous conditions imply:

$$B_1 = \int G(\vec{r}) dV > 0 \tag{S20.1}$$

Furthermore, $\vec{\nabla}\Delta T(\vec{r}, t) = F(t) * \vec{\nabla} G(\vec{r})$ points in the direction of greatest rate of increase of $\Delta T(\vec{r}, t)$, which in our case is towards the center of the control volume (the temperature distribution, during and after applying the heating laser, exhibits its maximum at the center of the control volume.), i.e, $\vec{\nabla} G(\vec{r})$ is parallel to -$\hat{r}$. On the other side, $d\vec{S}$ = $dS\hat{r}$, pointing away from the center. Thus:

$$B_2 = \int \vec{\nabla} G(\vec{r}) \cdot d\vec{S} = -\int \frac{\partial G(\vec{r})}{\partial r} dS < 0 \tag{S20.2}$$

And

$$C = \frac{-B_2}{B_1} > 0 \tag{S20.3}$$

A careful review of this topic shows that the relaxation time found in expression S19 is in full agreement with those found in the literature,[7] except for the additional constant

in the denominator in S19, α, which is associated with the metabolic activity, as shown in:

$$\tau = \frac{\rho_t c_t}{\omega_b \rho_b c_b + \frac{\mu^2}{L^2} k} = \frac{L^2}{\beta_{eff}} \quad \text{(S21)}$$

Where $\beta_{eff} = (\omega_b \rho_b c_b L^2 + \mu^2 k)/4\rho_t c_t$ describes the effective thermal diffusivity of the tissue, μ is an eigenvalue (dimensionless) and L is the characteristic linear dimension of the tissue volume being heated.

By comparing the expressions S19 and S21, C can be identified as:

$$C = B_2/B_1 = \int \nabla^2 G(\vec{r}) dV) / \int G(\vec{r}) dV = \frac{\mu^2}{L^2} \quad \text{(S22)}$$

Note that the definition of C makes the stated equality dimensionally possible since $\int \nabla^2 G(\vec{r}) dV) / \int G(\vec{r}) dV$ has a dimension of [1/m^2].

Additionally, for the excitation wavelengths in the visible/NIR spectral regions, it has been proposed that L can be assumed to be equal to the spot radius of the laser.[8] This assumption seems to be well-grounded since the dimensions of the irradiated tissue control volume are limited by the laser spot size.

In order to check the validity of our analytical solution, we estimated the characteristic relaxation time of a healthy tissue using numerical data provided by literature. Since the Ag_2S nanothermometers were injected between the epidermis and muscle layers, the tissue properties of our interest are confined to these zones (see Table S1 below).

	$\boldsymbol{k}$ $(\mathbf{W \cdot K^{-1} m^{-1}})$	$\boldsymbol{\rho}(\mathbf{kg \cdot m^{-3}})$	$\boldsymbol{c}(\mathbf{J \cdot K^{-1}\, m^{-3}})$	$\boldsymbol{\omega}(\mathbf{s^{-1}})$
Tissue[7, 9]	0.445	1116	3300	No
Blood[7, 9a]	No	1055	3660	$3 \cdot 10^{-3}$

Supporting Table 4.1. Values physical and thermodynamic properties of tissue and blood of a living organism.

From the data provided in Table S1 and using the value of C for the laser's spot radius used in our experimental procedure (herein assumed to be ~0.5 cm), the terms associated with blood perfusion and heat conductivity, as well as $\rho_t c_t$ are:

$$\rho_b c_b \omega_b \approx 1.8 \cdot 10^4 \frac{W}{K \cdot \mathrm{m}^3}$$
$$Ck \approx 1.2 \cdot 10^4 \frac{W}{K \cdot \mathrm{m}^3}$$
$$\rho_t c_t = \approx 3.7 \cdot 10^6 \frac{J}{K \cdot \mathrm{m}^3} \quad \text{(S23)}$$

Further, the metabolic activity of some biological systems has been shown to present a linear behavior with temperature within the physiological range (20-40 °C) for a factor of 2 in a range of temperature increment of 5-10 °C [4a, 4d, 10]. Working under these assumptions and by using the reported value of 368 mW.m^{-3} for Q_{basal} at T = 32.8 ^{o}C,[9c, 11] we can obtain from equation (S11):

$$\alpha = \frac{(2Q_{bassal} - Q_{bassal})}{(\Delta T)} = [\text{from 37 to 72}]\ \mathrm{W \cdot K^{-1} m^{-3}} \quad \text{(S24)}$$

Substituting the values into the equation (S19), it results in a thermal relaxation time of $\tau \approx 123$ s. This value is in a good agreement with our experimental results (60-100 s).

The small value for the term associated with the metabolic activity ($\alpha \approx 7 \cdot 10^1 \frac{W}{K \cdot \mathrm{m}^3}$) makes it negligible when compared to those related to blood perfusion ($\rho_b c_b \omega_b \approx 1.78 \cdot 10^4 \frac{W}{K \cdot \mathrm{m}^3}$) and thermal conductivity ($Ck \approx 1.2 \cdot 10^4 \frac{W}{K \cdot \mathrm{m}^3}$). On the other hand, compared to healthy tissues, tumor tissues have an almost identical thermal conductivity k ($0.55 \frac{W}{K \cdot \mathrm{m}}$).[9a] Despite the discrepancies in literature about the behavior of tumor metabolic activity,[9a, 12] their value does not change by more than a factor of 10 (depending on the type and the stage of the tumor), thus remaining negligible for tumor tissues. The small contribution of the metabolic activity term for both healthy and tumor tissue allows us to simplify the expression for thermal relaxation time even further, so that:

$$\tau \approx \frac{\rho_t c_t}{\omega_b \rho_b c_b + Ck} \tag{S25}$$

Bear in mind that Ck is almost the same for both healthy and tumoral tissues, so the blood perfusion plays a crucial role in the difference between the thermal relaxations of healthy and tumor tissue. Indeed, an increasing number of studies have found that tumor tissues present a low blood perfusion in respect to a normal tissue, showing that thermal response difference between tumors and healthy tissue arises as a consequence of the perfusion rate variance [12-13]. However, during the *angiogenesis* process, when tumor growth stimulates the development of new blood vessels (tumor's capillaries), both metabolic activity and blood perfusion are predicted to be higher than those of a healthy tissue and a tumoral one in a more advanced stage. For this case, instead of the solution in equation S25, the complete solution shown in equation S19 should be taken into account.

4.1.1 Numerical simulations approach.

In order to test the former experimental evidences on the influence of blood perfusion in the thermal relaxation of tumors, we have performed numerical simulations in a realistic computer mouse model using a transient solver that employs the finite-difference time-domain (FDTD) method, which allows a better local resolution of the calculations. A thermoregulation model based on the aforementioned Pennes bioheat equation is used,[3d] with a lumped term that includes $\boldsymbol{\omega_b}$, $\boldsymbol{\rho_b}$, $\boldsymbol{c_b}$ and $\boldsymbol{T_b}$, accounting for the *heat transfer rate*, i.e. the heat carried away by blood perfusion.

Blood perfusion varies with temperature, as other tissue properties do. This dependence may be included in the physical model of the thermal exchange between the tumor and its surroundings during tissue cooling to better account for the role of perfusion during a thermal therapy treatment. Nevertheless, depending on the conditions this approach may complicate calculations unnecessarily, even leading to under- or overestimating the actual values. It has been shown that the temperature dependence of perfusion should only be explicitly considered in the model just when the temperature difference goes above 10 ºC.[14] Since the temperature difference in the present case is closer to 10 ºC, two different models of blood perfusion during thermal relaxation have been considered for the sake of comparison: *constant* (temperature independent) and *piecewise linear* (temperature dependent) models. The constant model assumes a continuous, laminar-like blood supply, while the piecewise linear one considers different perfusion regimes depending on the considered temperature ranges. As pre-defined in the experimental conditions used in our study, we define the following piecewise linear model for the temperature tumor blood perfusion (ω_{tv}):

$$\omega_{tv} = \begin{cases} 50\ l/kg/min, & T > 44\ ºC \\ 10 l/kg/min\big(1 + 0.8(T - 39\ ºC)\big), & 44\ ºC > T \geq 39\ ºC \\ 10\ l/kg/min, & T < 39\ ºC \end{cases} \qquad \text{(S26)}$$

In the case of the constant model, the corresponding blood perfusion value has been directly inserted in the thermal solver for the entire temperature range. The system has been evaluated for each tissue taking into account the corresponding tissue physical properties (Table S2). In addition, only the voxels with a value within a narrow band defined by some pre-defined limits around transition temperatures are tested after each iteraction and reassigned to other segments of the temperature dependence, as described.[14] The width of the band considered here is 0.5 ºC above and below the corresponding temperature limits.

Tissue	$\boldsymbol{\rho}$ $(\boldsymbol{kg/m^3})$	$\boldsymbol{c_t}$ $(\boldsymbol{J/kg/K})$	$\boldsymbol{k}$ $(\boldsymbol{W/m/K})$	$\boldsymbol{q_t}$ $(\boldsymbol{W/m^3/K})$	$\boldsymbol{Q}$ $(\boldsymbol{W/kg})$	$\boldsymbol{\omega_t}$ $(\boldsymbol{ml/kg/min})$
Fat	911	2348.33	0.21	2013	0.51	32.71
Skin	1109	3390.5	0.37	7969	1.65	106.38
Skin (with fur)	1109	3390.5	0.04	7969	1.65	106.38
Melanoma[15]	1060	3852	0.56	3680	3.47	356.6
Blood	1049.75	3617	0.52	709090	0	10000

Supporting Table 4.2.-Relevant physical parameters of the tissues present in the thermal simulations with indication of the corresponding source.[16]

The numerical simulations were carried out using the *Diggy* model—a high-resolution male nude normal mice model—available through the IT'IS FOUNDATION (http://dx.doi.org/ 10.13099/VIP91205-01-0) as part of the Virtual Family computational models.[17] In order to mimic the in vivo setup as much as possible, the posture of the mouse virtual model has been adapted using a physics-based poser engine included in the Sim4Life platform.[18] A tumor phantom was inserted in the mouse model at the same implantation place chosen for the in vivo studies (Figure 6a). All the simulations were carried out considering the most advanced stage of tumor growth. Since growing tumors usually tend to develop a highly perfused shell with a necrotic core,[19] which matches our histopathological findings, the microcirculation of the tumor

has been studied by generating a virtual model with predominant peripheral vascularization, with most of the vessels running parallel to the tumor surface.

Branching and vessel size were chosen so as to follow a random distribution. In regions with high chances of overlapping tissues, a higher priority was given to those more relevant to the thermal relaxation of the studied region; for example, the tumor and its vasculature were given a higher priority prior compared to their surroundings. Prioritization determined the most relevant physical properties in the case of tissue overlapping, so those of the tumor and its vessels overwrote the properties of fat, bones and muscles. The skin interface was assigned mixed (convective) boundary conditions, so that the heat flux across the surface satisfies:

$$F_{boundary} = k\frac{dT}{dn} + h(T - T_{outside}) \quad \text{(S27)}$$

Where k is the thermal conductivity, h is the heat transfer coefficient, and (T-$T_{outside}$) the local temperature difference. For hollow organs, Neumann boundary conditions with a 0 $W \cdot m^{-2}$ heat flux across boundaries have been chosen:

$$F_{boundary} = k\frac{dT}{dn} \quad \text{(S28)}$$

Although both deliver relatively close results, the piecewise linear model underperforms specially within the 15–150 s time range, where the perfusion weight is slightly overestimated.

\

4.2 Supplementary data and information of Ag_2S Dot-to-Superdot transformation triggered by femtosecond laser pulses

4.2.1 Characterization of the side products of ultrafast laser irradiated Ag2S dots.

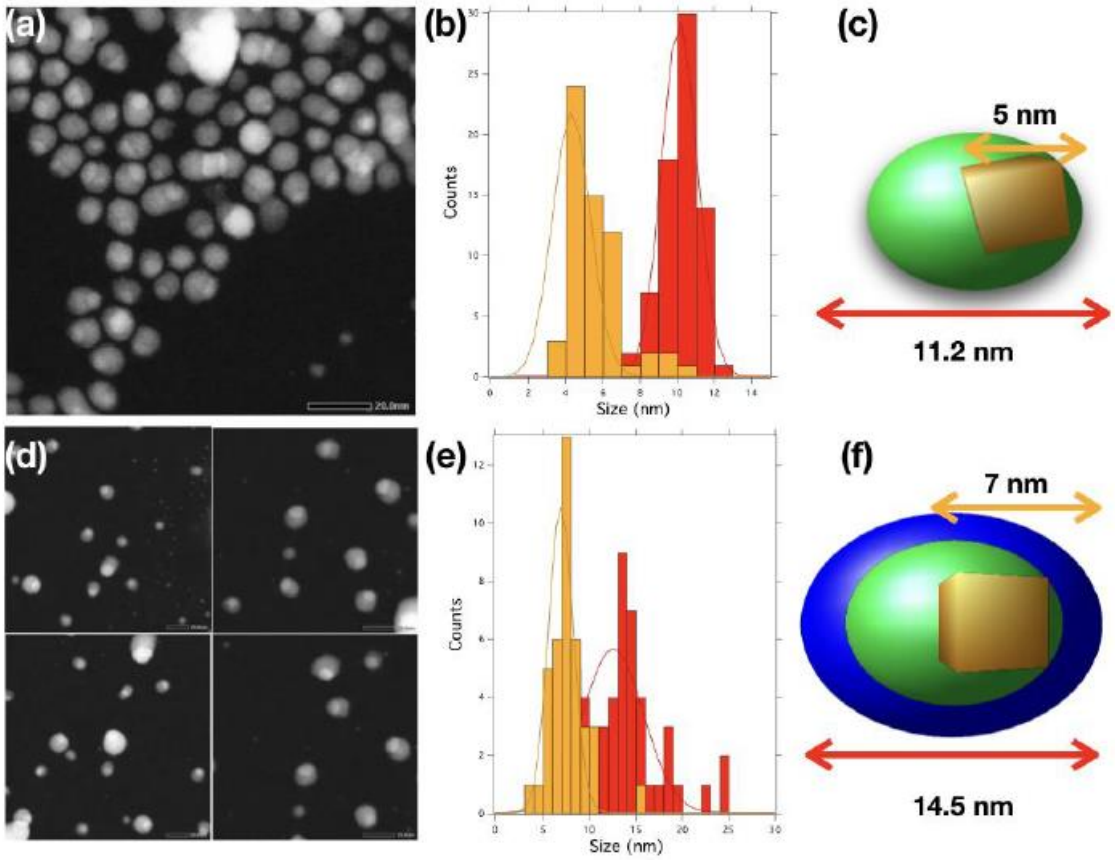

Supporting Figure 4.7. (a) HAADF-STEM image of Ag2S dots. **(b)** Size distribution of Ag2S dots as obtained from the STEM image. c) Schematic representation of the structure of Ag2S dots, including the sizes. **(d)** HAADF-STEM images of Ag/Ag2S@AgCl superdots (hereafter, Ag2S superdots) **(e)** Size distribution of the Ag2S superdots as obtained from the STEM images. Orange and red bars correspond to Ag core and Ag2S, respectively. **(f)** Schematic representation of the structure of Ag2S superdots, including the sizes.

4.2.2 Optical transformation of Ag_2S dot-to-superdot transformation induced by femtosecond laser irradiation

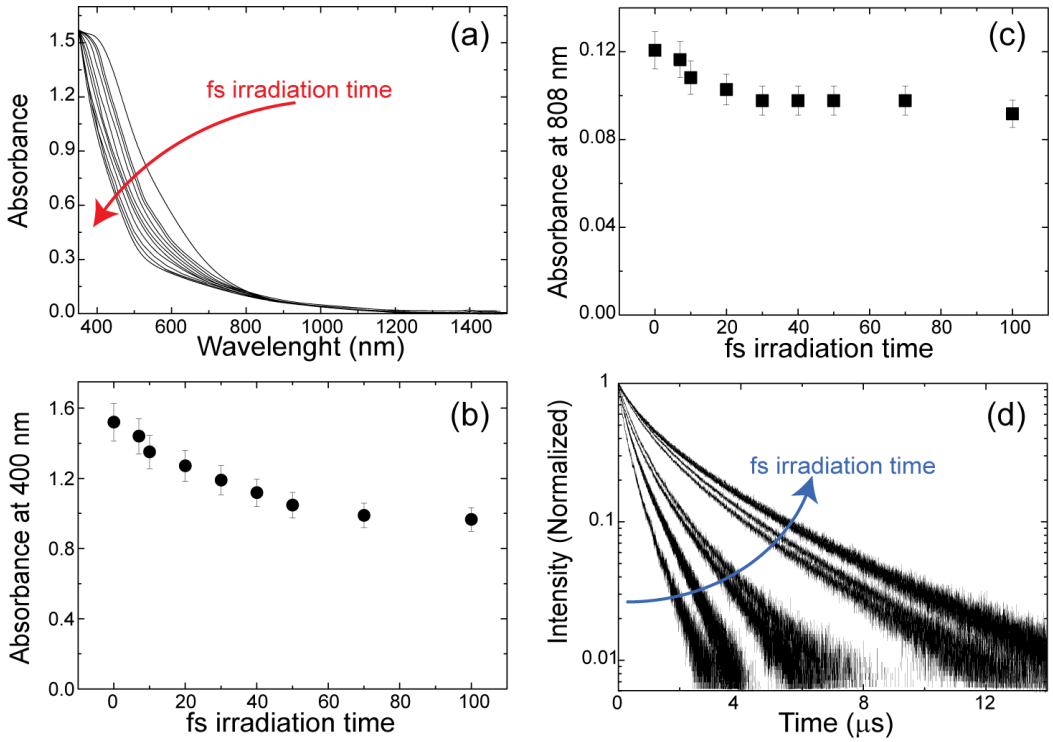

Supporting Figure 4.8. (a) VIS-NIR extinction spectra of colloidal solutions of Ag/Ag_2S dots in $CHCl_3$ as treated with ultrafast laser during different times. **(b)** Extinction coefficient at 400 nm as a function of treatment time for the VIS-NIR extinction spectra curves presented (a). **(c)** Extinction coefficient at 808 nm as a function of treatment time for the VIS-NIR extinction spectra curves presented (a). **(d)** Fluorescence decay curves of colloidal solutions of Ag/Ag_2S dots in $CHCl_3$ as treated with ultrafast laser during different times. In all cases, the solutions as treated with a ultrafast laser keeping the same pulse width, power and laser density (50 fs, 0.6 W and 9 W/cm^2).

4.2.2.1 No presence of concentration artifacts

Data concerning concentration dependence of lifetime are display in **Supporting Fig. 4.9**. We dissolved the solution from 1 down to 0.1 mg/ml in order to monitor if there are any presence of artifacts related to high concentration of Ag_2S Superdots in $CHCl_3$. No evidence of concentration artifacts were found, demonstrating that the long lifetime of Ag_2S Superdots is indeed provided by minimizing non-radiative pathways, as the ultrafast laser treatment is applied.

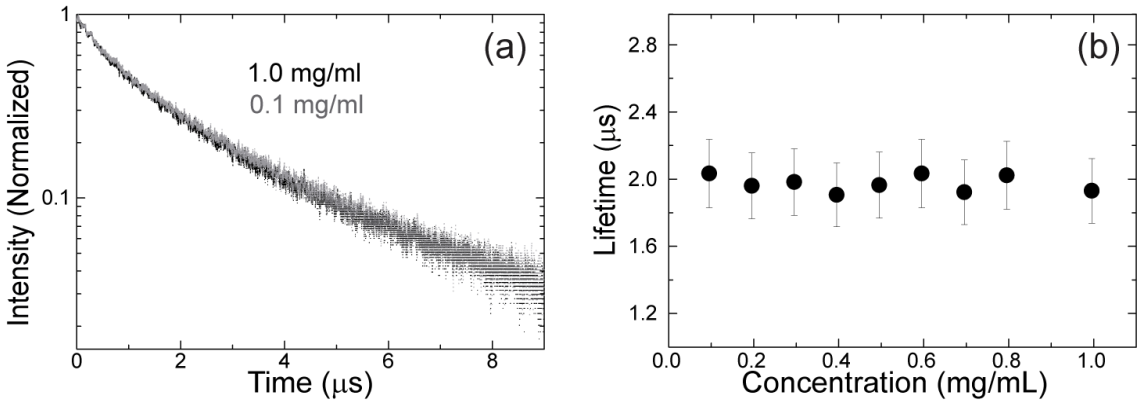

Supporting Figure 4.9. (a) Fluorescence decay curves from colloidal solutions of Ag@Ag_2S dots in $CHCl_3$ as treated with ultrafast laser (50 fs, 0.6 W and 9 W/cm^2) during 90 min at concentration of 1.0 and 0.1 mg/mL. **(b)** Lifetime as a function of concentration of the treated solution of Ag@Ag_2S dots based on fluorescence decay curves given in (a).

4.2.3 Multiphoton character of the Ag2S dot-to-superdot transformation.

The multiphoton character of the ultrafast laser induced dot-to-superdot transformation is investigated by measuring the intensity enhancement rate (*dI/dt*) obtained during irradiation with different pulse energies. In this case, the beam spot size is kept constant for the different pulse energies. Experimental results are included in **Supporting Fig. 4.10** and clearly show a linear trend in a Log-Log representation with a slope of 2.2 indicates that the dot-to-superdot transformation is triggered by a two photon absorption process.

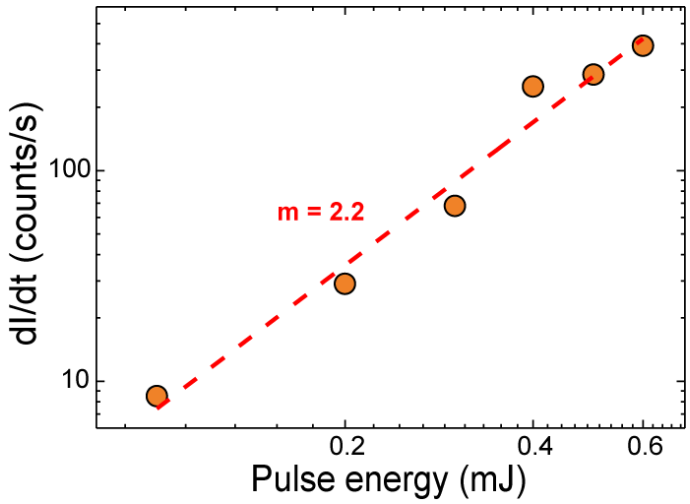

Supporting Figure 4.10.. The time derivative of intensity as a function of irradiation pulse energy (E_p). The slope of the curve that (η) shows to be directly proportional to E_p^2.

4.2.4 Optimum laser conditions for Ag2S dot-to-superdot transformation

The **Supporting Fig. 4.11** demonstrates that when the irradiation power density is larger than 9 W/cm^2 the initial improvement is followed by luminescence deterioration. Indeed, for irradiation pump densities as high as 40 W/cm^2 the luminescence is completely quenched after 30 min of irradiation. This complete fluorescence quenching is accompanied by a drastic change in the color of the sample as it can be observed in **Supporting Fig. 4.11a**. We state that for such large power densities the Ag_2S nanodots have been completed destroyed and the solution just contain AgCl. The final fluorescence intensity is consequence of the interplay between the increasing improving rate with the power density and the excessive damage caused at high excitation densities. **Supporting Fig. 4.11b** shows the luminescence intensity generated by the solution of Ag_2S dots as a function of the irradiation power density. Note that in each case the final luminescence intensity has been normalized by the excitation density. The results clearly reveal the existence of an optimum irradiation density close to 9 W/cm^2. Power densities below this value do not cause a complete transformation of Ag_2S QDs whereas larger power densities induce irreversible damage.

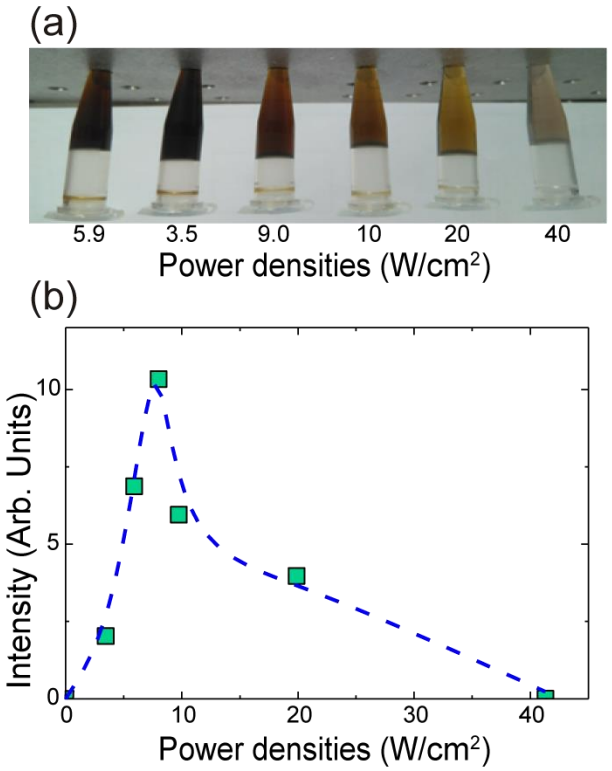

Supporting Figure 4.11. (a) Optical images for the solution of Ag_2S treated with different power densities during the ultrafast laser treatment. **(b)** Luminescence intensity generated by the solution of Ag_2S dots at the final of the ultrafast irradiation treatment (around 100 min) as a function of the irradiation power density. The optimum irradiation density was found to be close to 9 W/cm^2.

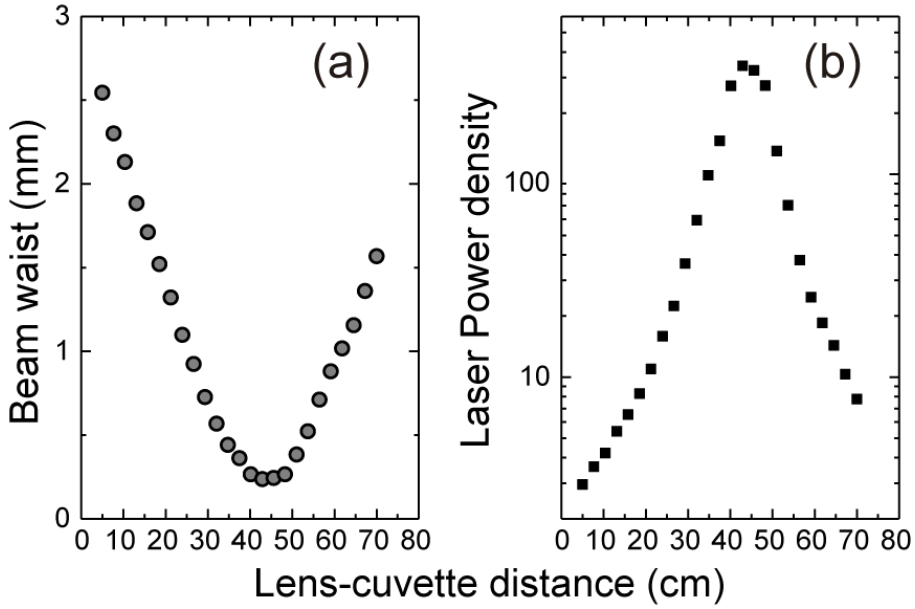

Supporting Figure 4.12. (a) Variation of the beam waist of the femtosecond laser pulse as a function of the lens-to-cuvette distance. **(b)** Variation of the power density of the femtosecond laser as a function of the lents-to-cuvette distance. The average laser power of the ultrafast irradiating laser was set to 0.6 W.

4.2.5 Thermal induced quenching during ultrafast laser irradiation

In order to study the thermal loading effect during the treatment based on ultrafast laser irradiation, a thermocouple was placed inside of the cuvette containing the colloidal solution of Ag/Ag_2S dots in $CHCl_3$. In this case the laser was set up at 50 fs and 15 W/cm^2. As can be observed in the **Supporting Fig. 4.13a,** the solution of as-prepared $Ag@Ag_2S$ dots changes its temperature as the times goes by during the laser treatment. The more prominent temperature increment happened during at the first 10 minutes, reaching a maximum value close to 15 °C. For times longer than 10 min the temperature starts to going down until it reaches a steady value close to 10 °C. The same experiment was also performed in an already treated solution (Ag/Ag_2S@AgCl Superdots treated during 90 min using an ultrafast laser of 50 fs and 9 W/Cm^2), that is, the already superdot structure was subjected to a second ultrafast laser treatment with a power density of 15 W/cm^2. In this last case, the superdot structure has showed a maximum temperature increment of only 10 °C during the first 10 min, but in contrast to the as-prepared solution, no remarkable changes could be observed for times longer than 10 min, in which it remained in an almost constant temperature increment of 10 °C. Interestingly, we can see that both, treated (superdot) and untreated (dot) solutions have reached the same temperature increment for times longer than 10 min, it can be explained by the fact that the during the laser treatment the untreated solution is changing its structure from *dot* to *Superdot* while the already treated solution does not show any remarkable changes in its structure, and, at the final, both solutions are founding to present the Ag/Ag_2S@AgCl Superdots heterostructure. Indeed, the NIR-II fluorescence image of both solutions after applying the laser treatment for long times of 60 min are showed as an inset in the **Supporting Fig. 4.13a**, clearly showing that the fluorescence intensity is almost the same, being only a little bit lower for the already treated solution (subjected to a double-ultrafast laser treatment). This is expected since the second-hand treatment on the already treated solution only promotes thermal loading effect and damage induced by ultrafast laser pulses. The difference in the temperature increment at the first 10 min when a comparison is made between the as-prepared (15 °C) and treated solution (10°C) is due to the fact that the as-prepared solution has found to present more non-radiative pathways associated with photothermal conversion than the treated solution. This result is also reflected in the Quantum Yield, where the as-prepared Ag_2S dot shows to present a lower QY than the

Ag_2S superdot (50-fold lower). However, once the ultrafast laser transformation of dot-to-superdot is applied, the increase of the QY accompanied by the reduction of the fractional thermal loading is evident.

The time evolution of emitted intensity generated from both solutions studied above (as-prepared and treated solution) has also been investigated by applying the same conditions of laser**.** Similar to the behavior observed in **Supporting Fig. 4.13a** concerning the thermal loading effect, the luminescence intensity for as-prepared solution also changed mainly during the first 10 min and is showed to keep a steady maximum value for longer times as described in **Supporting Fig. 4.13b**. Such results provide further evidence and strengthen to the previous conclusions. Indeed, the assumption that the complete transformation from *dot-to-superdot* occurs in the first 10 min of irradiation is also checked through the emitted light intensity. The course of the time evolution of emitted intensity of the already treated solution was also investigated (see **Supporting Fig. 4.13b)**. For this case, the emitted intensity showed a rapid substantial decrement during the first 10 min, shortly afterward, showing to decrease slowly. These results show to corroborate to the luminescence quenching effect behavior induced by temperature previously described in **Supporting Fig. 4.13a** as well to the presence of laser induced damage effect. Indeed, by looking at the emission spectra as a function of temperature displayed in **Supporting Fig. 4.13c** and the temperature dependence of its emitted intensity in **Supporting Fig. 4.13d**, the changed was found to be closed 4% per °C. Based on the fact that the treated solution showed to present a maximum temperature increment of 10°C, the thermal quenching is calculated to be 40%. However, the experimentally observed quenching was found to be close of 50%, demonstrating that although the majority contribution are associated with temperature increment, a small but significant part due to the laser induced damage is also present

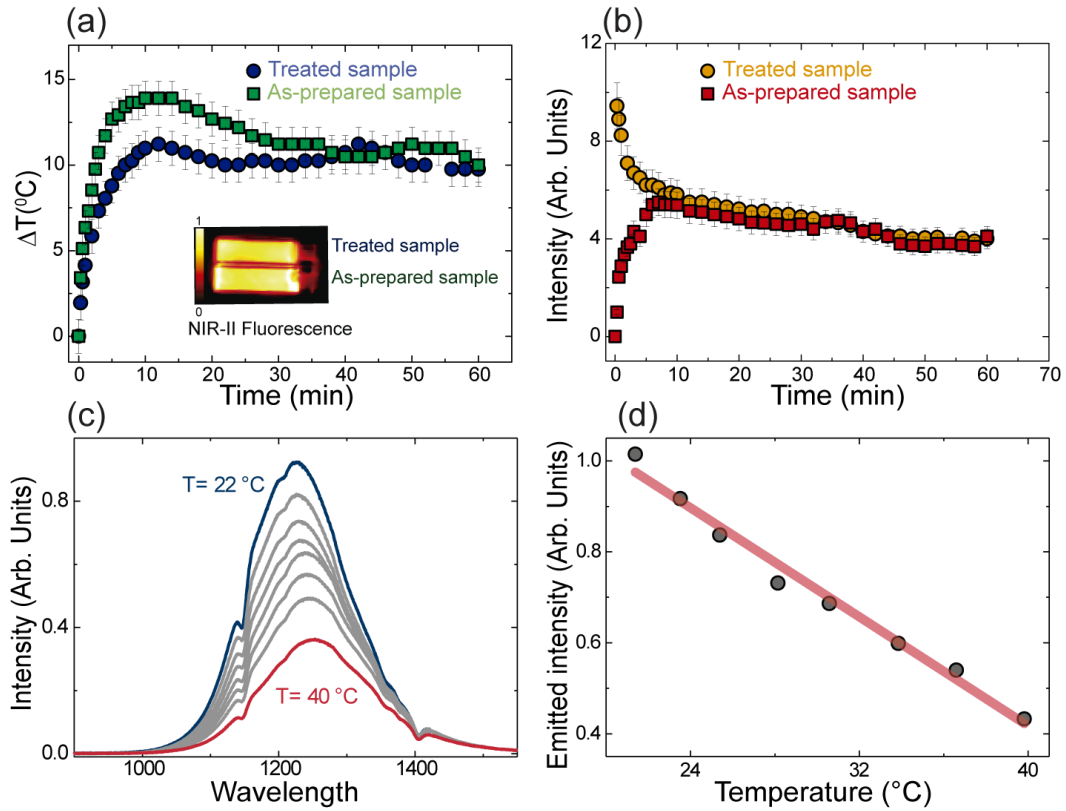

Supporting Fig. 4.13. **a)** Time evolution of temperature for as-prepared ($Ag@Ag_2S$ dots) and treated solution ($Ag/Ag_2S@AgCl$) in $CHCl_3$ during ultrafast laser irradiation with 50 fs laser pulses during 60 min at a fluence of 15 W/cm^2 **b)** Time evolution of the emitted intensity generated from both solutions during the same treatment applied as described in (a). **(c)** Luminescence emission spectra of the treated solution were investigated under an 808 nm of CW excitation laser at different temperatures ranging from 20 to 45 °C. The temperature dependence of the emitted intensity extracted from the spectra in (c) is also included in **(d)**.

4.2.6 Radiative and thermal induced non-radiative pathways

Assessing the fluorescence and thermal properties of colloidal solutions of Ag/Ag2S dots in CHCl3 as treated with the ultrafast laser (808 nm, 50 fs, 9 W/cm^2) at different time stages is a viable strategy to get deeper and better pieces of information about the thermal loading effect observed before, during and after the ultrafast fast laser treatment. **Supporting Fig. 4.14a, b and c** shows the optical, NIR-II and thermal images of the solutions treated at different time stages range from 0 to 90 min. The changing of the visual aspect (the solution become more transparent as previously mentioned in the main text) as the times goes by is here observed in detail. Here we show also the evolution of the brightness (fluorescence images) and temperature increment (thermal images) of each solution. Both, fluorescence and thermal images

were taken at the same time moment by placing them in the eye view of a fluorescence imaging system and thermal camera. A CW excitation laser of 808 nm operating at a moderate intensity (0.3 $W \cdot cm^{-2}$) was applied until the rising of temperature of each solution reached a maximum temperature and stayed steady. It is clearly shown that for longer times of ultrafast laser treatment while the brightness exhibits an increasing trend the thermal loading shows to follow an opposite direction, as can been seen more expressly in data displayed in **Supporting Fig. 4.14d.** Indeed, by comparing the temperature increment between the as-prepared Ag_2S dots and in a 90 min time-stage treated Ag_2S superdot (both in chloroform), the as-prepared Ag_2S solution shows an increment of 6.8 °C while the treated Ag_2S superdot shows only an increment of 3.7 °C. This result is completely in agreement with the previous findings described in **Supporting Fig. 4.13a**, but is to show more clearly that the dot to superdot transformation reduces the non-radiative mechanism related to thermal loading and, as a consequence, drastically increases the luminescence.

The fraction of thermal loading, (η_t), is another important physical quantity used to quantify the thermal effect observed as a function of ultrafast irradiation time. Such physical quantity provides an absolute value of the fraction of the absorbed photons that is transformed into heat throughout non-radiative electron-hole pair recombination process present when the solution of Ag_2S is photon-excited. The QY and η_t can be related to each other throughout the mathematical expression:

$$\eta_T = 1 - \mathrm{QY} * \left(\frac{\lambda_{exc}}{\langle\lambda_{em}\rangle}\right) \propto \Delta T \tag{S29}$$

Where λ_{exc} is the excitation wavelength used in our experiments (808 nm) and $\langle\lambda_{em}\rangle$ is the average emission wavelength of the Ag_2S dots found to be around 1220 nm. As additionally expressed in equation (S1) η_T is directly proportional to the increment of temperature (ΔT) of the solution after exciting it with an appropriate optical light at a specific wavelength. Here, instead of the absolute value, we report a relative net fractional thermal loading (${\eta_t}^{net}$) for each treated solution in respect to the as prepared Ag_2S dot. The ${\eta_t}^{net}$ link with the absorption efficiency (η_{abs}) through the expression:

$$\eta_t{}^{net} = \frac{\Delta T\ (t)}{\Delta T\ (0)} * \eta_{abs} \tag{S30}$$

Where $\Delta T(0)$ is the temperature increment of the as-prepared solution and $\Delta T(t)$ is in respect to the sample treated for an irradiation time *t*. Both η_{abs} and $\eta_t{}^{net}$ are plotted together with the data of QY previously showed and the results are shown in **Supporting Fig. 4.14e** and **f.** The two major pathways, photon emission and thermal loading, respectively associated with radiative and non-radiative process, are competing with each other as can been easily seen through the experimental data in **Supporting Fig. 4.14f**, in agreement with the theoretical expression in equation (S29) as well to all the previous results concerning the thermal loading effect presenting in the Ag2S dots before, during and after treatment with the ultrafast laser irradiation.

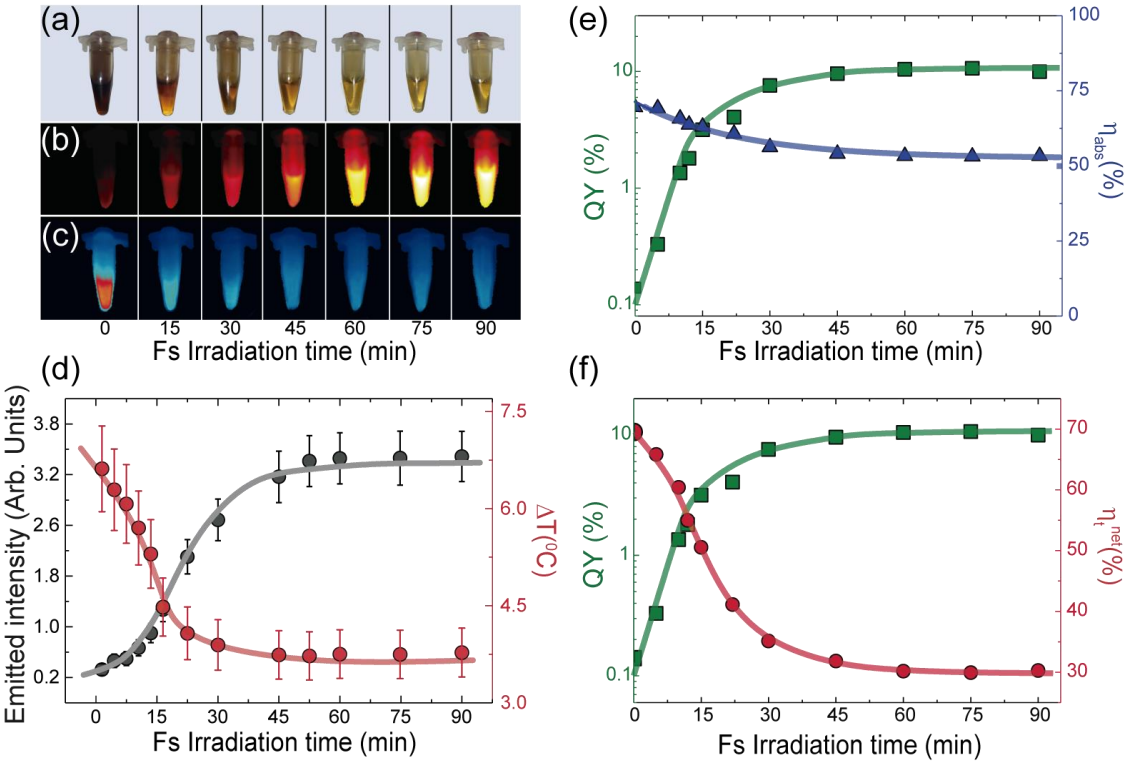

Supporting Fig. 4.14. **a)** Time evolution of temperature for as-prepared ($Ag@Ag_2S$ dots) and treated solution ($Ag/Ag_2S@AgCl$) in $CHCl_3$ during ultrafast laser irradiation with 50 fs laser pulses during 60 min at a fluence of 15 W/cm^2 **b)** Time evolution of the emitted intensity generated from both solutions during the same treatment applied as described in (a). **(c)** Luminescence emission spectra of the treated solution were investigated under an 808 nm of CW excitation laser at different temperatures ranging from

20 to 45 °C. The temperature dependence of the emitted intensity extracted from the spectra in (c) is also included in **(d)**.

4.2.7 Luminescence properties variance induced by ligand exchange procedure.

4.2.7.1 Fluorescence decay times after ligand exchange procedure

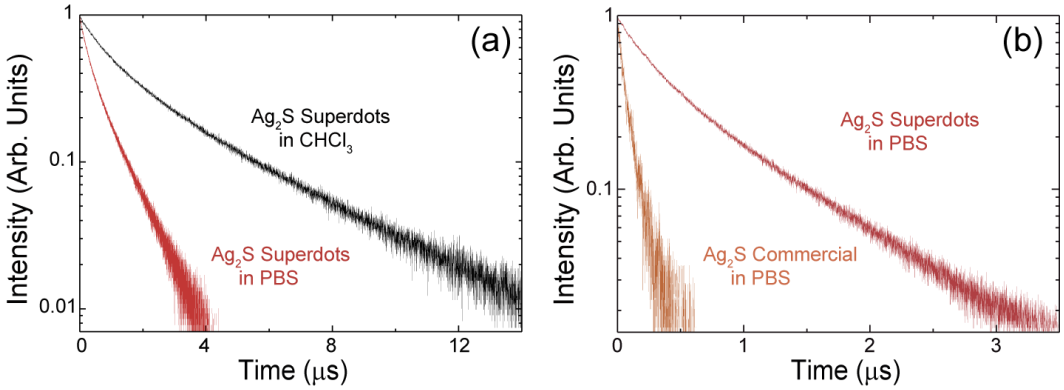

Supporting Fig. 4.15. **a)** Fluorescence decay curves from colloidal solutions of Ag_2S Supedots in $CHCl_3$ and after transfer it to PBS through ligand exchange procedure explained above. **b)** Fluorescence decay curves from colloidal solutions of Ag_2S Supedots and commercial ones. In both cases, particles are coated with PEG and dispersed in PBS.

4.2.7.2 Quantum Yields (QY) and Lifetime

Solution	QY (%)	Lifetime (μs)
Ag_2S Superdot in $CHCL_3$	10	2
Ag_2S Superdot in PBS	5.7	0.6
Ag_2S commercial in PBS	0.36	0.06

Supporting Table 4.3. Photoluminescence Quantum Yield (PLQY) of Ag_2S Superdot before ($CHCL_3$) and after (PBS) applying ligand exchange procedure. PLQY corresponding Ag_2S commercial in PBS is also included for comparison purposes.

4.2.8 Comparison between Ag_2S Superdot and FDA approved ICG dye in Near Infrared Second Biological Window.

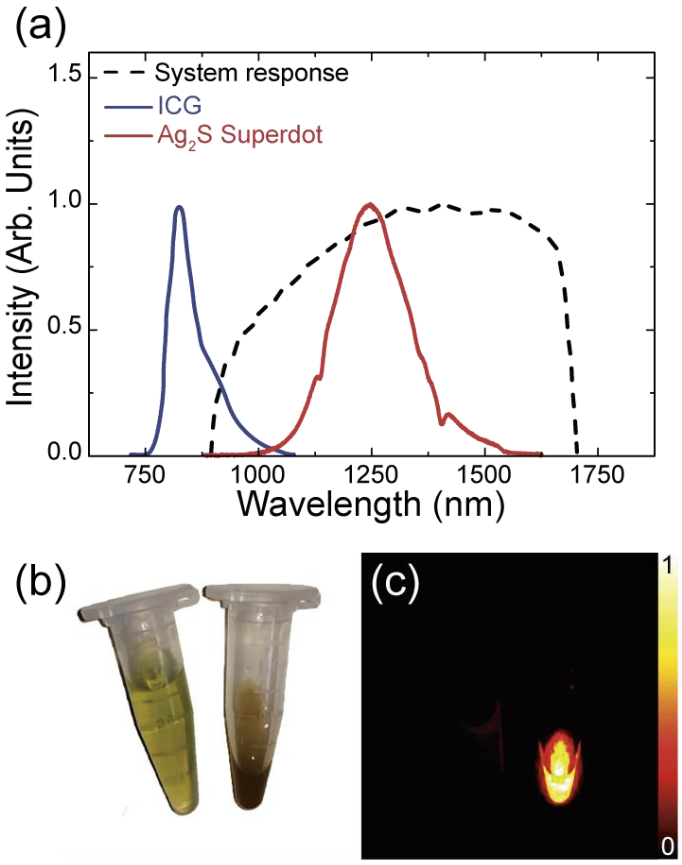

Supporting Fig. 4.16. **a)** The normalized emission spectra of ICG and Ag_2S Superdot plotted together with the spectral response of our NIR-II in vivo imaging system, demonstrating clearly that the ICG has only a poor overlap between its tail and the spectra response of the acquisition system. **b)** Optical and NIR-II fluorescence images of colloidal solutions of ICG and Ag_2S Superdot. A by far brighter emission is observed for Ag_2S Superdot as it is compared with ICG.

4.2.9 Guarantee of minimum thermal loading during the acquisition of real-time in vivo images by requiring low power densities using Ag_2S Superdot.

Temperature increment studies after illuminate whole-body of an individual mouse with an 810 nm fiber-coupled laser at different power densities were carried out. The laser was applied during 4 min in order to reach a maximum steady temperature value. The results are present in **Fig. S8**, where the mouse with fur and without white fur was studied. The maximum temperature increment was found to be 5 and 3 °C for before and after shave the mouse, respectively. We can see in the data of **Fig. S8** that such increment of temperatures was able to get by using an excitation light intensity of 240 mW/Cm^2. The lower temperature increment for the mouse with white fur reflects that

fact that white fur (in general, white objects) reflects all the wavelengths of the visible light, including a remarkable reflection at 808 nm, as a result the mouse with white fur absorbs less 808 nm light than mouse without the white fur (were the skin is found to be a rose beige color), promoting less conversion of energy photos of 808 nm into thermal heating. The mainly information extract from these data is that the maximum temperature increment was found to be less than 0.5 °C for a power density of 50 mW/cm^2 used during the acquisition of real-time *in* vivo images.

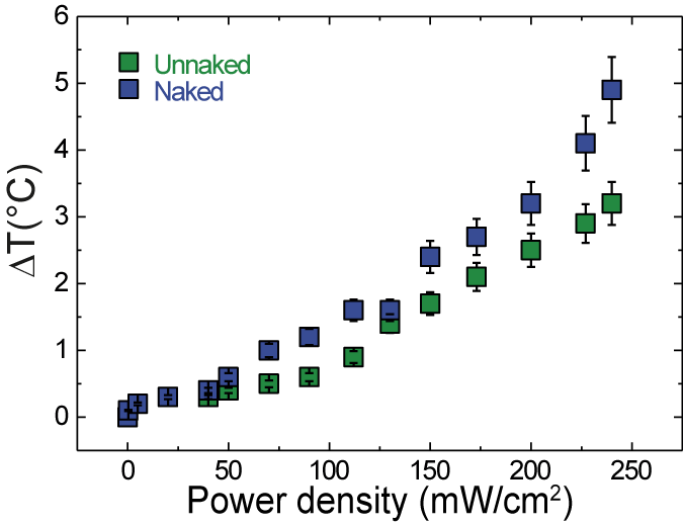

Supporting Fig. 4.17. Temperature increment after illuminate whole-body of an individual mouse with an 810 nm fiber-coupled laser at different power densities. The experiment was made in a mouse before and after shaving its fur.

4.2.10 Noteworthy works recently reported in NIR-II fluorescence pre-clinical imaging

Supporting Table 4.4. Noteworthy works recently reported in NIR-II fluorescence pre-clinical imaging using Ag_2S dots as well as others remarkable NIR-II nanoprobes.

Sample	**Basic optical**	**Characteristic**	**Surface (Chemistry and Charge)**		**In vivo experiment**		**Volume**
			Coating/Functionalization	Z-potential	Reported concentration	Power density	
Exchange-SWNTs	808 nm	1150 nm	PL–PEG	N/A	0.17 mg/mL	0.13 W cm -2	200 μL[1]

Single-walled CNTs	808 nm	Main peak 1200 nm	DSPE-mPEG	N/A	500 n M (i.e. 108 mg/ml)	0.14 W cm -2	200 µL[2]
NaYF 4 :Yb 3+ , Er 3+	980 nm	1525 nm	HAS	-13.6 mV	3 n M	0.14 W cm -2	100 µL[3]
RE-Doped a) core/multishell	800 nm	1525 nm	DSPE-PEG2000-COOH	N/A	20–100 n M	0.2 W cm −2	200 µL[4]
PbS/CdS/ZnS	808 nm	1270 nm	MPA	-24.2 mV	0.04 mg mL −1	0.10 W cm -2	100 µL[5]
IR-1061	808 nm	900-1300 nm	DSPE-mPEG	N/A	0.27 mg/mL	0.14 W cm -2	200 µL[6]
Ag 2 S	808 nm	1100nm	DOX@PEG	N/A	1.5 mg/mL	0.45 W/cm2	200 µL[7]
Ag 2 S	808 nm	1200 nm	PEGylated	N/A	1 mg/mL	0.126 W/cm2	200 mL[8]
Ag 2 S	808 nm	1200 nm	6PEG	N/A	1.34 mg mL -1 (i.e. 0.75 n M)	0.14 W cm -2	200 µL[9]
Ag 2 S	808 nm	1200 nm	PEGylated	N/A	1.5 mg/mL	0.14 W cm -2	200 µL[10]
Ag 2 S	808 nm	1200 nm	PEG-Tat Peptide- hMSCs		12.5 µg/mL	0.124 W/cm2	250 µ L[11]
Ag_2S Super	808 nm	1220 nm	PEGylated	-30 mW	0.15 mg/mL	0.05 W/cm2	100 µL

5 Conclusions and future

In the course of this study, we developed miscellaneous tools to tackle assorted procedural problems concerned medical issues. The conclusion and future possibilities based on the findings of this doctoral thesis shall be summed up.

5.1 Conclusions and perspectives about Ag_2S nanodots for Lifetime-Based Luminescence Thermometry in the Near Infrared Second Biological Window (NIR-II BW)

- *The results show that decay curves are strongly dependent on the coupling with the surrounding medium. Ag2S nanodots stable in water (PEG coated) have been found to follow faster dynamics with respect to those nanodots dispersed in toluene (DDT coated) due to the activation of surface related de-excitation processes, while keeping the bulk recombination dynamics unaltered.*

- *The fluorescence decay time showed up to be independent of wavelength emission, suggesting the absence of quantum confinement effects, therefore, it should be state that we were not deal with quantum dots base on Ag_2S, but instead of it we were in a scale size significantly larger in comparison to the bohr exciton radious determined for semiconductors of Ag_2S.*

- *The time-resolved fluorescence decay dynamics of our Ag_2S nanodots show to be strongly temperature dependent, mainly the fluorescence lifetime of bulk transitions, showing remarkable shortenings in the temperature range of interest in biomedicine (0–50 °C).*

- *For PEG-coated Ag_2S nanodots dispersed and stable in water, it is worthy to mention that the multiphonon assisted non-radiative pathways associated with surface defects are remarkable stronger by increasing the temperature. This is a consequence of*

the fact that temperature assisted energy migrations from bulk to surface states become more prominent as the temperature rises.

- *The fluorescence lifetime-based thermal sensitivity of Ag_2S nanodots showed up to be not critically depend on neither the environment that they were dispersed nor the surface properties.*

- *Based on the findings concerning the fluorescence lifetime-based thermal sensing competency of our Ag_2S nanodots, a plan was traced for developing and operating their thermal sensing talent in a direct application regarding subcutaneous thermal readout. Time and spatial informations about thermal gradients induced by temperature increments were accurately obtained by using the Ag_2S nanodots.*

- *The findings regarding subtissue thermal reading were of fundamental importance, in which we could estimate a large difference between subtissue and surface temperature. Discriminate this difference is of extraordinary matter, since during therapies of cancer tumors induced by hyperthermia, controlling only the surface temperature of a tumor induces a big mistake when compared to its inner one.*

5.2 Conclusions and perspectives about Ag_2S nanodots for Tumor Detection Based-Luminescence Transient Nanothermometry (LTNh)

- *The temperature dependency of fluorescence emission of our PEG-coated Ag_2S nanodots licensed us to apply them for in vivo tumor detection based on luminescence thermometry that shall be the basis of future protocols for any early tissue abnormalities/disorders diagnosis*

- *The thermometry-based approach was applied to perform temperature readout of a tumor tissue after subjecting it to a heat stimulus. The NIR-II fluorescence emission from Ag_2S nanodots make them working as reliable nanothermometers capable of providing a precise, contactless thermal reading inside of the induced melanoma tumor.*

- *Fluorescence-based nanothermometers were successfully employed for monitoring modifications in physiological tissue properties through variations in their thermal dynamics during cooling process.*

- *Physiological changes were found to take place when a melanoma tumor is developing, causing remarkable differences in the fluorescence thermal transient of Ag_2S when compared to those placed in a healthy tissue.*

- *The obtained results regarding murine model of melanoma reveal that at the early stages of tumor development (up to 7 days before it could be detected by optical inspection) there were evident differences in the thermal relaxation dynamics between a region localized in the tumoral tissue and in healthy ones.*

- *The obtained results regarding the murine model of melanoma reveal that at the early stages of tumor development (up to 7 days before it could be detected by optical inspection) there were evident differences in the thermal relaxation dynamics between a region localized in the tumoral tissue and in healthy ones.*

- *Behind the observed modifications in the thermal relaxation dynamics of tissue during the tumor development, the thermal regulatory mechanisms such as blood perfusion as well as metabolic heat energy generation have played a determining role in causing differences related to the physiological status of a tumoral tissue as it passes through the phases of angiogenesis and necrosis.*

- *Although we have limited our demonstration to a murine model of melanoma, thermal transient thermometry would also be applicable to any tumor whose development entailed a significant modification in blood perfusion (virtually all solid tumors), as long as it was accessible by a laser beam.*

- *As angiogenesis and necrosis are both common processes during tumor development, the technique here presented has the potential to become an almost universal technique for detection of solid tumors and identification of their development stage. The results presented in this work introduce to the scientific community the possibility of applying luminescence nanothermometry as a diagnosis tool, which could be valuable for early detection not only of tumors, but also of other pathologies that entail changes in the blood perfusion, as is the case of any cardiovascular diseases.*

5.3 Conclusions and perspectives about Ag_2S Dot-to-Superdot transformation triggered by femtosecond laser pulses.

- *The included basic scientific findings here would be promoting improvements in applied medical research, engineering research, and advanced technology development. In the included studies the performance testing and or operational monitoring of our hybrid structures of Ag_2S Superdots in fluorescence imaging in in vivo probes were testified guaranteed excellent results.*

- *Remarkable improvements concerning the photoluminescence quantum yield (PLQY) accompanied by increments of the luminescence decay times could be achieved by applying an inedited methodology based on physical-chemical nanoengineering by means of high energetic energy pulses provide by ultra-fast laser.*

- *Thanks to the excellent fluorescence as well as structural perfection achieved no need for expensive detection systems as well as high doses of contrast agent in vivo experiments are required.*

- *The longer-lived luminescence decay of the obtained Ag_2S, together with the highest bright so far reported among fluorescence contrast agents for bioassays, opens up the possibility for applying them to applications in time-gated biological imaging acquisition. This is a great advantage concerning to perform imaging acquisition in biological living because it is an absolute measurement methodology showing no dependence with excitation laser intensity as well as avoiding any signal from tissues` autofluorescence.*

- *Summing up, if one considers the advantage offered by these NPs, including photochemical stability and optimum spectral operation range, the more than one order of magnitude improvement in their quantum yield demonstrated here should constitute the first step towards their translation into the clinics. In our findings, the demonstrated power of ultrafast laser pulses to improve luminescent nanoparticles, may also stimulate new concepts on synthesis procedures that could benefit from the synergy between traditional chemical procedures and light-matter interaction processes.*

5 Conclusiones y futuro

A lo largo de los estudios de esta tesis, desarrollamos diversas herramientas para abordar una variedad procedimientos relacionados con problemas médicos. Ahora se resumirán la conclusión y las posibilidades futuras basadas en los resultados obtenidos.

5.1 Conclusiones y perspectivas a respecto nanodots Ag_2S para termometría basada en la vida promedia de la luminiscencia en la segunda ventana biológica del infrarrojo cercano (NIR-II BW)

- *De hecho, los resultados muestran que las curvas de decaimiento de luminiscencia dependen fuertemente del acoplamiento con el medio circundante. Se ha encontrado que los nanodots Ag_2S estables en agua (recubiertos con PEG) siguen dinámicas más rápidas con respecto a los nanodots dispersos en tolueno (recubiertos con DDT) debido a la activación de procesos de desexcitación relacionados con la superficie mientras se mantiene inalterada la dinámica de recombinación de 'bulk'.*

- *El tiempo de decaimiento de la fluorescencia mostró ser independiente de la longitud de onda de emisión, lo que sugiere la ausencia de efectos de confinamiento cuántico, por lo tanto, indicase que no estábamos tratando con puntos cuánticos de Ag_2S, sino que estábamos en un tamaño de escala significativamente mayor en comparación con el radio de exciton de bohr de este mismo semiconductor.*

- *La dinámica de decaimiento de la fluorescencia resuelta en el tiempo de nuestros nanodots Ag_2S muestra tener una fuerte dependencia con la temperatura, principalmente la vida promedia de la fluorescencia de las transiciones de 'bulk', manifestando una reducción notable en el rango de temperatura de interés en biomedicina (0-50 ° C).*

- *Con respecto a los nanodots Ag_2S recubiertos con PEG, dispersos y estables en agua, vale la pena mencionar que las vías no radiativas asistidas por multifonones debida a los defectos superficiales son notablemente más fuertes al aumentar la temperatura. Esto es una consecuencia del hecho de que las migraciones de energía,*

asistidas por multifonones, de los estados de 'bulk' a la superficie se vuelven más prominentes a medida que aumenta la temperatura.

- *La sensibilidad térmica basada en la vida promedia de la fluorescencia de los nanodots Ag_2S demostró no depender críticamente ni del entorno en que se dispersaron ni de las propiedades de la superficie.*

- *Con base en los resultados relacionados con la eficiencia de lectura de temperatura basada en la vida promedia de fluorescencia de nuestros nanodots Ag_2S, se trazó un plan para desarrollar y operar su capacidad de detección térmica en una aplicación directa con respecto a la lectura térmica de tejidos subcutáneos. La información espacial y de tiempo sobre gradientes térmicos inducidos por incrementos de temperatura se obtuvieron con precisión mediante el uso de nanodots Ag_2S.*

- *Los hallazgos con respecto a la lectura térmica del subtejido fueron de fundamental importancia, en la cual pudimos estimar una gran diferencia entre el subtejido y la temperatura de la superficie. Discriminar esta diferencia es de extraordinaria importancia, ya que durante las terapias de tumores cancerosos inducidos por hipertermia, controlar solo la temperatura de la superficie de un tumor induce un gran error en comparación con su interior.*

5.2 Conclusiones y perspectivas a respecto de los nanodots Ag_2S para detección de tumores basadas en la nanotermometría transitoria de luminiscencia (LTNh)

- *La dependencia de la emisión de fluorescencia con la temperatura de nuestros nanodots Ag_2S, recubiertos con PEG, nos permitió aplicarlos para la detección de tumores en in vivo usando la termometría de luminiscencia, que es muy promisoria para ser la base en futuros protocolos para cualquier diagnóstico temprano de anomalías y trastornos tisulares.*

- *La propuesta de termometría basada en luminiscencia se aplicó en la realización de lectura de temperatura de un tejido tumoral después de someterlo a un*

estímulo térmico. La emisión de fluorescencia NIR-II de los nanodots Ag_2S los permiten funcionar como nanotermómetros confiables capaces de proporcionar una lectura térmica precisa y sin contacto en el interior del tumor de melanoma inducido.

- *Los nanotermómetros Ag_2S se emplearon con éxito para monitorear modificaciones en las propiedades fisiológicas del tejido a través de variaciones en su dinámica térmica durante el proceso de enfriamiento.*

- *Se encontraron cambios fisiológicos a lo largo del desarrollo del tumor de melanoma, que causaron diferencias notables en la relajación térmica de fluorescencia de los Ag_2S en comparación cuando estaban en tejido sano.*

- *Los resultados con respecto el modelo murino de melanoma revelan que en las primeras etapas del desarrollo del tumor (hasta 7 días antes de que pudiera detectarse mediante inspección óptica) hubo diferencias evidentes en la dinámica de relajación térmica entre un sitio localizado en el tejido tumoral y en lo sano.*

- *Detrás de las modificaciones observadas en la dinámica de relajación térmica del tejido durante el desarrollo del tumor, los mecanismos de regulación térmica como la perfusión sanguínea y la generación de energía de calor metabólica, han desempeñado un papel determinante induciendo diferencias notables relacionadas con el estado fisiológico de un tejido tumoral a lo largo que este pasó por las fases de angiogénesis y necrosis.*

- *Aunque hemos limitado nuestra demostración a un modelo murino de melanoma, la termometría de transeúnte térmico también sería aplicable a cualquier tumor cuyo desarrollo implicara una modificación significativa en la perfusión sanguínea (prácticamente todos los tumores sólidos), siempre que fuera accesible por un rayo láser.*

- *Angiogénesis y la necrosis son procesos comunes durante el desarrollo del tumor, entonces la técnica aquí presentada tiene el potencial de convertirse en una técnica casi universal para la detección de tumores sólidos y para la identificación de su fase a lo largo del desarrollo. Los resultados presentados en este trabajo presentan para la comunidad científica la posibilidad de aplicar la nanotermometría de*

luminiscencia como herramienta de diagnóstico, lo que podría ser valioso para la detección temprana no solo de tumores, sino también de otras patologías que conllevan cambios en la perfusión sanguínea, como es el caso de enfermedades cardiovasculares en general.

5.3 Conclusiones y perspectivas sobre la transformación de punto para superpunto Ag_2S desencadenada por pulsos de láser de femtosegundos

- *Los hallazgos científicos básicos incluidos aquí habrá de promover mejoras en la investigación médica aplicada, la investigación de ingeniería y el desarrollo de tecnología avanzada. En los estudios incluidos, las pruebas de rendimiento y/o el monitorio operacionales de nuestras estructuras híbridas de superpuntos Ag_2S como sondas en in vivo a través de imágenes de fluorescencia testificaron y demostraron excelentes resultados.*

- *Mejoras increíbles en el rendimiento cuántico de fotoluminiscencia (PLQY) fueron obtenidas. Acompañado de incrementos de los tiempos de decaimiento de la luminiscencia aplicando una metodología inédita basada en nanoingeniería físico-química mediante pulsos de alta energía energética proporcionados por láser ultrarrápido*

- *Gracias a la excelente fluorescencia, así como a la perfección estructural lograda, no se necesitan sistemas de detección costosos, así como también no se requieren altas dosis de agente de contraste para experimentos in vivo.*

- *El largo tiempo de vida de luminiscencia de los Ag_2S obtenidos, junto con el más alto brillo hasta ahora reportado entre los agentes de contraste de fluorescencia para bioensayos, se abre la posibilidad de aplicarlos en adquisición de imágenes biológicas con la técnica conocida como ' time-gated'. Esta técnica es una gran ventaja con respecto a la adquisición de imágenes de sistemas biológicos porque es una metodología de medición absoluta que no muestra dependencia con la intensidad del láser de excitación y evita cualquier señal de autofluorescencia de los tejidos.*

- *En resumen, si se considera las ventajas que ofrecen estas NPs, incluida la estabilidad fotoquímica, el rango óptimo de operación espectral y la mejora de más de un orden de magnitud en sus rendimiento cuántico. Todo esto deberá constituir el primer paso para aplicarlos a nivel clínico. En nuestros hallazgos, a los cuales pulsos de láser ultrarrápidos demostraron gran eficiencia para mejorar las nanopartículas luminiscentes, abren la posibilidad de estimular nuevos conceptos sobre procedimientos de síntesis que puedan beneficiarse de la sinergia entre los procedimientos químicos tradicionales y los procesos de interacción de la luz con la materia*.

5 Conclusões e futuro

Ao longo dos estudos desta tese, desenvolvemos várias ferramentas para abordar uma variedade de procedimentos relacionados a questões médicas. Agora, resumiremos as conclusões desses estudos e algumas possibilidades futuras.

5.1 Conclusões e perspectivas em relação aos nanodots Ag_2S para termometria baseada no tempo de vida de luminescência na segunda janela biológica do infravermelho próximo (NIR-II BW)

- *De fato, os resultados mostram que as curvas de decaimento de luminescência são fortemente dependentes de efeitos relacionados ao meio circundante. Verificou-se que os nanodots Ag_2S estáveis em água (revestidos com PEG) seguem uma dinâmica mais rápida em relação aos nanodots dispersos em tolueno (revestidos com DDT) devido à ativação de processos de desexcitação relacionados à superfície, mantendo a dinâmica de recombinação de 'bulk' inalterada.*

- *O tempo de decaimento da fluorescência mostrou-se independente do comprimento de onda de emissão, sugerindo a ausência de efeitos de confinamento quântico, indicando que não estávamos lidando com pontos quânticos "quantum dots" de Ag_2S, mas com partículas de tamanho em escala significativamente maior em comparação com o raio de bohr exciton desse semicondutor.*

- *A dinâmica do decaimento de fluorescência resolvida no tempo de nossos nanodots Ag_2S mostra uma forte dependência com a temperatura, principalmente a vida média de fluorescência das transições de 'bulk', mostrando uma notável redução no regime de temperatura de interesse em biomedicina (0-50 ° C).*

- *No que diz respeito aos nanodots Ag_2S revestido com PEG, dispersos e estáveis em água, vale a pena mencionar que os caminhos não radioativos assistidos por multifonons, relacionados a defeitos superficiais, são notavelmente mais fortes com o aumento de temperatura. Isto é uma consequência do fato que as migrações de energia, assistidas por multifonons, com origem em estados de 'bulk' para estados de superfície ficam mais proeminentes à medida que a temperatura aumenta.*

- *A sensibilidade térmica baseada no tempo de vida de fluorescência dos nanodots Ag_2S demonstrou não depender criticamente do ambiente em que estavam dispersos ou das propriedades da superfície.*

- *Com base nos resultados relacionados com a eficiência da leitura de temperatura baseada no tempo de vida de fluorescência dos nanodots Ag_2S, desenvolvemos e realizamos uma aplicação para leituras de temperatura de tecidos subcutâneos. Informações espacial e temporal através de gradientes térmicos induzidos por incrementos de temperatura foram obtidas com precisão através do uso de nanodots Ag_2S.*

- *Os achados referentes à leitura térmica subcutânea de tecidos foram de fundamental importância. Conseguimos estimar uma grande diferença entre temperatura entre um tecido subcutâneo e superficial. Discriminar essa diferença é de extraordinária importância, pois durante as terapias cancerígenas induzidas por hipertermia, ao controlar apenas a temperatura da superfície de um tumor induz um grande erro em comparação com seu interior.*

5.2 Conclusões e perspectivas em relação aos nanodots Ag_2S para detecção de tumores baseada em nanotermometria de transiente de luminescência (LTNh)

- *A dependência da emissão de fluorescência com a temperatura de nossos nanodots Ag_2S, revestidos com PEG, nos permitiu aplicá-los na detecção de tumores em in vivo através do uso da termometria de luminescência, em que é muita promissora e poderá ser a base em protocolos futuros para diagnóstico precoce de anormalidades e distúrbios teciduais.*

- *A proposta de termometria baseada em luminescência foi aplicada na realização de leitura da temperatura de um tecido tumoral após submetê-lo a um estímulo térmico. A emissão de fluorescência NIR-II dos nanodots Ag_2S garante uma nanotermometria confiável, capaz de fornecer uma leitura térmica precisa e sem contato dentro do tumor de melanoma induzido.*

- *Nanotermômetros de Ag_2S foram utilizados com sucesso para monitorar alterações nas propriedades fisiológicas de tecido através de variações em sua dinâmica térmica durante o processo de resfriamento.*

- *Alterações fisiológicas foram encontradas ao longo do desenvolvimento do tumor de melanoma, que causaram diferenças notáveis no transiente térmico de fluorescência dos nanodots de Ag_2S em comparação quando estes estavam em um tecido saudável.*

- *Os resultados referentes ao modelo de melanoma murino revelam que, nos estágios iniciais do desenvolvimento do tumor (até 7 dias antes de poder ser detectado por inspeção óptica), havia diferenças óbvias na dinâmica de relaxação térmica quando regiões de tecido tumoral e saudável eram comparadas..*

- *Por trás das mudanças observadas na dinâmica do relaxamento térmico do tecido durante o desenvolvimento do tumor, mecanismos de regulação térmica como a perfusão sanguínea e a geração de energia térmica metabólica, desempenharam um papel decisivo induzindo diferenças notáveis relacionadas ao estado fisiológico de um*

tecido tumoral ao longo do seu desenvolvimento, passando pelas fases de angiogênese e necrose.

- *Embora restringimos nossa demonstração a um modelo de melanoma murino, a termometria de relaxação térmica também se aplica a qualquer tumor cujo desenvolvimento envolvesse uma modificação significativa na perfusão sanguínea (praticamente todos os tumores sólidos), desde que acessível por um feixe laser.*

- *Angiogênese e necrose são processos comuns durante o desenvolvimento do tumor; portanto, a técnica aqui apresentada tem o potencial de se tornar uma técnica quase universal para a detecção de tumores sólidos e para a identificação de estágios ao longo do desenvolvimento de tumores. Os resultados apresentados neste trabalho apresentam à comunidade científica a possibilidade de aplicar a nanotermometria de luminescência como ferramenta de diagnóstico, que pode ser valiosa para a detecção precoce não apenas de tumores, mas também de outras patologias que levam a alterações na perfusão sanguínea, como é o caso das doenças cardiovasculares em geral.*

5.3 Conclusões e perspectivas sobre a transformação de 'dot' para o 'superdot' Ag2S induzida por pulsos de laser de femtossegundos

- *As descobertas científicas básicas incluídas aqui promoverão melhorias na pesquisa médica aplicada, pesquisa de engenharia e desenvolvimento de tecnologia avançada. Nos estudos incluídos, os testes de desempenho e/ou o monitoramento operacional de nossas estruturas híbridas de superdot Ag_2S como sondas em in vivo através de imagens de fluorescência foram testemunhados e demonstraram excelentes resultados.*

- *Foram obtidas melhorias incríveis no rendimento quântico da fotoluminescência (PLQY). Acompanhado por aumentos nos tempos de decaimento da luminescência, aplicando uma metodologia sem precedentes baseada em nanoengenharia físico-química, usando pulsos de alta energia fornecidos por laser ultrarrápidos.*

- *Graças à excelente fluorescência, bem como à perfeição estrutural alcançada, não são necessários sistemas caros de detecção, assim como altas doses de agente de contraste não são necessárias para experimentos em in vivo.*

- *O longo tempo de vida de luminescência do Ag_2S obtido, juntamente com o maior brilho até agora relatado entre os agentes de contraste de fluorescência para bioensaios, abre a possibilidade de aplicá-los na aquisição de imagens biológicas através da técnica conhecida como 'time-gated'. Essa técnica tem uma grande vantagem em relação à aquisição de imagens de sistemas biológicos, pois é uma metodologia de medição absoluta que não mostra dependência com a intensidade do laser de excitação e evita qualquer sinal de autofluorescência tecidual.*

- *Em resumo, considerando as vantagens oferecidas por essas NPs, incluindo estabilidade fotoquímica, regime ideal de operação espectral e a melhoria de mais de uma ordem de magnitude em seu rendimento quântico. Tudo isso deve ser o primeiro passo para aplicá-los a nível clínico.*

- *Em nossas descobertas, para as quais pulsos de laser ultra-rápidos demonstraram grande eficiência na melhoria de nanopartículas luminescentes, abrem a possibilidade de estimular novos conceitos sobre procedimentos de síntese que podem se beneficiar da sinergia entre procedimentos químicos tradicionais e processos de interação com luz com a matéria.*

6 REFERENCES

[1] **a) B. del Rosal, D. H. Ortgies, N. Fernández, F. Sanz-Rodríguez, D. Jaque, E. M. Rodríguez, *Advanced Materials* 2016, 28, 10188; b) H. D. A. Santos, E. C. Ximendes, M. d. C. Iglesias-de la Cruz, I. Chaves-Coira, B. del Rosal, C. Jacinto, L. Monge, I. Rubia-Rodríguez, D. Ortega, S. Mateos, J. GarcíaSolé, D. Jaque, N. Fernández, *Advanced Functional Materials* 2018, 28, 1803924; c) E. Carrasco, B. del Rosal, F. Sanz-Rodríguez, Á. J. de la Fuente, P. H. Gonzalez, U. Rocha, K. U. Kumar, C. Jacinto, J. G. Solé, D. Jaque, *Advanced Functional Materials* 2015, 25, 615.**

[2] **C. Panati, in *Toys That Glow in the Dark: 1603, Italy*, (Ed: P. Library), ESTADOS UNIDOS; ENCICLOPEDIAS; DICCIONARIOS, New York, US 1987, 463.**

[3] **B. Valeur, M. N. Berberan-Santos, *Journal of Chemical Education* 2011, 88, 731.**

[4] **D. M. Reynolds, in *Aquatic Organic Matter Fluorescence*, DOI: DOI: 10.1017/CBO9781139045452.004 (Eds: A. Baker, D. M. Reynolds, J. Lead, P. G. Coble, R. G. M. Spencer), Cambridge University Press, Cambridge 2014, p. 3.**

[5] **B. K. Watson, A. H. Coons, *The Journal of experimental medicine* 1954, 99, 419.**

[6] **A. H. Coons, H. J. Creech, R. N. Jones, *Proceedings of the Society for Experimental Biology and Medicine* 1941, 47, 200.**

[7] **Z. Liu, Luke D. Lavis, E. Betzig, *Molecular Cell* 2015, 58, 644.**

[8] **A. V. Naumova, M. Modo, A. Moore, C. E. Murry, J. A. Frank, *Nature biotechnology* 2014, 32, 804.**

[9] **E. Pastrana, *Nature Methods* 2012, 10, 36.**

[10] **A. S. Klymchenko, Y. Mely, *Progress in molecular biology and translational science* 2013, 113, 35.**

[11] **a) C. Zheng, M. Zheng, P. Gong, D. Jia, P. Zhang, B. Shi, Z. Sheng, Y. Ma, L. Cai, *Biomaterials* 2012, 33, 5603; b) C. Wu, Y. Zhang, Z. Li, C. Li, Q. Wang, *Nanoscale* 2016, 8, 12531.**

[12] **W. Zhong, *Analytical and Bioanalytical Chemistry* 2009, 394, 47.**

[13] **E. C. Ximendes, W. Q. Santos, U. Rocha, U. K. Kagola, F. Sanz-Rodríguez, N. Fernández, A. d. S. Gouveia-Neto, D. Bravo, A. M. Domingo, B. del Rosal, C. D. S. Brites, L. D. Carlos, D. Jaque, C. Jacinto, *Nano Letters* 2016, 16, 1695.**

[14] **X. Jia, D. Li, J. Li, E. Wang, *RSC Advances* 2015, 5, 80929.**

[15] **W. Yang, P. Thordarson, J. J. Gooding, S. P. Ringer, F. Braet, *Nanotechnology* 2007, 18, 412001.**

[16] **C. Wang, Y. Wang, L. Xu, D. Zhang, M. Liu, X. Li, H. Sun, Q. Lin, B. Yang, *Small* 2012, 8, 3137.**

[17] **a) X. Cui, B. Wan, Y. Yang, X. Ren, L.-H. Guo, *Scientific reports* 2017, 7, 1518; b) Z. Lin, H. Zhang, J. Huang, Z. Xi, L. Liu, B. Lin, *Toxicology Research* 2014, 3, 497.**

[18] **a) G. Hong, J. T. Robinson, Y. Zhang, S. Diao, A. L. Antaris, Q. Wang, H. Dai, *Angewandte Chemie (International ed. in English)* 2012, 51, 9818; b) Y. Zhang, Y. Zhang, G. Hong, W. He, K. Zhou, K. Yang, F. Li, G. Chen, Z. Liu, H. Dai, Q. Wang, *Biomaterials* 2013, 34, 3639.**

[19] **a) D. A. Harrisson Santos, E. C. Ximendes, M. d. C. Iglesias-de la Cruz, I. Chaves-Coira, B. del Rosal, C. Jacinto, L. Monge, I. Rubia-Rodríguez, D. Ortega, S. Mateos, J. GarcíaSolé, D. Jaque, N. Fernández, *Advanced Functional Materials* 2018, 28, 1803924; b) C. Li, Y. Zhang, M. Wang, Y. Zhang, G. Chen, L. Li, D. Wu, Q. Wang, *Biomaterials* 2014, 35, 393; c) D. A. Harisson Santos, D. Ruiz, G. Lifante, C. Jacinto, B. H. Juarez, D. Jaque, *Nanoscale* 2017, DOI: 10.1039/c6nr08534b; d) Y. Zhang, G. Hong, Y. Zhang, G. Chen, F. Li, H. Dai, Q. Wang, *ACS Nano* 2012, 6, 3695; e) P. Jiang, C.-N. Zhu, Z.-L. Zhang, Z.-Q. Tian, D.-W. Pang, *Biomaterials* 2012, 33, 5130; f) C. Li, F. Li, Y. Zhang, W. Zhang, X. E. Zhang, Q. Wang, *ACS Nano* 2015, 9, 12255; g) B. del Rosal, D. Ruiz, I. Chaves-Coira, B. H. Juárez, L. Monge, G. Hong, N. Fernández, D. Jaque, *Advanced Functional Materials* 2018, 28, 1806088.**

[20] **S. I. Sadovnikov, A. I. Gusev, *Journal of Materials Chemistry A* 2017, 5, 17676.**

[21] **A. Olkhovets, R. C. Hsu, A. Lipovskii, F. Wise, *Physical Review Letters - PHYS REV LETT* 1998, 81, 3539.**

[22] **D. Ruiz, B. Del Rosal, M. Acebron, C. Palencia, C. Sun, J. Cabanillas-Gonzalez, M. Lopez-Haro, A. Hungria, D. Jaque, B. Juárez, *Advanced Functional Materials* 2016, 27, 1604629.**

[23] **Y. Shen, J. Lifante, E. Ximendes, H. D. A. Santos, D. Ruiz, B. H. Juárez, I. Zabala Gutiérrez, V. Torres Vera, J. Rubio Retama, E. Martín Rodríguez, D. H. Ortgies, D. Jaque, A. Benayas, B. del Rosal, *Nanoscale* 2019, DOI: 10.1039/C9NR05733A.**

[24] **Y. Du, B. Xu, T. Fu, M. Cai, F. Li, Y. Zhang, Q. Wang, *Journal of the American Chemical Society* 2010, 132, 1470.**

[25] **H. D. A. Santos, D. Ruiz, G. Lifante, C. Jacinto, B. H. Juarez, D. Jaque, *Nanoscale* 2017, 9, 2505.**

[26] **A. Ivaturi, S. K. W. MacDougall, R. Martín-Rodríguez, M. Quintanilla, J. Marques-Hueso, K. W. Krämer, A. Meijerink, B. S. Richards, *Journal of Applied Physics* 2013, 114, 013505.**

[27] **A. Mami, I. Mellouki, M. B. Mbarek, M. Amlouk, N. Yacoubi, *IEEE Sensors Journal* 2016, 16.**

[28] **a) B. d. Rosal Rabes, *Doctor* UNIVERSIDAD AUTÓNOMA DE MADRID, UNIVERSIDAD AUTÓNOMA DE MADRID, 2017-01-20, 2017; b) A. B. Adam.**

[29] **a) E. M. Graham, K. Iwai, S. Uchiyama, A. Prasanna de Silva, S. W. Magennis, A. C. Jones, *Lab on a Chip* 2010, 10, 1267; b) K. Okabe, N. Inada, C. Gota, Y. Harada, T. Funatsu, S. Uchiyama, *Nat Commun* 2012, 3, 705; c) P. Haro-González, L. Martínez-Maestro, I. Martín, J. García-Solé, D. Jaque, *small* 2012, 8, 2652; d) R. K. P. Benninger,**

Y. Koç, O. Hofmann, J. Requejo-Isidro, M. A. A. Neil, P. M. W. French, A. J. deMello, *Analytical Chemistry* 2006, 78, 2272; e) J. Yu, L. Sun, H. Peng, M. I. J. Stich, *Journal of Materials Chemistry* 2010, 20, 6975; f) L. Shang, F. Stockmar, N. Azadfar, G. U. Nienhaus, *Angewandte Chemie International Edition* 2013, 52, 11154; g) S. W. Allison, G. T. Gillies, A. J. Rondinone, M. R. Cates, *Nanotechnology* 2003, 14, 859; h) O. A. Savchuk, P. Haro-Gonzalez, J. J. Carvajal, D. Jaque, J. Massons, M. Aguilo, F. Diaz, *Nanoscale* 2014, 6, 9727.

[30] **B. R. Fisher, H.-J. Eisler, N. E. Stott, M. G. Bawendi, *The Journal of Physical Chemistry B* 2004, 108, 143.**

[31] **a) W. Z. Lee, G. W. Shu, J. S. Wang, J. L. Shen, C. A. Lin, W. H. Chang, R. C. Ruaan, W. C. Chou, C. H. Lu, Y. C. Lee, *Nanotechnology* 2005, 16, 1517; b) A. C. Berends, F. T. Rabouw, F. C. M. Spoor, E. Bladt, F. C. Grozema, A. J. Houtepen, L. D. A. Siebbeles, C. de Mello Donegá, *The Journal of Physical Chemistry Letters* 2016, 7, 3503.**

[32] **a) W. J. Mir, A. Swarnkar, R. Sharma, A. Katti, K. V. Adarsh, A. Nag, *The Journal of Physical Chemistry Letters* 2015, 6, 3915; b) P. Jiang, Z.-Q. Tian, C.-N. Zhu, Z.-L. Zhang, D.-W. Pang, *Chemistry of Materials* 2012, 24, 3.**

[33] **H. Wang, C. De Mello Donegá, A. Meijerink, M. Glasbeek, *Journal of Physical Chemistry B* 2006, 110, 733.**

[34] **C. de Mello Donegá, M. Bode, A. Meijerink, *Physical Review B* 2006, 74, 085320.**

[35] **S. Lin, Y. Feng, X. Wen, P. Zhang, S. Woo, S. Shrestha, G. Conibeer, S. Huang, *The Journal of Physical Chemistry C* 2015, 119, 867.**

[36] **V. M. Huxter, T. Mirkovic, P. S. Nair, G. D. Scholes, *Advanced Materials* 2008, 20, 2439.**

[37] **R. Gui, A. Wan, X. Liu, W. Yuan, H. Jin, *Nanoscale* 2014, 6, 5467.**

[38] **M. C. Brelle, J. Z. Zhang, L. Nguyen, R. K. Mehra, *The Journal of Physical Chemistry A* 1999, 103, 10194.**

[39] **L. M. Maestro, C. Jacinto, U. Rocha, M. C. Iglesias-de la Cruz, F. Sanz-Rodriguez, A. Juarranz, J. G. Solé, D. Jaque, *Journal of Applied Physics* 2012, 111, 023513.**

[40] **a) D. Jaque, F. Vetrone, *Nanoscale* 2012, 4, 4301; b) C. D. S. Brites, P. P. Lima, N. J. O. Silva, A. Millan, V. S. Amaral, F. Palacio, L. D. Carlos, *Nanoscale* 2012, 4, 4799.**

[41] **a) J. S. Donner, S. A. Thompson, C. Alonso-Ortega, J. Morales, L. G. Rico, S. I. C. O. Santos, R. Quidant, *ACS Nano* 2013, 7, 8666; b) D. Jaque, B. del Rosal, E. Martin Rodriguez, L. Martinez Maestro, P. Haro-Gonzalez, J. Garcia Sole, *Nanomedicine* 2014, 9, 1047.**

[42] **X. Zhu, W. Feng, J. Chang, Y.-W. Tan, J. Li, M. Chen, Y. Sun, F. Li, *Nature Communications* 2016, 7, 10437.**

[43] **B. del Rosal, E. Carrasco, F. Ren, A. Benayas, F. Vetrone, F. Sanz-Rodríguez, D. Ma, Á. Juarranz, D. Jaque, *Advanced Functional Materials* 2016, 26, 6060.**

[44] **a) T. Munro, L. Liu, C. Glorieux, H. Ban, *Journal of Applied Physics* 2016, 119, 214903; b) L. Liu, K. Zhong, T. Munro, S. Alvarado, R. Côte, S. Creten, E. Fron, H. Ban, M. Van der Auweraer, N. B. Roozen, O. Matsuda, C. Glorieux, *Journal of Applied Physics* 2015, 118, 184906.**

[45] **H. H. Pennes, *Journal of applied physiology* 1998, 85, 5.**

[46] **a) H. P. Sien, R. K. Jain, *Journal of Thermal Biology* 1979, 4, 157; b) G. P. M., *Annals of the New York Academy of Sciences* 1980, 335, 1.**

[47] **a) M. W. Chastagner, R. E. Dodde, A. J. Shih, W. Li, R. K. Chen, *Journal of Heat Transfer* 2016, 138, 074503; b) H. F. Bowman, *Natl Cancer Inst Monogr* 1982, 61, 437; c) C. J. C., *Annals of the New York Academy of Sciences* 1980, 335, 67.**

[48] **a) J. C. Forster, W. M. Harriss-Phillips, M. J. J. Douglass, E. Bezak, *Hypoxia* 2017, 5, 21; b) C. W. Song, A. Lokshina, J. G. Rhee, M. Patten, S. H. Levitt, *IEEE Transactions on Biomedical Engineering* 1984, BME-31, 9; c) P. Falk, *European Journal of Cancer (1965)* 1978, 14, 237; d) M. E. Fallowfield, *European Journal of Cancer and Clinical Oncology* 1989, 25, 1683.**

[49] **D. Ruiz, B. del Rosal, M. Acebrón, C. Palencia, C. Sun, J. Cabanillas-González, M. López-Haro, A. B. Hungría, D. Jaque, B. H. Juarez, *Advanced Functional Materials* 2017, 27, 1604629.**

[50] **a) M. P. Çetingül, C. Herman, *Physics in Medicine & Biology* 2010, 55, 5933; b) K. R. Holmes, *Diagnostic Pathology* 2009, 16, 14; c) A. Bhargava, A. Chanmugam, C. Herman, *Diagnostic Pathology* 2014, 9, 36.**

[51] **Hasgall P.A., Di Gennaro F., Baumgartner C., Neufeld E., Gosselin MC, Payne D., Klingenböck A., K. N., DOI: 10.13099/VIP21000-03-0. , IT'IS Foundation, www.itis.ethz.ch/database 2015.**

[52] **a) B. Choi, N. M. Kang, J. S. Nelson, *Microvascular Research* 2004, 68, 143; b) H. Fujii, T. Asakura, T. Ohura, *Optics Letters* 1985, 10, 104.**

[53] **D. Hanahan, R. A. Weinberg, *Cell* 2011, 144, 646.**

[54] **a) R. H. Thomlinson, L. H. Gray, *British Journal of Cancer* 1955, 9, 539; b) J. A. Straw, M. M. Hart, P. Klubes, D. S. Zaharko, R. L. Dedrick, *JNCI: Journal of the National Cancer Institute* 1974, 52, 1327.**

[55] **E. Neufeld, N. Chavannes, T. Samaras, N. Kuster, *Physics in Medicine & Biology* 2007, 52, 4371.**

[56] **J. J. Mock, M. Barbic, D. R. Smith, D. A. Schultz, S. Schultz, *Journal of Chemical Physics* 2002, 116, 6755.**

[57] **D. Werner, A. Furube, T. Okamoto, S. Hashimoto, *The Journal of Physical Chemistry C* 2011, 115, 8503.**

[58] **B. Bhushan, T. Kundu, B. P. Singh, *Optics Communications* 2012, 285, 5420.**

[59] **P. M. Scop, *Physical Review* 1965, 139, A934.**

[60] **a) D. J. Naczynski, M. C. Tan, M. Zevon, B. Wall, J. Kohl, A. Kulesa, S. Chen, C. M. Roth, R. E. Riman, P. V. Moghe, *Nature communications* 2013, 4, 2199; b) K. Welsher, S. P. Sherlock, H. Dai, *Proceedings of the National Academy of Sciences of the United States of America* 2011, 108, 8943.**

[61] **R. Bhavane, Z. Starosolski, I. Stupin, K. B. Ghaghada, A. Annapragada, *Scientific Reports* 2018, 8, 14455.**

[62] **B. del Rosal, I. Villa, D. Jaque, F. Sanz-Rodríguez, *Journal of Biophotonics* 2016, 9, 1059.**

[63] **S. Nie, *Nanomedicine* 2010, 5, 523.**